THE NATURE OF SINGLE-WALL CARBON NANOTUBE-SILICON HETEROJUNCTION SOLAR CELLS

A Dissertation
Submitted to the Graduate Faculty
of the
North Dakota State University
of Agricultural and Applied Science

By

John Michael Harris

In Partial Fulfillment of the Requirements
for the Degree of
DOCTOR OF PHILOSOPHY

Major Department:
Physics

April 2015

Fargo, North Dakota

North Dakota State University
Graduate School

Title

The Nature of Single-Wall Carbon Nanotube-Silicon Heterojunction Solar Cells

By

John Michael Harris

The Supervisory Committee certifies that this ***disquisition*** complies with North Dakota State University's regulations and meets the accepted standards for the degree of

DOCTOR OF PHILOSOPHY

SUPERVISORY COMMITTEE:

Erik K Hobbie
Chair

Sylvio May

Andrew B Croll

Svetlana Kilina

Approved:

04/15/2015
Date

Erik K Hobbie
Department Chair

ABSTRACT

Since their inception in 2007, nanotube-silicon heterojunction solar cells have experienced rapid improvement due to the diligent work of several research groups. These devices have quickly reached a point where they might begin to possibly compete with current well-established silicon solar technologies; however the development of industrial-scale nanotube synthesis and purification capabilities remains problematic.

Although there has been significant recent progress in improving performance, the precise classification of nanotube-silicon heterojunctions has remained ambiguous. In this thesis, I use type, chirality and length purified single-wall carbon nanotubes to clarify the nature of this particular class of solar cell. The junctions that I assembled were made from freestanding nanotube sheets that showed remarkable stability in response to repeated crumpling and folding during fluid processing, which suggests that the films could be well suited to flexible device platforms. Despite modest ideality factors, the best diodes created in this study met or exceeded state-of-the-art device characteristics, but with a surprising lack of any significant dependence on sample type. The data further suggest that these devices might be simultaneously categorized as either Schottky or p-n junctions. More importantly, the results of this study demonstrate the manner in which band-gap engineering can optimize these devices while emphasizing the important role of the junction morphology.

ACKNOWLEDGEMENTS

There are many people that I need to acknowledge in this dissertation, but let's begin with my advisor, and chair of the Materials and Nanotechnology (MNT) program, Dr. Erik Hobbie. I first met Erik in my senior year as an undergraduate physics student with no research experience and no idea what to do after graduation. Erik took a chance with me as an undergraduate research assistant and I am eternally grateful to him for giving me that opportunity. Upon receiving my bachelor's degree, I became a full time graduate research assistant in Erik's group, where he continued to help me grow as a student and scientist. Thank you very much for your support Erik. Your energy and enthusiasm were very helpful in keeping me going during those moments when it felt like the research was going to get the best of me.

I also want to thank the other members of the MNT research group: Matt Semler, Joe Miller, Bekele Gurmesa, Damith Rozairo, Ahmed Elbaradei, and Sam Brown. You're an awesome group of friends and I'll never forget the laughs and crazy conversations we've shared together over the years. Matt, you're a true laser-ninja and I'm thankful for all the assistance and advice you've given me as I tried to hash out problems in my research. The work you've done to laser cut wafers, streamline the lithography process, and measure the Raman shift across various nanotube samples has proven invaluable. Thank you to Joe and Ahmed for your assistance in measuring nanotube film transparency and helping me learn to use the spectrophotometer. Thank you Bekele for motivating me to keep my head up while writing this thesis and helping me to remember the importance of alternating lab time and gym time to keep the balance. Someday I'll get you on that climbing wall. Last but not least, I thank Damith for his efforts to get the group together for activities outside the lab. These gatherings were always a good time and I can

honestly say that you sir are an excellent cook, I fully plan to use the Sri Lankan cooking techniques you taught me to “wow” some people.

There are a few people in the Center for Nanoscale Science and Technology (CNSE) research group that need to be acknowledged as well. Greg Strommen, Kevin Mattson, and Fred Haring; I thank all of you for your assistance in the clean room. You trained me to use so many pieces of equipment that I've lost count. You've been critical to the success of my research. Kevin, over the years I have called on you to assist me with oxide depositions, wafer dicing, and countless hours of two-person integrity while I conducted hazardous lab processes. I can't thank you enough for your help and I'll always remember the excellent conversations we've shared over the years; you're awesome. Outside the cleanroom, I'd like to thank other members of the CNSE research group: Justin Hoey, Kenny Anderson, and Matt Frohlik. Your help in training me on various pieces of equipment, conducting XPS measurements, preparing acid solutions, proofreading standard operating procedures, and being patient and supportive while I occupied your lab space have meant a lot to me. I would not have been able to complete this research without your help as well.

Finally, I need to acknowledge Jeff Fagan at the National Institute of Standards and Technology. I never got to meet you in person, though I’d like to thank you for your work to enrich nanotube solutions. Your research was critical to my success as a graduate student as you always kept me well stocked with excellent nanotubes.

DEDICATION

To my dad.

Michael J Harris

(1954-2013)

TABLE OF CONTENTS

LIST OF TABLES

LIST OF FIGURES

LIST OF ABBREVIATIONS

AFM.....Atomic Force Microscope

AM .....Air Mass

ASTM .....American Society for Testing Materials

ATPE.....Aqueous Two Phase Extraction

Au.....Gold

$AuCl_3$.....Gold Chloride

BOE.....Buffered Oxide Etch

CDA .....Compressed Dry Air

CH_3NO_2.....Nitro Methane

Cl.....Chloride

CoMoCat.....Cobalt Molybdenum Catalyst

Cr.....Chromium

DGU .....Density Gradient Ultracentrifugation

DOC .....Deoxycholate

DWCNT.....Double-Wall Carbon Nanotube

eDOS.....Electronic Density of States

EELS .....Electron Energy Loss Spectrum

EQE.....External Quantum Efficiency

FF .....Fill Factor

HF .....Hydrofluoric Acid

HMDS .....Hexamethyldisilazane

HNO_3.....Nitric Acid

IEC .....International Eletrotechnical Commission

ITO .....Indium Tin Oxide

J_{sc}.....Short Circuit Current

MCE .....Mixed Cellulose Ester

MEG.....Multiple Exciton Generation

MIS .....Metal-Insulator-Semiconductor

MWCNT .....Multi-Wall Carbon Nanotube

NIST.....National Institure of Standards and Technology

NMP N-Methyl-2-Pyrrolidone

NREL .....National Renewable Energy Laboratory

NSH.....Nanotube-Silicon Heterojunction

OPV.....Organic Photo Voltaic

PCE .....Power Conversion Efficiency

PDMS.....Polydimethylsiloxane

PEC .....Photo Electrochemical Cell

PECVD .....Plasma Enhanced Chemical Vapor Deposition

PERL.....Passive Emitter Rear Locally diffused solar cell

PESC .....Passive Emitter Solar Cell

PMGI.....Polymethylglutarimide

RBM.....Radial Breathing Mode

R_s.....Sheet Resistance

SALS.....Small Angle Light Scattering

SDS .....Sodium Dodecylsulfate

SEM .....Scanning Electron Microscope

Si .....Silicon

SMART.....Simple Model of the Atmospheric Radiative Transfer of Sunshine

$SOCl_2$ .....Thionyl Chloride

SWCNT.....Single-Wall Carbon Nanotube

TEM .....Transmission Electron Microscope

UNSW.....University of New South Whales

vdW.....Van der Waals

vHs .....van Hove Singularity

V_{oc} .....Open circuit Voltage

LIST OF APPENDIX TABLES

LIST OF APPENDIX FIGURES

CHAPTER 1. INTRODUCTION

Since the dawn of the industrial age, world energy consumption has been exponentially increasing, surpassing an annual 15 TW consumption in 2010 according to the American Census bureau. It is estimated that approximately 80 % of this demand is currently met with fossil fuels. According to the International Energy agency this demand is estimated to increase to 25 TW by 2035 with the vast majority of demand coming from strong economic growth in the developing world. In 2006, the European Energy Council set forth a goal to swing energy production such that 80 % of the energy demand in 2040 will be supplied by renewable sources. To reach this goal, solar energy will be critical due to its unlimited planet-wide availability; however a major setback to the advancement of current silicon-based solar technologies continues to be cost associated with the high-temperature crystallization process of silicon (Si), which has a melting point of 1400 °C.

Single-wall carbon nanotubes (SWCNTs) have recently emerged as a viable substitution for Silicon (Si) in a variety of next generation technologies, and it is widely believed that with industrial scale manufacturing, SWCNT-based technologies will become drastically more cost effective. In this contribution I focus on nanotube-silicon heterojunction (NSH) solar cells, which are currently the best performing solar cell architectures implementing SWCNTs. NSH solar cells pair a doped thin SWCNT film in conjunction with a doped-monocrystalline Si layer to create this rapidly improving single-junction architecture.

1.1. A Brief Overview of Monocrystalline Silicon Solar Cells

The first practical solar cell officially came into existence when Russell Ohl, a researcher with Bell Labs, filed a patent in March of 1941 for a light-sensitive silicon device with power

conversion efficiency (PCE) under 1%.[1] The device that Ohl patented was essentially doped crystalline silicon (Si) with a rudimentary PN junction for charge separation. In the 1950s, led by Bell Labs, the field experienced rapid growth due to a new method of creating diffused PN junctions; with PCEs of 4.5% in 1953[2] and 11 % in 1955.[3] The modification of device electrodes into grid patterns demonstrated the power of design by improving the PCE of these diffused junction devices to 14% in 1959.[4]

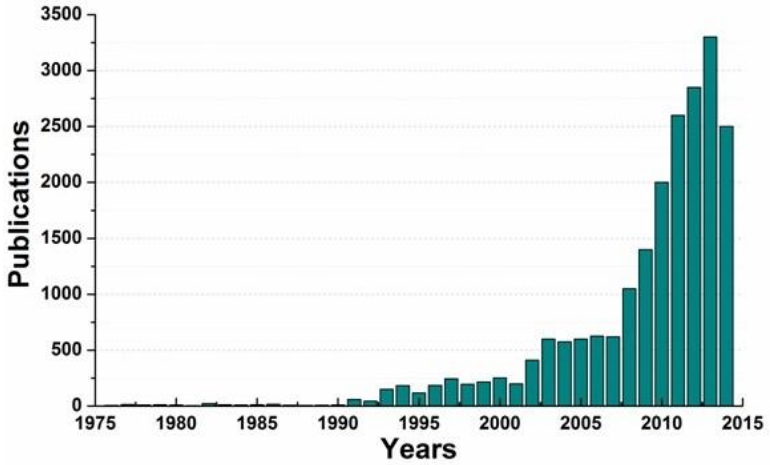

Figure 1: Yearly publications on the subject of solar technology. Compiled through Web of Science v5.16.1.

Over the next few decades this field continued to gain momentum in other ways, with new organizations developing new architectures and the industry as a whole developing measurement standards such as the American Society for Testing Materials (ASTM) E-490 AM0, which is our solar spectrum as measured above the atmosphere. In 1977 NASA began using a new Air mass (AM) 1.5 spectrum, in an attempt to better match the spectral output of the sun at ground level to include absorption and Rayleigh scattering in the atmosphere. This spectrum was later adopted in 1985 by the ASTM (ASTM G173-03 AM1.5), where the global spectrum represents the average light conditions of the continental United States alongside a 37° tilt in the solar panel with respect to the ground (Figure 2). The AM1.5 spectrum became the

industry standard for 1-sun spectral measurements when it was also adopted by the International Electro-technical Commission (IEC) in 1989.[5] This standard was revised as recently as 2008 to create the current AM1.5 IEC 60904 spectrum, used in current photovoltaic research.[6,7]

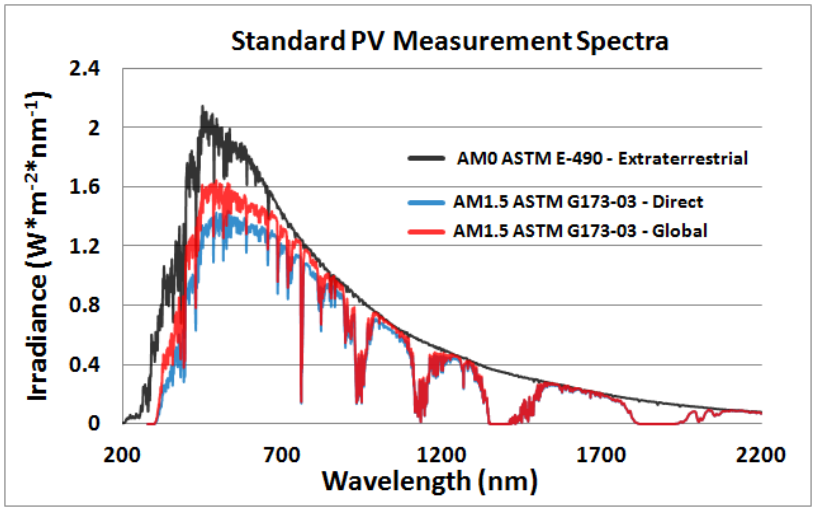

Figure 2: The AM0 and AM1.5 spectra are used for space and terrestrial solar applications, respectively. Spectra were openly downloaded through the Simple Model of the Atmospheric Radiative Transfer of Sunshine (SMARTS) program, which is available on the National Renewable Energy Laboratory (NREL) website. [8,9]

The modern age of solar technology was largely brought about by the University of New South Wales (UNSW) in Sydney, Australia with the development of the single-junction passive emitter solar cell (PESC) in 1983. These devices initially demonstrated PCEs of 19.1 %, later improved to 21% in 1988.[10] A new single-junction architecture called a passive emitter rear locally (PERL) diffused solar cell, also developed by UNSW, was reported the following year. (Figure 3) Initial PERL efficiencies were reported to be 23 % in 1989. These efficiencies were further improved over the course of a decade to 25 % in 1999. This reported efficiency remains the current PCE record for single-junction monocrystalline Si devices.[10]

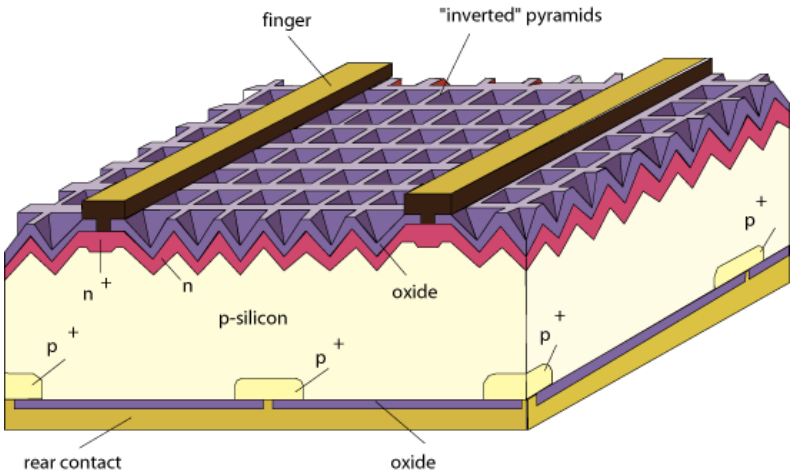

Figure 3: A PERL solar cell designed at the Centre for Photovoltaic Devices and Systems, UNSW. These devices have held the conversion efficiency record for 16 years in the category of single-junction monocrystalline Si solar cells and are well documented in the works of Martin A Green. [10,11]

The theoretical limit in the conversion efficiency for these single-junction silicon solar cells was shown to be approximately 30 % in 1961 in what was called the Shockley-Queisser limit.[12] This theoretical limit is built on the concept of single-exciton generation, which holds that one incoming photon, absorbed at the junction, generates a single exciton. While we have been unable to improve on the efficiency record set in 1999, the Shockley-Queisser limit indicates that further improvements in single-junction Si solar cells are possible but have yet to be realized. In recent years it has been suggested that by replacing the Si on one side of the junction with a material such as SWCNTs, which can exhibit multiple exciton generation (MEG), [13] one can bypass the Shockley-Queisser limit and produce new single-junctions architectures with greatly improved conversion efficiencies.

1.2. The Road From Single-Wall Nanotube Discovery to Nanotube-Silicon Heterojunction Solar Cells

In the last two decades, thousands of research papers have been published focusing on understanding and utilizing single walled carbon nanotubes (SWCNTs) in next-generation technologies. This 'super' material, which is most easily conceptualized as a graphene monolayer rolled into a hollow cylinder, exhibits superior optical, electronic, and mechanical properties.[14-17] These unique, often surprising properties give SWCNTs incredible promise across a broad spectrum of applications, including flexible electronics and cost effective high-efficiency solar cells.

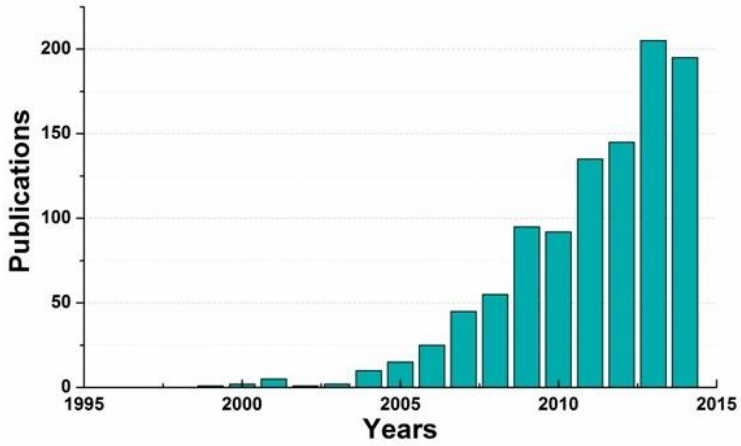

Figure 4: Yearly publications on the subject of carbon nanotubes implemented in next-generation solar technology. Compiled through Web of Science v5.16.1.

The initial discovery of SWCNTs is widely credited to Sumio Iijima for his 1991 characterization in the journal Nature while working at the NEC corporation's Fundamental Research Laboratory in Ibakari, Japan.[18] This publication marks the beginning of the incredibly fast-paced evolution of carbon nanotube research, which in only 24 years has grown and branched out to have real world applications in nearly all technological research fields. In the year following SWCNT discovery, the (*n*, *m*) chiral vector was introduced as a way of

characterizing nanotube structure. The chiral vector characterizes the twist in the graphitic structure of the SWCNT side-wall and specifies the band structure; giving rise to a broad range of metallic and semiconducting SWCNTs.[19] The bandgap for semiconducting SWCNTs was shown to scale inversely with SWCNT diameter (d),[20] which is in the range of 1 nm. In contrast, SWCNT lengths (L) that can reach upwards of 1 cm, resulting in an incredibly high aspect ratio (L/d), which is responsible for many amazing SWCNT properties.[21] Another consequence of SWNCTs 1-dimensional geometry are van Hove singularities (vHs) in the electronic density of states.[19,22] The existence of these singularities has been confirmed though numerous characterizations of the inter-band energy transitions within illuminated SWCNTs, where energy transitions between vHs are directly related to photon absorption. Electron energy loss spectroscopy (EELS)[19,23] can also provide useful information about the SWCNT band structure.

In 2001 it was demonstrated that SWCNTs have the ability to generate a photocurrent under UV illumination.[24] This contribution marks the introduction of SWCNTs into the field of photovoltaics. Early SWCNT-based solar technologies demonstrated fairly low conversion efficiencies and were based on organic photovoltaic (OPV) cells and photoelectrochemical (PEC) cells, which paired SWCNTs with materials such as pyrenes,[25] fullerenes,[26] and doped polythiophene.[27] Further information on these types of solar cells can be found in a handful of enlightening review papers.[28,29]

The NSH solar cell architecture, which is the focus of this contribution, was first presented in 2007.[30] Creation of these devices requires processing SWCNTs into thin-film networks, where conductivity is dependent on nanotube-nanotube sidewall carrier transport and can be interpreted though percolation theory.[31] The fabrication process behind NSH solar cells is described in greater detail in chapter 3 of this paper, though it can be summarized as the

deposition of a thin-film SWCNT network on the surface of a pre-patterned Si wafer where the contact interface between SWCNT and Si serves as the heterojunction for charge separation. It was observed in 2008 that once charge separation has occurred in the NSH solar cell, the primary mode of charge transfer occurs through tunneling at temperatures under 240 °K and thermionic emission for devices over 240 °K (-33 °C).[32]

Band gap engineering became the next phase in NSH solar cells with post-deposition acid treatments of the SWCNT network resulting in noticeable increases in device performance to such a degree that these NSH devices begin to compete with tradition mono-crystalline Si solar cells. Efficiencies near 5 % PCE were demonstrated for chemical functionalization with thionyl chloride ($SOCl_2$).[33,34] Nitric acid (HNO_3) doping brought about another improvement in NSH solar cells by pushing efficiencies to 13 % in a wet-state,[35] but dropping to 10 % in a dry state.[36] In recent years it has been shown that functionalization with gold chloride ($AuCl_3$) can yield the greatest improvements to device performance, with reported efficiencies near 11.2 % in 2013.[37,38] Chemical functionalization is discussed in more detail further below in this dissertation. A few enlightening review papers have been written in the last decade on the rapid advancement of NSH solar technology.[39-41]

In this contribution, I present my work on NSH solar cells fabricated with highly purified SWCNT films that are unmatched in quality by all prior publications on the subject. Specifically, I report on the use of SWCNT films which have been electronically type-sorted to be purely metallic or semiconducting, on chirality-sorted films containing predominantly (6,5) semiconducting or (7,4) metallic SWCNTs, and on electronically mixed films length-sorted to contain only SWCNTs longer than 400 nm.[41] I report efficiencies upwards of 15 % with $AuCl_3$ doping and attempt to shed light on charge separation mechanics in NSH devices through an

examination of the comparatively clean band structure of these devices as compared to those of previously reported devices. This discussion can be found in chapter 5 of this dissertation.

CHAPTER 2. MATERIALS PHYSICS

A benefit of NSH solar cell architecture is the relative simplicity, which makes these devices appealing for large-scale application. The ultimate goal of these devices from a materials science viewpoint is to effectively collect charges generated on either side of a heterojunction. It is important to physically understand the materials comprising both sides of the heterojunction, as well as the mechanism of charge separation within the junction. The NSH architecture described here implements *n*-doped crystalline silicon, a well-established material benefiting from several decades of active research, on one side of the junction. The other side of the junction is a chemically *p*-doped SWCNT film. These doped films are becoming increasingly well understood in the literature, however a clear description of their precise role in NSH solar cells, as well as the resulting charge separation mechanism, are topics of ongoing investigation.

2.1. Single-Wall Carbon Nanotube Physics

A carbon nanotube is most easily conceptualized by rolling a sp^2 hybridized graphene monolayer into a hollow cylinder. The chiral (*n*,*m*) vector, $\vec{C} = n\overrightarrow{a_1} + m\overrightarrow{a_2}$, where *n* and *m* are integers, characterizes the symmetry of this rolling, and dictates whether the nanotube is metallic or semiconducting. This is achieved through the relationship that if $n - m = 3p$, where p is an integer, then the corresponding nanotube is metallic, else semiconducting.[19] (Figure 5) The translational vector is defined as $\vec{T} = t_1\overrightarrow{a_1} + t_2\overrightarrow{a_2}$, where t_1 and t_2 are integers. This vector is both parallel to the central axis of the SWCNT and orthogonal to the chiral vector, which is confined to the hexagonal lattice comprising the nanotube sidewall. The rectangular area that these two orthogonal vectors map out on the side-wall represents a single unit cell in real-space, which contains 2*N* carbon atoms, where N is the number of hexagons contained in the unit cell.[43] The

diameter of a nanotube increases with chirality, where typically observed diameters range from 0.6 to 2 nm. Diameters greater than 30 nm are also possible; these fat nanotubes are referred to as nanofibers. Nanotube length can be anywhere from 10 nm to 1 cm, and in conjunction with the typical 1 nm diameter, results in the exceptionally large aspect ratios (length/width) which are responsible for many of the superior properties that nanotubes possess.[21] A single hollow cylinder of sp^2 hybridized graphene is called a single-wall carbon nanotube (SWCNT). Two concentric cylinders, with a typical cylinder spacing of 0.3 nm, are together called a double-wall carbon nanotube (DWCNT). Similarly, concentric cylinders numbering more than 2 are referred to as multi-wall carbon nanotubes (MWCNTs). The nanotubes used in this research are strictly of the single-walled variety.

Synthesis techniques tend to produce a broad spectrum of SWCNT length and chirality with batches typically containing 1/3 metallic and 2/3 semiconducting. In this contribution, arc-discharge, laser-ablation, and cobalt molybdenum catalyst (CoMoCat) synthesis techniques were used.[44-46]

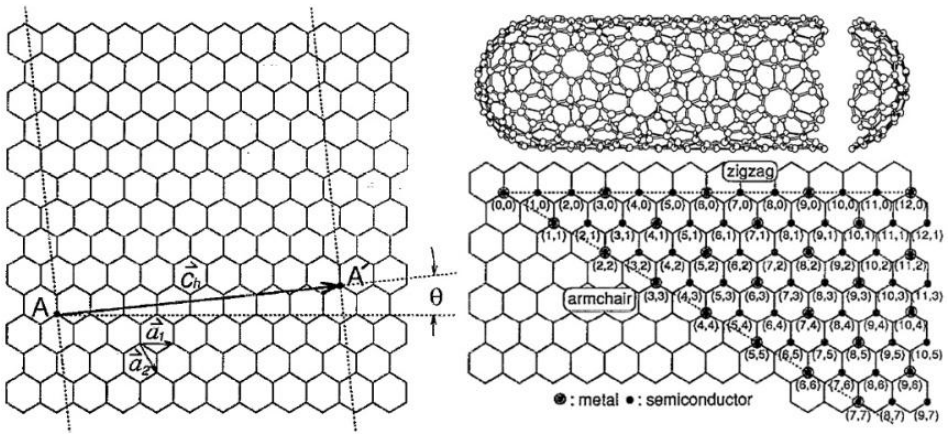

Figure 5: A chiral map indicating the various SWCNT geometries with metallic (big) and semiconducting (small) SWCNT chiralities. Zigzag and armchair nanotubes represent the symmetric boundary conditions for this map. The image is credited to the 1992 work of R. Saito *et al.*[19]

Large aspect ratios allow for a simplified view of SWCNT geometry in which the end-caps on either end of the nanotube can be ignored, which in conjunction with radial symmetry, allows a SWCNT to be modelled as one-dimensional. The van Hove singularities (vHs) within the electronic density of states (eDOS) for both metallic and semiconducting nanotubes are a consequence of this one-dimensionality. Observation of vHs was achieved through a variety of experiments using optical absorption spectroscopy and electron energy loss spectroscopy (EELS).[19,23] In these works, electron transitions from vHs under the Fermi level to those above were shown to correspond to peaks in the optical absorption spectra (Figure 6). Because the chirality of a SWCNT dictates its band structure, a unique nanotube chirality thus implies a characteristic diameter and corresponding band gap, as well as a unique set of absorption peaks and vHs pairs.

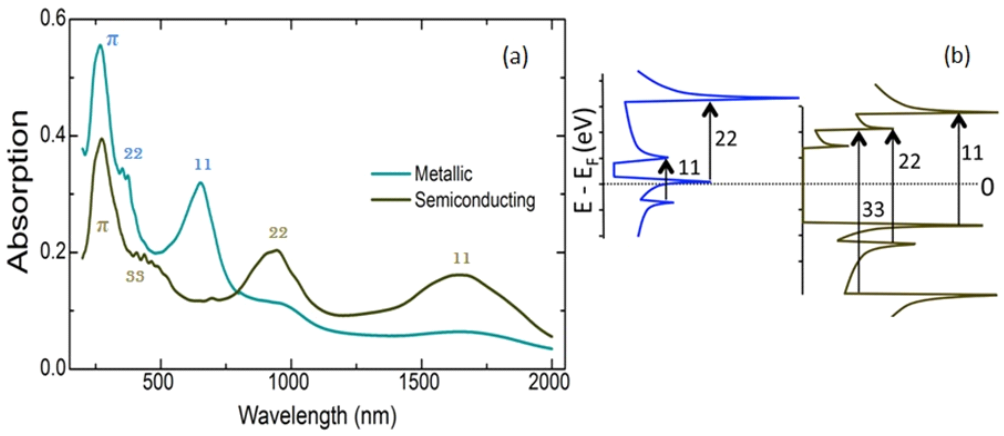

Figure 6: (a) Absorption spectra showing 2 and 3 absorption peaks for metallic and semiconducting SWCNTs respectively. Π-plasmon oscillations are present at 270 nm for both electronic types. Optical resonances M_{ii} and S_{jj} correspond to (b) electron transitions between vHs across the Fermi level (dotted).[50]

Nanotubes assembled into percolated thin films exhibit superior optical, electronic, and mechanical properties as compared with other thin, transparent, conducting films.[47] However, these SWCNT films suffer from a convoluted band structure as a result of the various metallic

and semiconducting chiralities contained within. Great strides have been made in recent years towards nanotube purification via ultracentrifugation and other approaches in an effort to 'clean-up' the band structure.[48,49] Appendix A details the electronic type-separation of the SWCNTs used in this research. As a direct result of these advances, the highly purified SWCNTs used in the presented NHS solar research have a purity that is unmatched in current NHS contributions. These SWCNTs have been electronically type-sorted into almost purely metallic and purely semiconducting solutions; their absorption spectra are represented in Figure 6a. Further chirality enrichment of other various SWCNT materials has allowed for the creation of predominantly (6,5) semiconducting, and (7,4) metallic solutions. The purity of these films is readily demonstrated in the striking color change between various monodisperse SWCNT samples.

Figure 7: Monodisperse SWCNT solutions demonstrate a striking array of colors. Blue solutions are metallic SWCNT enriched, (6,5) enrichment bring out the color purple, and (7,4) enrichment is responsible for yellow.[48,49]

A filtration process described in chapter 3 was used to process these monodisperse solutions into thin-film isotropic networks (Figure 8). Small angle light scattering (SALS) was used to measure the intensity vs. scattering wave vector, *q*. To determine the morphology, this data was fit to a power law to yield the fractal dimension *D*, for metallic and semiconducting

films; $I(q) \propto q^{-D}$ with $D \approx 1.72$ for both (Figure 8c). This indicates that the films can be modeled as quasi-2D mass fractals, where the fractal dimension is independent of electronic type.[50]

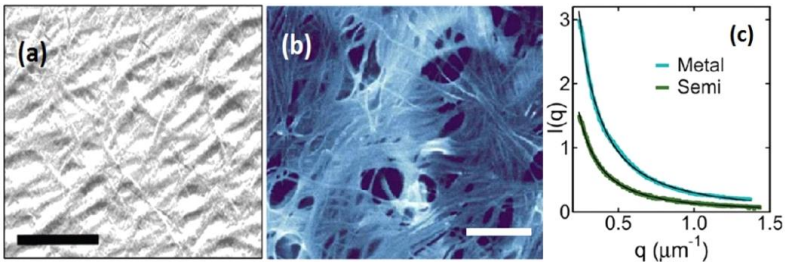

Figure 8: (a, b) TEM images demonstrate the porous structure of these isotropic SWCNT films. (a) 250 nm (b) 200 nm.(c) Scattering intensity is fit to a power law to yield the fractal dimension.

Impedance spectroscopy was used to conduct a capacitive frequency measurement on these metallic and semiconducting films. This test yields the complex sheet resistance as a function of frequency for an alternating current applied to the SWCNT film (Figure 9). The real sheet resistance (solid) shows no dependence on frequency whereas the imaginary (dashed) shows a linear increase, indicating that films comprised of both types are reasonable conductors. A publication from 2012 in ACS Nano details the work I conducted on the electronic durability of these films.[50] This work can be found in Appendix B.

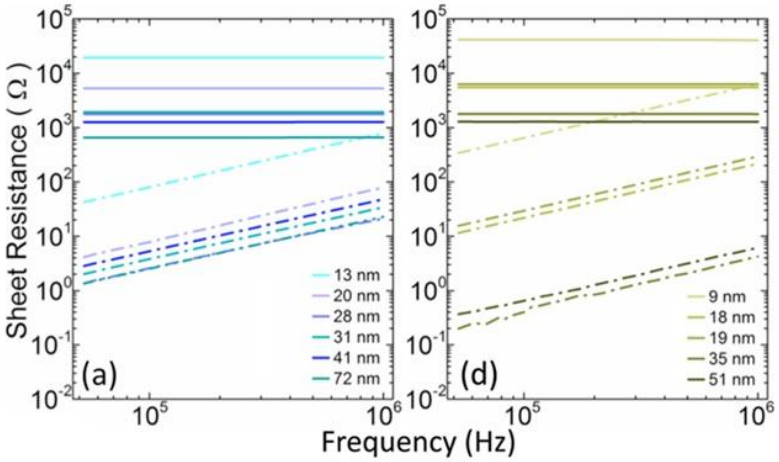

Figure 9: Electronically purified SWCNTS were filtered into purely metallic (blue) and semiconducting (tan) films with various thicknesses. Impedance measurements were used to yield the real (solid) and imaginary (dashed).

The real part of the sheet resistance for these electronically purified films was plotted against film thickness as measured with AFM and fit to a power-law expression for the conductivity of fibrous networks within the percolation theory framework. (Figure 10) In this equation,

$$\sigma(h) = \sigma_o \left(\frac{h}{h_c} - 1\right)^{\alpha}, \quad (1)$$

the critical conductivity is $\sigma_{0,}$ the percolation threshold is $h_{c,}$ and the critical exponent is α. The percolation threshold is a representation of the minimal film thickness at which the films is interconnected, or percolated, at a sufficient level to become conducting. Data fits indicate that our metallic films become percolated at 12 nm and the semiconducting films at 6 nm. Both film types exhibit a critical exponent $\alpha \approx 1$, which places thin-film SWCNTs in accord with other percolated 2D conducting fibrous networks described by percolation theory.[51-53] The critical conductivity for these films was shown to be 3.3 x 10^{-4} □Ω^{-1} and 7.7 x 10^{-5} □Ω^{-1} for metallic and semiconducting films, respectively.

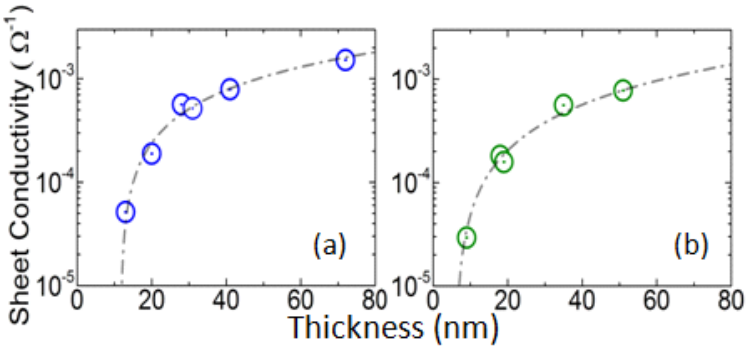

Figure 10: Conductivity is plotted against thickness and fit to a power-law expression from percolation theory to yield the minimum thickness at which 2D clusters films percolate and become conductive.

Raman spectroscopy is a useful tool for studying the normal modes of oscillation for individual SWCNTs within these thin-film networks. This spectroscopy technique relies on the inelastic Raman scattering of photons from a monochromatic laser beam. Nanotubes exhibit

three primary simple modes: the radial breathing mode (RBM), D-band, and G-band. (Figure 11) The RBM represents oscillations in nanotube diameter and provides information on nanotube chirality within the network. A common assumption in the literature is that the frequency of the RBM is inversely proportional to the diameter of the nanotube through the simple relation: $\boldsymbol{\omega_{rbm} = C/d}$, where *d* is the nanotube diameter and *C* is a constant typically in the range of 218 to 248 $cm^{-1}nm$.[54-56] The variation in this constant is due to corrections for environmental conditions such as substrate vs. solution, or isolated nanotubes vs. those that are bundled together.

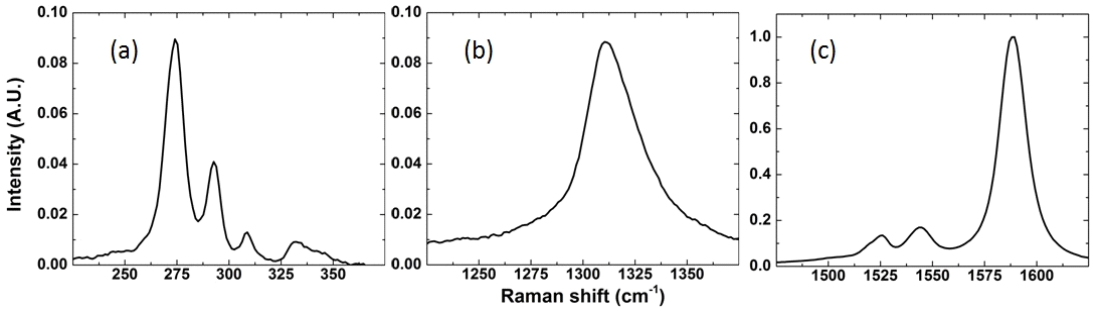

Figure 11: (a) The radial breathing mode, (b) D band, and (c) G band normal modes of oscillation for chirality purified (6,5) SWCNT films, normalized to the G band peak.[42]

An ideal nanotube sidewall is a perfectly hexagonal lattice (Figure 5); though in reality, occasional errors will result in small, localized patches of pentagons and heptagons within the lattice structure. Under photon bombardment, these defects create measurable oscillations in the nanotube sidewall, which correspond to a Raman shift of 1300 cm^{-1} (D band). A third oscillation exists at a Raman shift of 1600 cm^{-1} (G band), which corresponds to shear deformations in the hexagonal lattice structure of the SWCNT. The SWCNTs used in this research exhibit G band intensity an order of magnitude larger than the D band. This is an indication of reasonably high film quality for colloidally processed nanotubes and the purity of the SWCNTs within.

2.2. Chemical Doping of Single-Wall Carbon Nanotube Films

In the presence of air, a SWCNT network will naturally absorb other molecules to become *p*-doped.[57] The ability of these SWCNT films to readily absorb molecules makes chemical doping an important tool for tuning the optical and electronic properties. Density-functional calculations suggest that salt solutions act as effective *p*-dopant for SWCNTs through an anion complex that remains stable in the absence of solvent, with cation-induced ionization providing an intermediate precursor.[58-60] In this work, the chloride (Cl) anion was targeted as the doping molecule through a 3-part chemical process consisting of (1) washing the active area with 1 % HF to remove oxides and clean the junction, (2) chemical doping with 3 drops of thionyl chloride ($SOCl_2$), and (3) chemical doping via spin coating gold chloride ($AuCl_3$) freshly dissolved in nitromethane (CH_3NO_2). The amount of time that lapsed between step 2 and step 3 could be up to weeks without detriment to the final performance of the device.

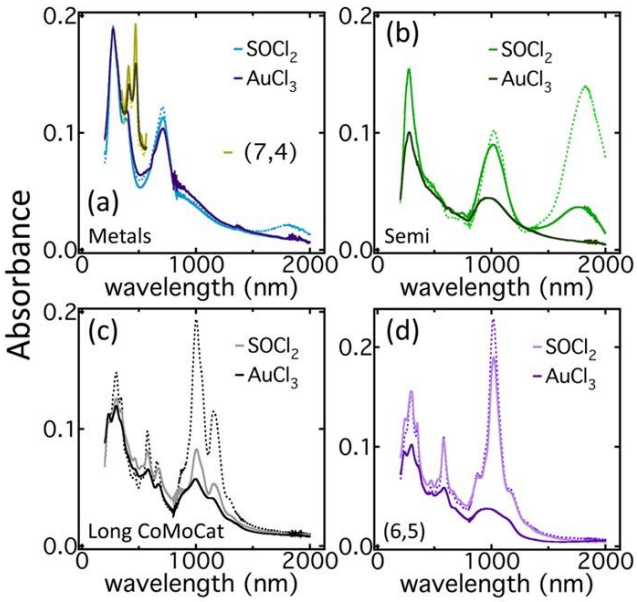

Figure 12: Absorption spectra of different purified SWCNT films; (a) metallic, (b) semiconducting, (c) length-enriched CoMoCat, and (d) (6,5) chirality for intrinsic films (dotted) and after the two consecutive doping steps.

As reported previously by Blackburn *et al.*[47] and Tune *et al.*,[61] doping has different effects on metallic vs. semiconducting SWCNTs. For the latter, we see a large reduction in the oscillator strength f_{11} of the first inter-band transition, whereas for metallic SWCNTs the strength of the interband transition is relatively unaffected. (Figure 12) This decline in the semiconducting f_{11} transition is accompanied by an 80x reduction in sheet resistance (R_s). In comparison, metallic films exhibit an R_s reduction of only 6x without the increased optical transparency of doped semiconducting films. (Figure 13)

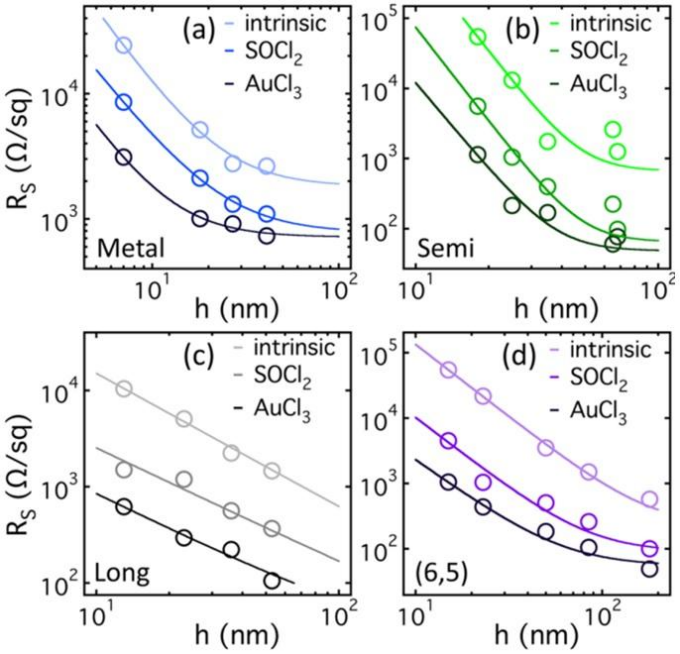

Figure 13: The Sheet resistance measured across consecutive doping steps and plotted against film thickness for 4 monodisperse SWCNT samples.

The physical picture that emerges is one in which doping significantly lowers the Fermi energy, E_F, in semiconducting SWCNTs, often to well within the valence band, while metallic SWCNTs show only a modest shift in E_F accompanied by improved interfacial conductivity.[47] Another important difference suggested by both computation and measurement - particularly for the devices of interest here - is the introduction of mid-gap states for semiconducting

nanotubes.[60,62] Although these states are localized in energy for specific chiralities with well-defined dopant numbers,[60] such features will be smeared in ensembles to yield a density of states (DOS) that qualitatively resembles a metallic SWCNT.

In the case of the monodisperse SWCNT samples used in this research, Raman spectroscopy shows a decrease in the oscillation strength for both the radial breathing mode (RBM) and G-band with relatively no change in the D-band. (Figure 14) This is consistent with chemical absorbates and indicates that the Cl anions are effectively stacking up within the SWCNT thin-film network, where they actively dampen system vibrations.

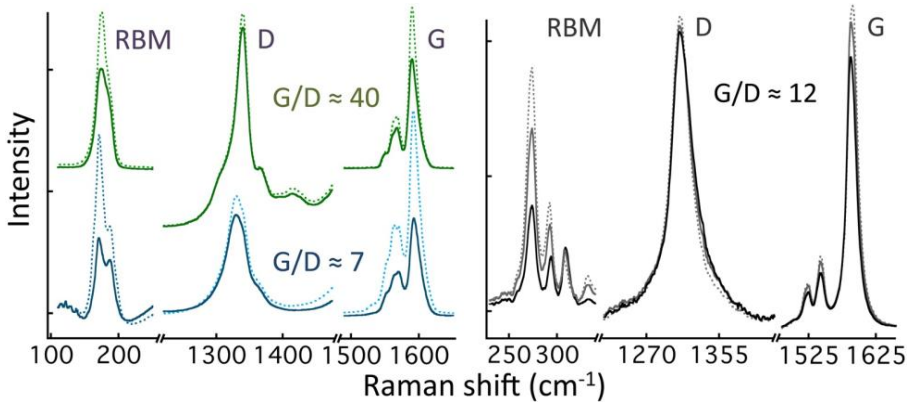

Figure 14: Raman spectra (RBM, D and G mode) of SWCNT samples. Left: semiconducting (green) and metallic (blue) fractions before (dashed) and after (solid) doping. Right: a length-enriched CoMoCat fraction before (dashed), after $SOCl_2$ (light grey) and after $AuCl_3$ (dark grey) doping.

2.3. Heterojunction Morphology

Two different physical interpretations are commonly used to describe the heterojunction within an NSH solar cell; PN junctions and metal-semiconductor (Schottky) junctions. The PN junction is created by bringing a *p*-type and an *n*-type semiconductor of proportional dopant density into direct contact. Charge separation occurs at the connection interface (heterojunction), which quickly equilibrates into a charge-depleted region, containing an electric field generated by the charge to either side. (Figure 15) It is this electric field within the depletion zone that drives exciton separation.

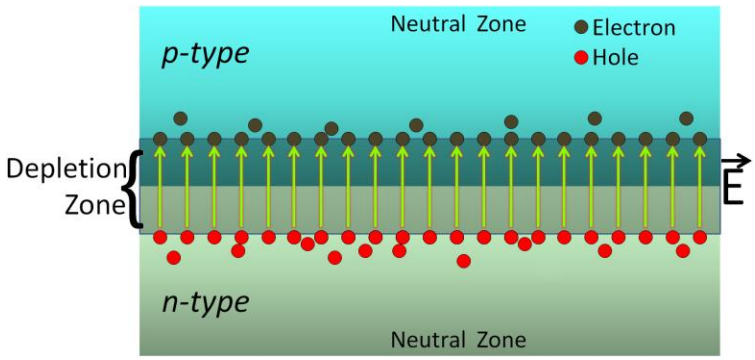

Figure 15: A P-N junction containing an electric field (yellow) as the result of charge separation in the heterojunction. In the standard forward-bias configuration, the *n*-type and *p*-type semiconductors are connected to the cathode and anode respectively.

In the PN model, both semiconducting layers are considered photogenerating, that is to say they both actively absorb photons to create excitons, which randomly move through the semiconductor before decaying into phonon vibrations or encountering the depletion zone and splitting into an electron and hole; each of which is then transported towards their respective electrodes by the electric field. In the works of Jung *et al*.,[37] evidence was presented delineating NSH solar cells as PN junctions; citing considerably low current densities under small reverse bias (10^{-11} A/cm^2), as well as a nearly 0.2 ms response time after abruptly flipping forward to reverse bias.

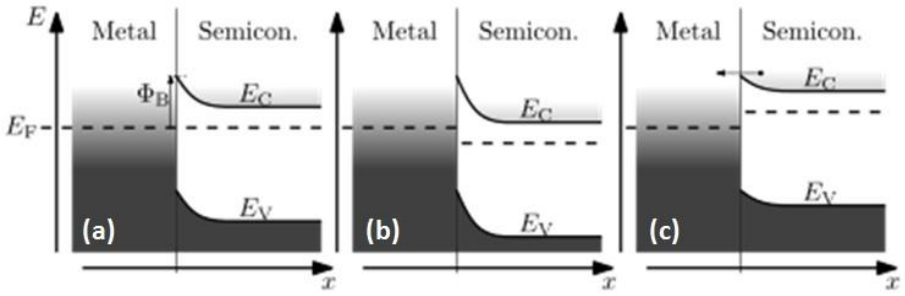

Figure 16: The band diagram for a basic metal-semiconductor Schottky heterojunction. For a device under zero-bias (a) the schottky barrier, ϕ_B, is defines as the difference between the Fermi energy, E_F, and the conduction-band energy, E_c. A schottky junction under (b) reverse bias and (c) forward bias. Image licensed under the Creative Commons (CC) Universal public domain for open use.

The metal-semiconductor Schottky model is the simplest and oldest diode model in physics. Schottky junctions are created by bringing the appropriate type of metal into close contact with the appropriate type of semiconductor; which begins the process of charge transfer as the Fermi level equilibrates between the two materials in intimate contact. The key parameter in these systems is the Schottky barrier. Applying a bias to the Schottky diode alters the alignment of the Fermi levels across the junction. (Figure 16)

CHAPTER 3. NANOTUBE-SILICON HETERJUNCTION SOLAR CELL FABRICATION

This research used *n*-type crystalline Si wafers with a thickness 525 μm; phosphorus-doped, 0.15 Ω cm, 0.2 Ω cm, and 0.4 Ω cm crystalline silicon (n-Si) wafers were submerged in an H_2O_2/H_2SO_4 mixture, buffered oxide etch (BOE), and H_2O_2/HCl (80 °C) in intervals of 10, 1, and 10 min, respectively. This standard RCA cleaning technique yields a pristine silicon surface free of oxides.[63] A 600 nm silicon dioxide (SiO_2) layer was then deposited on top of the wafer via plasma enhanced chemical vapor deposition (PECVD) before placing the wafer in a YES oven (135 °C, 20 min) to both dehydrate and treat the SiO_2 layer with hexamethyldisilazane (HMDS), which improves SiO_2/photoresist adhesion.

3.1. Photolithography and Electrode Deposition

Once the wafer was treated with HMDS, a 1 μm layer of positive photoresist was spin-coated on top and the wafer was placed in a convection oven to soft-bake (90 °C, 1 min). The wafer was then aligned under a clear-field Mylar shadow-mask and exposed to intense UV light for 13 seconds. An additional soft-bake (90 °C, 1 min) was applied to the wafer before submersion in OPD 262 photo developer for 30 seconds to dissolve UV cross-linked photoresist and leave behind a patterned polymer cap on the SiO_2 dielectric. This patterned cap was cured with a hard-bake (120 °C, 1 min) and the wafer was submerged in BOE to etch away any SiO_2 not capped by photoresist. This etching process was considered complete by observing the wafer's surface-response to water. A sudden transition from hydrophilic SiO_2 to hydrophobic crystalline Si was observed as the BOE re-exposed the crystalline surface with an etch-rate of

approximately 100 nm per minute. The wafer was thoroughly rinsed in water to remove BOE, and then acetone to dissolve the photoresist cap.

The BOE wet-etch process used to pattern the wafer's top surface with a SiO_2 dielectric also served to clean the bottom surface of accumulated native oxide. After this etching process was complete, the wafer was placed under vacuum and the bottom surface was coated with 250 nm of aluminum (Al) via Lesker magnetron sputtering. The wafer was then placed in a convection oven and thermally annealed (250 °C, 2 hrs) to create an aluminum silicide interface with a minimal metal-Si Shottky barrier. Direct contact between Al and crystalline Si is required to produce this low-energy barrier, so removing native oxide before depositing Al is critical.

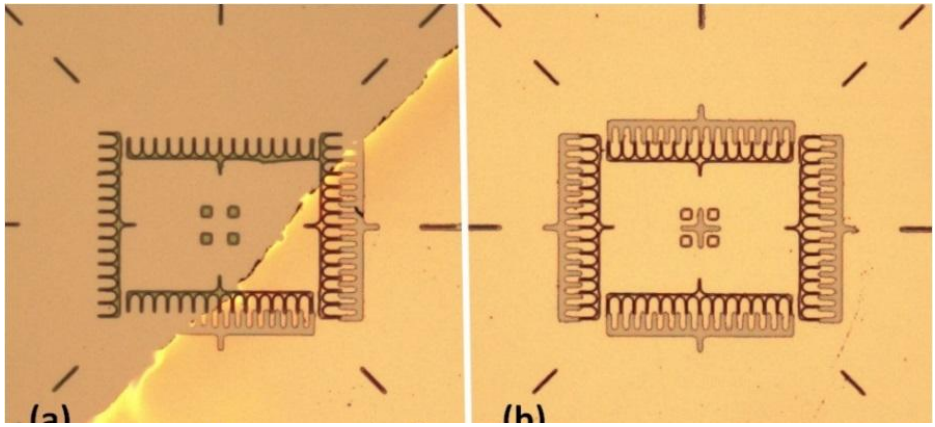

Figure 17: Dual Vernier comb alignment markers were used to accurately position the dark-field Mylar mask (outer-comb) over the patterned SiO_2 dielectric (inner-comb) in preparation for UV exposure. Kapton tape was used to mask (a) prior to Cr/Au/Cr deposition covering (b).

A bi-layer photolithography technique was used to deposit a metal electrode on top of the SiO_2 dielectric with alignment markers that allow for 5 microns of a precision. (Figure 17) This second lithography process began with spin coating the top of the wafer with 200 nm MicroChem™ SF-2S Polymethylglutarimide (PMGI) photoresist. This resist is not susceptible to UV-polymerization and readily dissolves in photo developer and N-Methyl-2-Pyrrolidone (NMP). The thickness of the PMGI layer should ideally be 1.3x the thickness of the metal layer

deposited over top. After spin-coating the wafer with PMGI resist it was subjected to a soft-bake (90 °C, 1 min) to dry the photoresist layer and a hard-bake (180 °C, 5 min) to cure it. This hard-bake is used to fine-tune the etch rate for PMGI in photo developer. Spin-coating recipes and hard-bake etch rates for various PMGI products purchased through MicroChem™ were easily located on the manufacturer's website. A 1 μm layer of positive photoresist was spin coated over the PMGI and the wafer was subjected to a soft-bake (90 °C, 1 min) in preparation for alignment and exposure. Both alignment markers in Figure 1 were used to position a dark-field Mylar mask over the wafer, which was then exposed to intense UV light for 13 seconds followed by a final soft-bake (90 °C, 1 min). The wafer was submerged in photo developer to cut channels in the photoresist bi-layer directly over the SiO_2 dielectric. It was observed to take roughly 30 seconds in developer to dissolve the 200 nm PMGI bottom layer enough to adequately undercut the 1 μm positive resist top layer. The freshly developed bi-layer cap was gently and thoroughly rinsed with DI water and air dried with compressed dry air (CDA). The patterned bi-layer was coated with chromium (Cr) and gold (Au) under maintained high-vacuum magnetron sputtering; deposited Cr, Au, Cr had targeted thicknesses of 10, 100, 10 nm respectively. Finally, the wafer was soaked overnight in N-methyl-2-pyrrolidone (NMP) to dissolve the photoresist and remove excess metal, exposing the SiO_2-insulated Au/Cr electrodes.

3.2. Isotropic Single-Wall Carbon Nanotube Film Preparation

The SWCNTs used in this research were fabricated though the laser ablation and Cobalt Molybdenum catalyst (CoMoCat) methods.[64,65] Initial purification of these SWCNTs was achieved through density-gradient ultracentrifugation (DGU).[66] Further chirality enrichment was achieved through nonlinear DGU.[67,68] Length-enriched CoMoCat fractions were prepared by dispersing the SWCNTs (Southwest nanotechnologies lot SG65EX or SG65i lot 046) in water

via ultrasonication with 2 % sodium deoxycholate (DOC). The suspensions were coarsely centrifuged to remove impurities and bundles and then purified by length using transient DGU.[69,70] Length enriched SWCNT fractions were characterized with AFM to yield fractions with a typical nanotube length > 400 nm.

Most recently, type and chiral enrichment has been achieved using the aqueous-two-phase-extraction (ATPE) approach developed at NIST. This method is well documented elsewhere.[42,71,72] These enrichment methods were used to yield high-quality SWCNT films, purified by electronic type, length, and individual chirality, to create the NSH solar cells in this research. All nanotube purification steps were performed by our collaborators at NIST. To prepare surfactant-free films on filter paper supports, a 250 mL solution of 10 % ethanol in DI water was prepared in a vacuum filtration apparatus over mixed cellulose ester (MCE) filter paper. An aqueous solution of surfactant-laden purified SWCNTs was then slowly injected at the MCE surface. The SWCNT solution separated from the ethanol solution as it spread into a uniform puddle over the MCE. To ensure film uniformity, the SWCNT-rich interlayer was given 20 minutes to fully settle before applying a 10 psi (20 inch Hg) vacuum. Excess surfactant was removed as the nanotubes assembled into a stable isotropic film on the surface of the MCE paper. After filtration, the MCE was thoroughly rinsed in DI water and vacuum dried. The purified SWCNT films created here have thicknesses ranging from 10 to 200 nm.

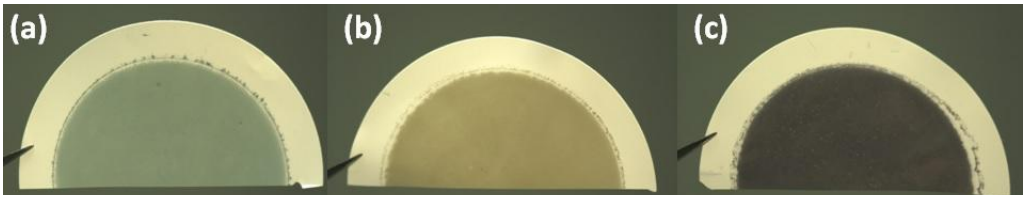

Figure 18: (a) Electronically type-sorted metallic SWCNTs, (b) (7,4) chirality purified metallic SWCNTs, and (c) (6,5) chirality purified semiconducting SWCNT filtered into films on MCE paper demonstrate the purity of the enrichment process.

3.3. Depositing a Single-Wall Carbon Nanotube Film

Different deposition processes were explored and employed with more or less the same results. I describe here the final and simplest process. Rectangular samples were cut from MCE paper and dropped into a 20 mL acetone bath. Dissolution of MCE began immediately and within 15 min the SWCNT films were typically observed to be free floating. (Figure 19) After 1 h, the film was collected in the plastic tip of a 1 mL micropipette along with a small amount of acetone. Proper pressure on the pipette allowed retention of the film along the sidewall of the pipette while acetone was drained away.

This free-standing behavior in SWCNT films was surprising. I expected the film to collapse in on itself and aggregate to the bottom of the solution through self-vdW interactions as the film's surface contacts itself. In water, SWCNT hydrophobicity becomes apparent. The film will behave one of two ways; if close to the surface of water it will move there and tightly hug the air-water interface to minimize water contact. If the film is not near a high surface-tension interface, it will behave as expected; crumble and aggregate to the bottom. A study of the wrinkling mechanics of SWCNT films on strained polymer support can be found in appendix C. This work was published in Soft Matter in 2013.[73] In a brief summary of the work in appendix C; wrinkling compression of SWCNT films was shown to change film morphology by decreasing the Elastic modulus of the film through a process called strain-softening. These free-standing films in ethanol might prove useful to future manufacturing processes, so it is important to know if these films are degrading in solution due to strain softening.

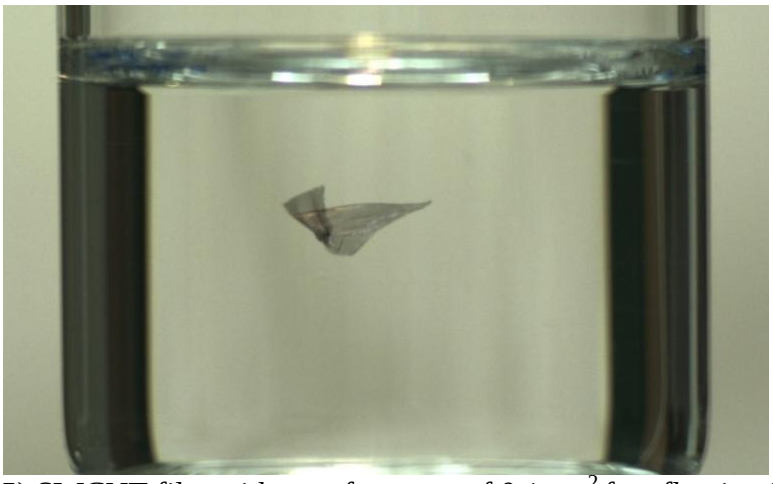

Figure 19: A (6,5) SWCNT film with a surface area of 0.1 cm^2 free floating in ethanol prior retrieval and deposition to fabricate a NSH solar cell.

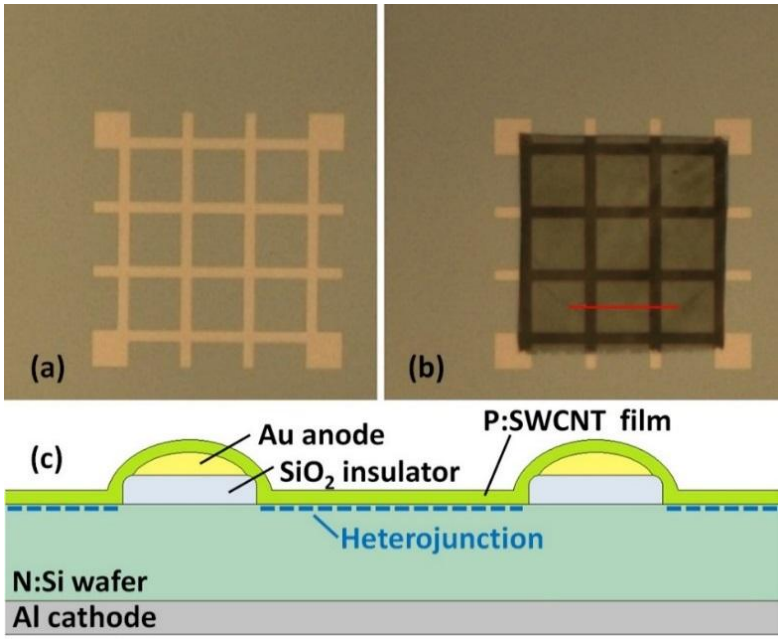

Figure 20: (a) A SiO_2-insulated electrode patterned into a grid with 1mm spacing as described in chapter 3.1. (b) Supporting movies demonstrate the fluid mediated deposition process used to position a SWCNT film over the electrodes. (c) A cross section diagramming the device architecture across 2 electrodes indicated in (b) (not to scale).

Clean acetone was quickly pulled into the pipette to retrieve the film and deposit it into a second vial of acetone for an additional hour. This process was repeated across three 20 mL acetone vials to remove all traces of MCE paper, and subsequently across three 20 mL ethanol vials to

remove residual surfactant from the SWCNT network. After the third ethanol bath, the film was collected in a clean pipette and deposited onto the pre-patterned Si substrate. Droplets of ethanol were used to unfurl the film. This process was easily accomplished in a puddle small enough to be contained by the surface tension provided by the wafer substrate. Once the SWCNTs were unfolded, ethanol was removed to form a thin liquid film on the surface of the substrate. It was observed that this thin ethanol puddle served very nicely as a medium through which air jets from a 1 mL micropipette could be used to orient and position the SWCNT film. After SWCNT/electrode alignment was achieved the remaining ethanol was allowed to evaporate, depositing the SWCNT film on the electrodes, creating a NSH solar cell first discussed in chapter 1.

An experiment was conducted to study NSH solar cell performance across different processing techniques. In this experiment, the ethanol deposition method was compared to the traditional water collection method. The study compares these methods alongside additional processing techniques: thermal annealing and HF exposure to expose the pristine Si surface. This study is found in appendix D, and yielded the conclusion that simple ethanol deposition provides the best device performance. Hydrofluoric acid treatment increased the device fill factor, or ratio of actual power output to ideal output. This can be interpreted as an improvement of the SWCNT-Si connection interface through the absence of naturally accumulated surface oxides upon SWCNT deposition. No other performance measure benefitted from the treatment, which was found to short lived, as oxides accumulate naturally on exposed Si.

CHAPTER 4. CHARACTERIZATION METHODS

Thin highly-enriched SWCNT films were prepared on optical-grade quartz in the manner described in Chapter 3 and subjected to a variety of measurements to understand their optical and electronic properties.[50,73] Additional SWCNT films were prepared over pre-patterned Si wafers to create NSH solar cells, which were subjected to a series of treatments to chemically functionalize the SWCNT film prior to a series of measurements to gauge the photovoltaic performance.[42]

4.1. Single-Wall Carbon Nanotube Film Properties

Characterization of these SWCNT films began with the collection of film thickness, transparency, and conductivity. To start these measurements, tapping-mode atomic force microscopy (AFM) on a Digital Instruments Inc. Dimension 3100 AFM was used to measure the thickness of SWCNT films deposited on quartz by collecting multiple step-heights along the film edge. (Figure 21)

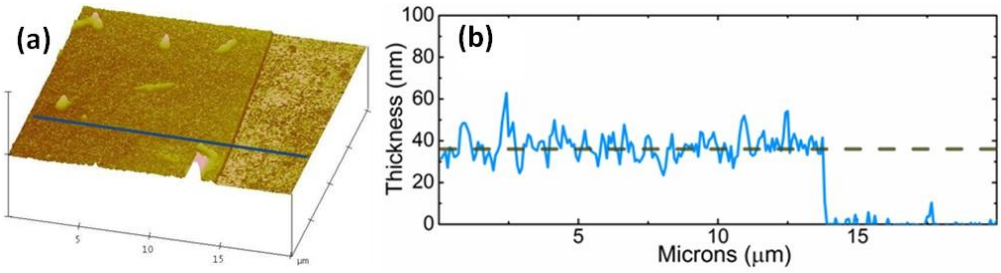

Figure 21: (a) Tapping mode AFM was used to scan SWCNT film edges at multiple points to yield film thickness through several cross-sectioned (b) step height measurements.

Film transparency was characterized on quartz with an Ocean Optics QE 6500 Spectrometer. Light intensity over a wavelength range of 500 to 750 nm was measured through the SWCNT film and divided by the same measure through the substrate to yield transparency.

This transparency measure was independently confirmed though the collection of absorption spectra over a wavelength range of 200 to 2000 nm using a Cary 5000 UV-Vis-NIR spectrophotometer. It was important for the accuracy of the absorption spectra to use films prepared on optical-grade quartz with SWCNT sample sizes larger than the incident illumination beam, which was observed to be 1 mm by 5 mm in reduced-beam mode.

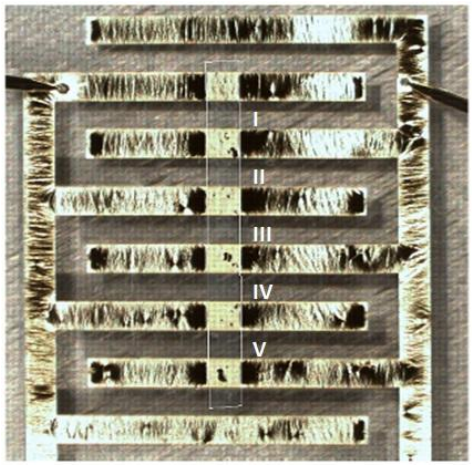

Figure 22: Interdigitated electrodes were deposited over a SWCNT film to create multiple SWCNT regions connected in parallel.

The conductivity of these SWCNT films was measured with capacitive frequency impedance spectroscopy on an Agilent B1500A semiconductor device analyzer. Narrow SWCNT films were prepared on quartz in the manner described in Chapter 3. Interdigitated electrodes consisting of 10 nm Cr under 100 nm Au were deposited over the SWCNT film via Lesker magnetron sputtering without breaking vacuum. The capacitive frequency measurement involved connecting probes to the interdigitated electrodes and applying an alternating current to the device with increasing frequency from 1 kHz to 1 MHz. This measure yielded the complex impedance of the SWCNT film, which was easily converted to complex sheet resistance by multiplication by a geometric prefactor, *G*. This prefactor takes into account SWCNT film width,

W, and the distance between the electrodes, *L*, in a simple summation across all enclosed SWCNT regions like those indicated with roman numerals in Figure 22;

$$G = \sum_{i=1}^{n} \frac{W_i}{L_i} . \quad (1)$$

The real sheet resistance was extracted from the complex sheet resistance, and the reciprocal was taken to yield SWCNT film conductivity. A mathematical scaling argument which relates SWCNT sheet resistance to a parasitic loss in solar-cell power is presented in appendix E.

4.2. Photovoltaic Properties

Freshly prepared NSH devices were placed under vacuum for several hours to remove excess ethanol from the SWCNT film before being placed in an Olympus BX51 optical microscope to measure active area. The average active area was approximately 0.1 cm^2 for the NSH devices used in this research. Chemical processing on each device began with the removal of native oxides from the heterojunction with 1 % Hydrofluoric (HF) acid in DI water for 1 minute. The HF was then thoroughly rinsed from the SWCNT network with DI water and the device was blown dry with nitrogen. Two droplets of thionyl chloride ($SOCl_2$) were then deposited over top to chemically functionalize the SWCNT network and the device was left to dry in air for 2 hours. The NSH solar cell was placed in a Laurel WS-400BZ spin coater under a puddle of gold-chloride ($AuCl_3$) prepared in nitro methane with a concentration of 5 mM. This puddle was left to fully cover the SWCNT film for 30 seconds before being spun off the substrate at 2500 RPM for 20 seconds. Functionalization with $AuCl_3$ was observed to yield the greatest benefit to photovoltaic performance; the mechanisms and results of chemical functionalization are presented in subsequent chapters of this dissertation. Immediately after $AuCl_3$ functionalization, the NSH device was subjected to a variety of measurements.

First, the IV profile was measured at air mass (AM) 1.5, giving an irradiance of 100 mW/cm^2 on an SS50AAA solar simulator (Photo Emission Tech Inc.) in conjunction with a Keithley 2400 source meter and 2000 multimeter. This model of solar simulator implements a vacuum-stage to contact a back side electrode, and 2-point probes to contact the top electrode in different places; this 2-point system is used to account for the work function between the probe and electrode. External quantum efficiency (EQE) was collected in a QE/ICPE QEX7 Measurement System (PV Measurements Inc.) by focusing a source beam on the heterojunction to maximize signal strength in the detector, which was connected with the NSH solar cell in a 2-point-probe configuration. A potential was applied to the device and the source beam was cycled through a wavelength range of 200 to 1200 nm to generate a photocurrent and yield the solar cell's EQE as a function of wavelength. The reverse-transient recovery time was measured by connecting the NSH device in series with a 200 Ω resistor, oscilloscope (Tektronix TDS 3034B), and function generator (BK Precision Instruments 4011A) which subjected the device to a square-wave potential offset at -2 V to 5 V, oscillating at a frequency of 3.55 kHz. This measurement provides a useful tool in determining the presence of minority carriers in the heterojunction where longer recovery times are indicative of the long minority carrier lifetimes exhibited by PN junction architectures.[37] A capacitive-voltage (CV) measurement conducted with an Agilent B1500A Semiconductor Analyzer was used to measure the capacitance from -2V to 0.5 V. The Agilent B1500 is work-horse with a vast amount of programmable impedance spectroscopy tools. The inverse-square of the capacitance, when plotted against potential, shows a linear trend, which was used to extract the built-in potential of the device.[37] In the final measurement, the NSH solar cell was placed on a hot plate in a small metal isolation hood to uniformly heat the sample in the absence of light. Agilent probes were connected to the device in

a 2-point configuration and the IV profile was measured at 20 K increments, from 20 °C to 120 °C, to characterize the thermionic properties. These measurements were then analyzed to yield device ideality, Schottky barrier height, and the Richardson constant of the devices.

An indepth scan was conducted through X-ray photoelectron spectroscopy (XPS), to map the elemental composition of the solar cell from the surface of the SWCNT film down to the heterojunction interface, stopping a short depth into the silicon. The details of this XPS ‘core sample’ can be found in appendix F.

CHAPTER 5. RESULTS AND DISCUSSION

Among SWCNT-silicon solar cells in general, air-stable devices with photo conversion efficiencies (PCEs) of 10-12 % have been reported without chemical doping,[74,76] while the current record efficiency (15 %) relies on an antireflective coating.[77] For *p*-type nanotubes on *n*-type silicon (Si) in the absence of antireflective treatment, the best characterized diode to-date corresponds to a PCE just over 11 %, a fill factor (FF) just over 74 %, and an open-circuit voltage (V_{oc}) of 0.53 V, an accomplishment that can be linked to remarkably small dark currents and diffusion dominated transport.[37] These traits, in turn, stem from a junction ideality factor just below 1.1, where a value of 1 corresponds to ideal behavior with homogeneous contact and suppressed recombination.[37] Comparable ideality has also recently been reported for graphene-Si diodes.[78] Chemically doped SWCNT-Si junctions with "wet" interfaces can achieve better performance,[35] and while devices with chemical doping exhibit stability issues,[40] the question of where the performance ceiling resides continues to have important implications for this technology.

Despite these accomplishments, our fundamental understanding of SWCNT-Si heterojunctions remains incomplete. While there is strong consensus that an atomically thin layer of graphene leads to behavior that closely resembles a Schottky barrier,[78-86] there is disagreement as to whether SWCNT-based devices represent Schottky,[39,40,87-89] metal-insulator-semiconductor (MIS),[37,61,90] or PN junctions.[91,92] The devices engineered by Jung *et al.* using mixed-type SWCNTs, for example, show nearly ideal PN diode behavior,[37] while Tune *et al.* demonstrated the importance of nanotube metallicity in what more closely resemble Schottky junctions.[61] To the best of our knowledge, this latter study is the first and only attempt to clarify the role of nanotube electronic type SWCNT-Si heterojunctions.[67] The diversity of opinion is surprising

given that unsorted SWCNTs typically occur in a ratio of 2/3 semiconducting to 1/3 metallic and thus might naively be expected to behave as a semi-metal.

The fabrication approach described in Chapter 3 of this dissertation is based on a novel fluid-processing scheme applied to freestanding SWCNT films that show remarkable stability in response to large-amplitude deformation, including the ability to repeatedly crumple and fold prior to being unfurled on patterned substrates. Despite modest ideality, we were able to achieve state-of-the-art dry characteristics (PCE ≈ 15 %, FF > 76 %, V_{OC} > 0.6 V, short-circuit current ≈ 35 mA/cm^2) in simple geometries without antireflective coatings. We also found a significant and somewhat surprising dependence on sample type, with our data suggesting that these devices can simultaneously exhibit characteristics of both Schottky and PN junctions. We applied simple scaling arguments to model the behavior over a broad range of sheet resistance and film thickness in a manner that highlights the unique role of doping-induced SWCNT mid-gap states. Our results clarify how band-gap engineering can optimize SWCNT-Si photodiodes while emphasizing the potential importance of precisely controlling the contact morphology of the heterojunction.

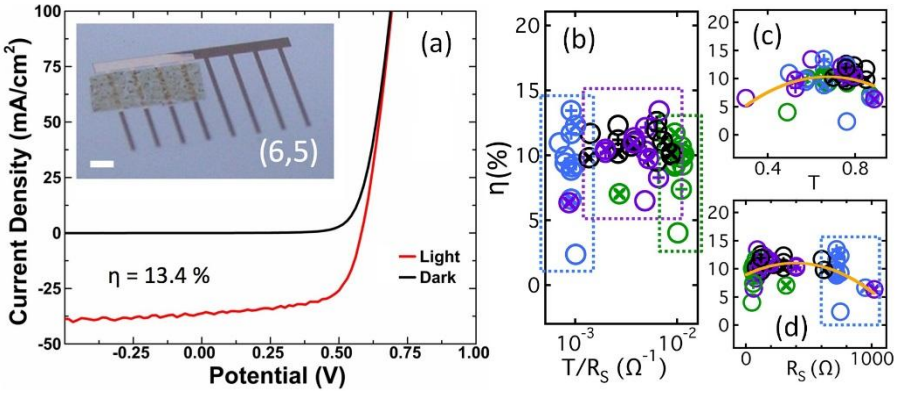

Figure 23: (a) The IV profile for the best performing device on comb-electrodes (inset). (b) PCE vs. transmission divided by sheet resistance, boxes indicate segregated dispersions. (c) PCE as a function of transmission and (e) PCE as a function of sheet resistance. All devices correspond to the comb pattern in part (a) (⊕ denotes 0.15 Ω cm, O denotes 0.20 Ω cm, and ⊗ denotes 0.40 Ω cm Si substrate). The transmission corresponds to 650 nm but the trends are the same for any wavelength near the peak of the solar spectrum. The curves are quadratic fits.

A common figure-of-merit is the ratio of the optical transmittance near the peak of the solar spectrum, $T(\lambda_0)$, to R_s.[93] As shown in Figure 23 for a large number of devices with the 'comb' electrode pattern, (Figure 23a), plotting the PCE (η) as a function of $T(\lambda_0)/R_S$ segregates the devices by type, with the best performers - metallic and (6,5) SWCNTs - separated by nearly a decade. Plotting this data as a function of $T(\lambda_0)$ (Figure 23c) reveals no such segregation, while plotting it as a function of R_S (Figure 24b) demonstrates that the dichotomy arises from the drastically different sheet resistance of the doped semiconducting and metallic films (Figure 13). It is surprising and unexpected that both metallic and (6,5) semiconducting SWCNTs yield such good devices at such disparate values of R_S.

We take this analysis one step further in Figure 24, which shows PCE (averaged over common thickness and varied substrate doping for each type) as a function of film thickness. Only the semiconducting SWCNTs fail to meet or exceed the performance of comparable devices,[37] despite a comb electrode pattern (inset, Figure 23a) simpler than that used by most groups, a shortcoming we corrected through the addition of evenly spaced cross-members to the comb design to create a grid electrode with 1 mm spacing. (inset, Figure 25) The trends in Figure 24a-b are easy to understand: thinner SWCNT films have high transmission but higher R_S and hence lower PCE. This trend is suppressed in the length-enriched sample, which exhibits a lower percolation threshold because of a 2× higher nanotube aspect ratio.[94] Thicker films, in contrast, have lower R_S but lower transmission and hence lower PCE; each film type has an optimum thickness dictated by competition between $T(\lambda)$ and R_S. We account for these trends with a simple scaling argument derived in Appendix E. If the series resistance of the devices arises predominantly from R_S, then

$$\eta \propto J_s \ln\left(\frac{J_s}{J_0}\right)\left(1 - \frac{J_s A R_s}{V_T \ln\frac{J_s}{J_0}}\right) \tag{2}$$

where J_S is the photocurrent, J_0 is the saturation current, A is device area and $V_T = k_B T / q$ is the thermal voltage (k_B is Boltzmann's constant and q is the fundamental charge). Because J_S scales with transmission, $\eta R_s \propto x(1 - ax + \cdots)$ with $x = T(\lambda)R_s$, where the deviation from linearity directly measures the impact of R_S. (Figure 24c) The metallic and thinner samples group at larger $T(\lambda)R_s$ where curvature starts to emerge.

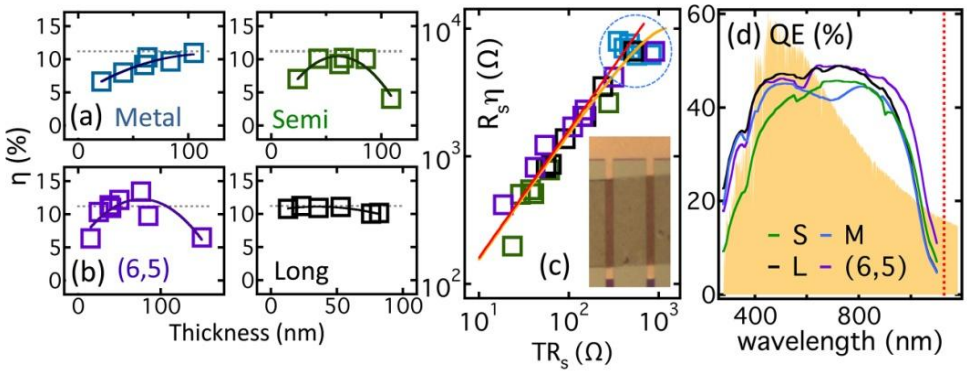

Figure 24: (a) Mean PCE as a function of film thickness for metallic (left) and semiconducting (right) films, and (b) a similar plot for (6,5) (left) and length-enriched (right) films. The curves are quadratic fits and the horizontal dashed line is the PCE for comparable devices reported by Jung *et al*.[37] (c) Scaling plot of the PCE and (d) EQE of each type superposed on the NREL 1.5AM solar spectrum, where the vertical line corresponds to the band gap of Si. All devices use the comb electrode pattern [inset to both (c) and Figure 5.1a].

The poorer performance of the laser-ablation semiconducting SWCNTs was independently verified by measuring the external quantum efficiency (EQE). The EQE is a ratio of the number of charge carrier created, over the total number of photons hitting the material. All devices show a loss of efficiency just below the wavelength corresponding to the band gap of Si, but the semiconducting SWCNTs have lower EQE near the solar spectral maximum (Figure 24d). A detailed superposition of the EQE on the corresponding absorption spectra (Figure 25) confirms that the EQE exhibits a minimum in the vicinity of each absorption peak, implying that

absorption of light within the SWCNT film is a detriment to performance. The EQE drops with SWCNT absorption because those photons aren't making it to the Si. This leads us to a view where the SWCNT films generate negligible photocurrent and simply serve as charge collection layers. In order of decreasing η, the ranking suggested by Figures 24 & 25 is; (6,5), metallic, length-enriched, semiconducting. This reveals the simplest mechanism by which SWCNT band-gap engineering impacts these devices. Normalizing the fully doped absorption spectra on a common scale and superposing them on the solar spectrum, the metallic films have the lowest absorption in the vicinity of λ_0 = 500 nm while the semiconducting films have the highest because of a superposition of *33* inter-band features arising from a broad distribution of diameters. Similarly, the length-enriched CoMoCat SWCNTs have significantly stronger absorption than the (6,5) SWCNTs from 800 nm out to the near infrared. Isolating single nanotube species or chiralities can thus reduce optical absorption by eliminating extraneous absorption resonances, thereby increasing the photocurrent generated in the Si surface.

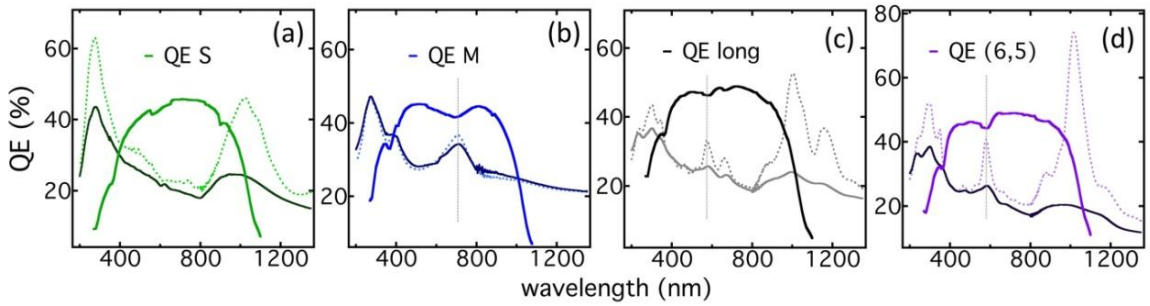

Figure 25: External quantum efficiency with the corresponding fully doped (dark) absorption spectra for (a) semiconducting, (b) metallic, (c) length-enriched CoMoCat and (d) (6,5) SWCNTs. Dashed traces are absorption spectra before doping with a clearer indication of peak position.

Although SWCNT type and chirality can impact device performance through the mechanisms described above, the underlying nature of the junctions needs clarification. To do so we focused on the dark transport characteristics. We also moved to a 'grid' electrode pattern

(inset, Figure 26a) that yields significantly higher PCE due to increased charge collection in orthogonal directions on isotropic films. Figure 26b shows a correlation between PCE and FF over a broad range of film thickness, where the best performers are metallic and (6,5) semiconducting SWCNTs prepared on the inset grid pattern of Figure 26a. Optimal film thicknesses for this pattern are 40-to-50 nm. Figure 26c shows the measured dark current (J_d) of devices in Figure 26b with the two highest performers indicated. A semi-log plot of the same data is shown in Figure. 26c. The bias dependence of J_d is modeled as[88]

$$J_d = J_0\left(e^{\frac{V}{nV_T}} - 1\right), \tag{3}$$

where J_0 is the saturation current and n is the ideality factor. We find nearly equivalent state-of-the-art performance for both metallic and (6,5) films despite modest ideality (n = 1.5).

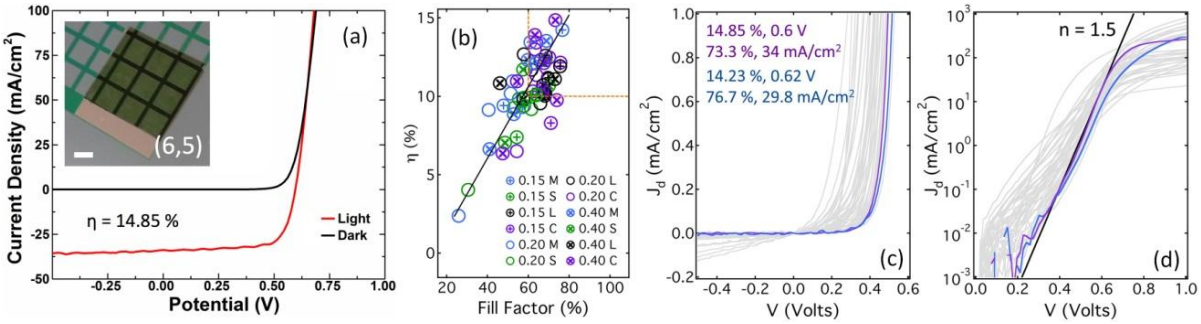

Figure 26: (a) An upgraded grid-electrode showing improved device performance. (b) PCE vs. FF for a large number of devices [M = metallic, S = semiconducting, L = length-enriched, and C = (6,5)-enriched, where ⊕ denotes 0.15 Ω cm, O denotes 0.20 Ω cm, and ⊗ denotes 0.40 Ω cm substrates]. (c) Dark currents for devices in (b), where the best performers - a metallic and a (6,5) film - are highlighted in color. (d) A semi-log plot of the data showing ideality.

Table 1: Best performing NSH devices across SWCNT sample type.

	h_{swcnt} (nm)	η (%)	FF (%)	V_{oc} (V)	J_{sc} (mA/cm^2)
(***n*** ,***m***) semiconducting	66	12.29	68.5	0.59	30.5
(***n***,***m***) metallic	41	14.23	76.7	0.62	29.8
(6,5) semiconducting	53	14.85	73.3	0.6	34
(7,4) metallic	50	13.83	70.8	0.59	33.2
Length enriched	47	12.89	71.1	0.58	31.2

The temperature dependence of J_0 provides additional insight into the nature of the junctions. Figure 27 shows the temperature response of a set of devices prepared from each sample type, where all heterojunctions considered in the remainder of the paper were prepared on 0.4 Ω cm substrates using the grid pattern of Figure 26a with 40-to-50 nm thick films. The inset to Figure 27a shows a fit of J_d to Eq. (3) under modest forward bias. The type dependence of n (inset, Figure. 27b) suggests that within this set of devices, the semiconducting SWCNTs form the least ideal junctions while the length-enriched CoMoCat SWCNTs form the most ideal. The junctions also become more ideal at higher temperature, which is similar to behavior reported for PN heterojunctions[37] but is also characteristic of Schottky junctions.[94] Figure 27c shows the temperature dependence of the extrapolated J_0, which is larger than that reported by Jung *et al*.[37] due to our somewhat higher ideality factors. The deviation of the measured dark current from Eq. (3) for $V < 0$ (Figure 27b) suggests that J_0 contains an additional bias dependence.

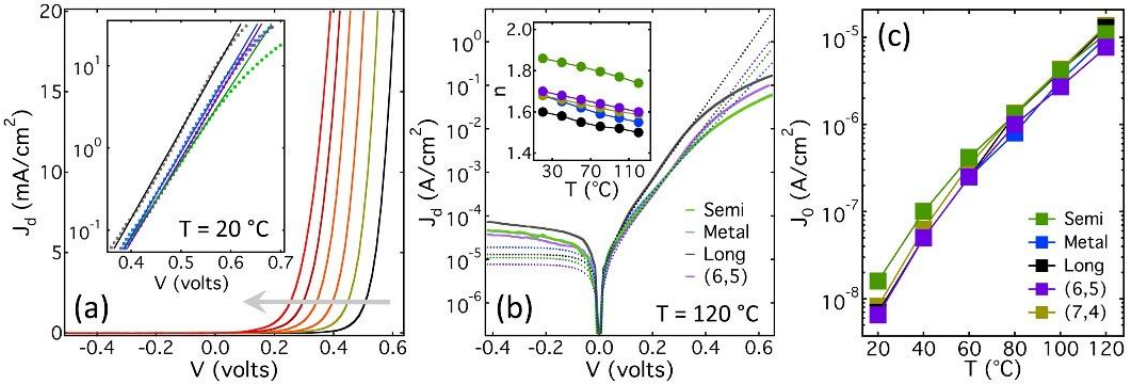

Figure 27: (a) J_d vs. bias for a length-enriched device from 20 °C up to 120 °C in 20 degree steps, where the arrow indicates increasing temperature. The inset shows the type dependence of J_d at 20 °C under forward bias with fits to Eq. (1) [green = semiconducting, blue = metallic, black = length enriched, purple = (6,5)]. (b) J_d vs. bias for different devices at 120 °C. The inset shows ideality factor vs. temperature for five devices, including a (7,4)-enriched film (yellow). (c) J_0 vs. temperature.

Focusing on the nature of the junctions, X-ray photoelectron spectroscopy (Appendix F) reveals a minimal post-processing Si-oxide layer (< 1 nm) under the relevant conditions while HF treatment is critical for performance. Plots of $n \ln J_0$ vs. T^{-1} (Figure 28a) suggest activation energies that appear to be incompatible with the band gap of Si.[37] At first glance, these two results are difficult to reconcile with either PN or MIS behavior in the conventional sense.

Turning to Schottky behavior, a Richardson plot of each device in Figure 27 yields an effective barrier height (Φ_0) and an apparent Richardson constant (A^*). This is done by taking the logarithm of the expression for the saturation current in the diode equation, which linearizes the expression with respect to temperature. and extracting values though the resulting linear fit. Repeating such measurements for many devices gives Φ_0 and A^* vs. ideality, n (Figure 29b-c). Such plots suggest that all SWCNT types/chiralities form the same class of junction but with significant barrier height inhomogeneity.[96] The range of n is not surprising given our simple fluid process, but the average ideality ranking is (6,5), long, metal, (7,4) and semi. Extrapolating to n = 1 gives a barrier height of 1.01 eV and a Richardson constant of 20 A/cm^{2}K^2, where the latter can be rationalized with the A^* value for n-type Si (110 A/cm^{2}K^2) through an effective area fraction of 20 %. Physically, this represents the minimum fraction of bundles that can make ideal contact with the underlying Si, consistent with the rough morphology of the films.[50,73,94,97]

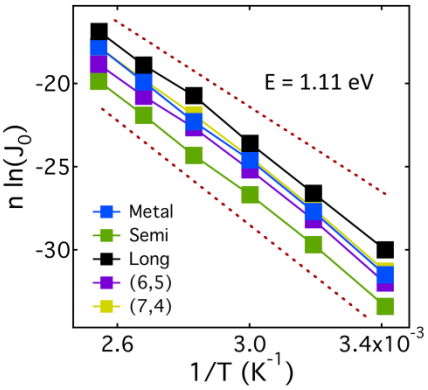

Figure 28: Activation energy plot for J_o, referenced to the band gap of Silicon (1.11 eV) (dotted).

Figure 29d shows measured J_d at 20 °C for a number of devices, with the more ideal junctions represented by solid curves. Remarkably, the smallest magnitude (10^{-6} A/cm^2) is comparable to CVD graphene-Si Schottky junctions with n = 1.08.[78] Capacitance measurements of typical junctions plotted as C^{-2} vs. V (Figure 30) are linear and yield a built-in voltage (V_{bi}) close to 0.6 V with only weak type variation in V_{bi} or slope. Assuming Schottky behavior,[98] the donor density obtained from slope and active area ($N_D \approx 1.8 \times 10^{16}$ cm^{-3}) agrees with the value expected for the 0.4 Ω cm substrates. When compared to the corresponding Φ_0, the independently determined V_{bi} are also consistent with a Si donor level just below the conduction band, as expected. The magnitude of the extrapolated ideal barrier height is significantly larger than the value of 0.62 V reported for nearly ideal CVD graphene on n-Si,[78] which is expected given the non-ideal fluid-processed nature of our junctions. All of these observations point to the band diagrams in Figure 29e-f, where doping leads to a semiconducting band structure that qualitatively resembles that of the metals.

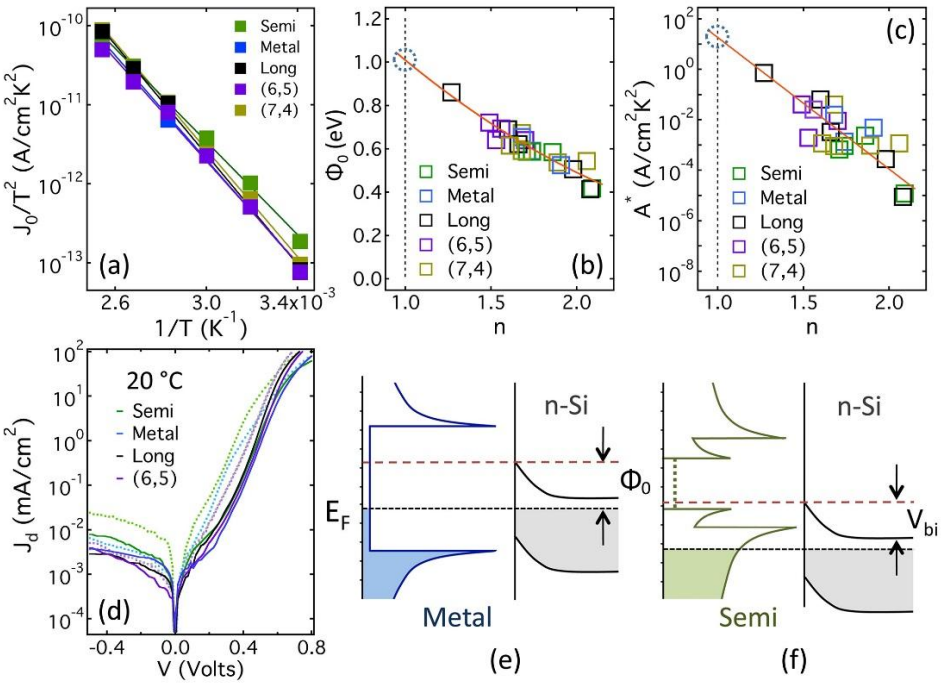

Figure 29: (a) Richardson plot for the set of devices in Figure 5. (b) Barrier height as a function of room-temperature ideality with a weakly quadratic fit, and (c) an analogous plot of Richardson constant with an exponential fit. (d) Measured J_d vs. V for a number of devices at 20 °C, where the solid curves represent the more ideal diodes. (e) Band diagrams of the metallic and (f) semiconducting junctions. The vertical dashed line in (f) denotes doping-induced states.

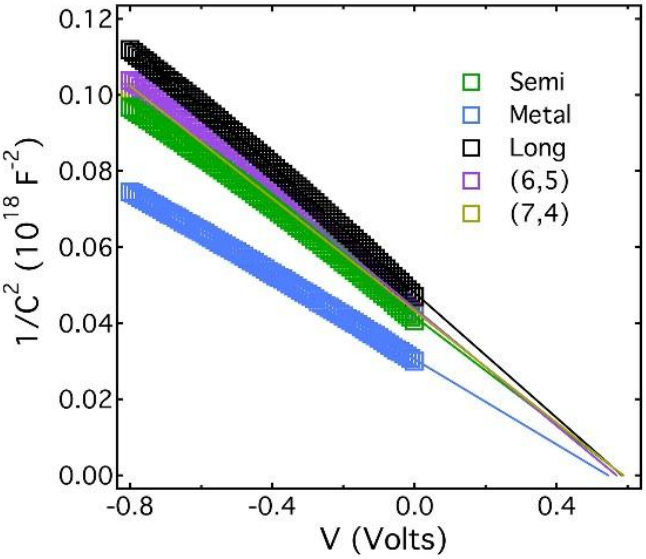

Figure 30: Inverse squared capacitance vs. potential. Linear fits were used to extrapolate the built-in potential.

Within the Schottky-junction interpretation, the magnitude of the barrier height with respect to the band gap of Si suggests that the Fermi level is not completely pinned. Neglecting image-charge barrier lowering and taking 4.05 eV for the electron affinity of Si, the data imply a SWCNT work function of 5.07 eV independent of type or chirality, in close agreement with theoretical predictions for nanotube bundles.[99] Turning to J_d under negative bias, the trends (Figure 31a-b) are incompatible with the $\sqrt{V_{bi} - V}$ behavior typical of diffusion-dominated transport or the $\exp[c(V_{bi} - V)^{1/4}]$ behavior expected for image-charge barrier lowering.[98] Instead, they are consistent with a nearly linear decrease in barrier height; $\Phi(V) = \Phi_0 - \Delta\Phi(V)$ with $\Delta\Phi(V) \propto |V|$. From the fits in Figure 31a-b (which require a value of J_0 roughly two orders of magnitude larger than that obtained for modest $V > 0$ in Figure 27) $|\Delta\Phi|/\Phi_0$ is 7.3 % (semi), 7.7 % (6,5), 2.8 % (metal), and 4.8 % (long) at -0.5 V. This is reminiscent of graphene-Si Schottky junctions, where an absence of Fermi-level pinning and a finite DOS near the Dirac point lead to an upward shift in E_F due to extrinsic doping under negative bias.[78] Specifically, the incremental charge per unit area is $q\Delta N = c_j(V)V$ with $dE_F/dN \approx g^{-1}(E_F)$, where c_j is the areal capacitance.

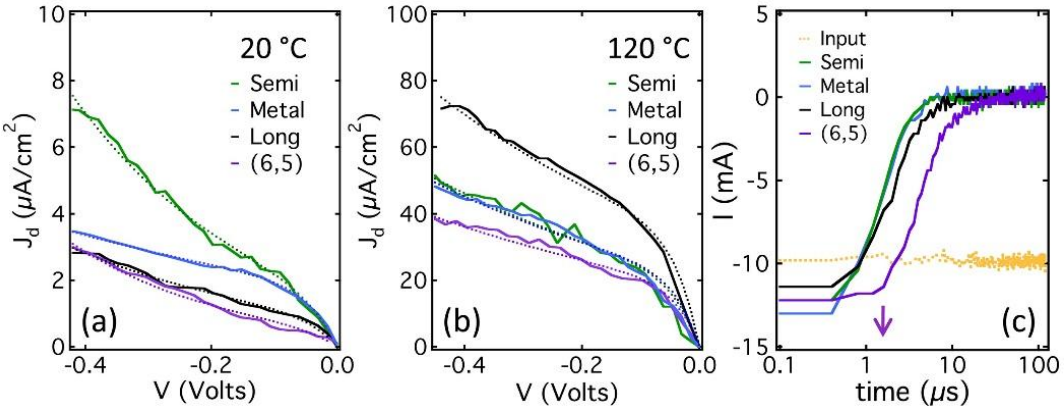

Figure 31: (a) Dark currents for the more ideal devices with fits (dashed curves) as detailed in the text and (b) an analogous plot at 120 °C. (c) Room temperature reverse-transient recovery.

Although the DOS at the Fermi level is unclear for the semiconducting nanotubes, we can apply this analysis to the metallic SWCNTs because $g(E_F)$ is relatively unchanged by doping.

Using $g(E) = 2Ln_A/\pi v_F$ (where v_F is the Fermi velocity, L is nanotube length, and n_A is areal SWCNT density) gives us $\Delta\Phi = \Delta E_f \approx \pi v_F c_j |V|/2qLn_A$ which explains the linearity of $\Delta\Phi(V)$. Using the measured c_j and $L \approx 350$ nm, the 2.8 % reduction in barrier height at -0.5 V implies 2×10^{10} SWCNT/cm^2, which is much smaller than $(dL)^{-1}$ where $d \approx 1$ nm is SWCNT diameter. Again, this is consistent with limited contact due to film roughness.

While the evidence for Schottky behavior is compelling, there are other aspects of these devices that significantly cloud this interpretation. Reverse transient recovery measurements can, in general, provide a direct probe of minority carrier recombination.[100] Here, such data (Figure 31c) show a finite recovery time and even a measurable storage time (t_s) for the (6,5) films. Although the metallic films have much larger sheet resistance, the former is still significantly larger than the *RC* time constant of the equivalent circuit, indicating the diffusion/depletion of minority carriers (holes). For the (6,5) device in Figure 5.9c, the measureable t_s yields a minority carrier recombination time on the order of 1-2 μs.[100] While this is smaller than the reported lifetime of 30 μs measured by Jung *et al.* in the limit of near ideality,[37] it is inconsistent with a Schottky junction, which would be a majority carrier device with switching times dictated by *RC*. The extrapolated ideal barrier height is also remarkably close to the band gap of Si (1.11 eV), which is consistent with the activation energy obtained by Jung *et al*. in the near-ideal limit.[37] Finally, the magnitude of *V*oc is 0.5-to-0.6 V or larger regardless of ideality or barrier height, which is also incompatible with conventional Schottky behavior.

Taken collectively, our results demonstrate that these devices do not fit neatly into either of the two conventionally distinct descriptions, but instead straddle an interface between the two. This would likely explain the diversity of interpretations reported in the literature, but it points to a unique classification for nanotube-silicon heterojunctions. The fact that these diodes can

simultaneously exhibit both Schottky and p-n behavior is not surprising, given a unique SWCNT band structure that differs significantly from that of a bulk metal or doped semiconductor through van Hove singularities in the DOS near the top of the valence band and the bottom of the conduction band. An obvious point of reference in this regard is an abrupt p+-n or *high-blocked* heterojunction, where the metal layer is replaced with a thin heavily hole-doped semiconductor layer but the basic description is the same as a Schottky junction.[101] Greater gliding of the electron density at the junction interface imparts more steepness to the I-V curve and hence higher V_{oc}, while the minority carrier lifetime defines an effective diffusion velocity that simply replaces the thermal electron velocity in the Schottky picture.

5.1. Conclusions

Our results demonstrate that SWCNT type and chiral purification can improve the performance of SWCNT-Si heterojunctions. Using an identical process to make devices from a CoMoCat parent, for example, the best PCE we achieved was 11.5 %. Much of this is simply due to improved transparency associated with the elimination of inter-band optical resonances, but the magnitude of the saturation current could have an impact as well. In this regard, morphological changes designed to increase contact area and homogenize barrier height - such as SWCNT alignment and/or a transparent conductive host matrix - should lead to more ideal behavior and a reduction in J_0 . Although this suggests the possibility that we have not yet hit the performance ceiling, we suspect that we are reasonably close for the simple device configurations considered here. Adding an antireflective coating[77] or moving to a large-array hole geometry,[74] for example, should further improve efficiency. We also postulate that more ideal behavior will enhance minority carrier contributions (i.e., lead to longer recombination time) and bring out characteristics more typical of PN junctions. For the devices detailed here,

the superior performance of the metallic and (6,5) semiconducting films stems from improved transparency with respect to the solar spectrum and larger Φ_0. The poorer performance of the large-diameter semiconducting films is due to lower transmission near the maximum of the solar spectrum and smaller Φ_0 (higher nonideality, Figure 29b), where the latter leads to a larger saturation current (Figure 29d).

Another surprising result is the stability of the films during fluid processing. Previous studies of the wrinkling and folding of comparable films compressed on polydimethylsiloxane (PDMS) reveal significant plasticity and strain softening through vdW bundling.[50,73,94,97] Such effects are absent here, which could possibly be due to screening of vdW forces by solvents and reduced in-plane compression associated with the large-amplitude bending of a freestanding sheet. Other effects such as surface charge may be at play, though an in-depth study is needed. Over time, the metallic films degrade under repeated pipette handling while the semiconducting films remain robust. While this is the opposite of previous compression studies, [50,73,94,97] the nature of the deformation here is different. It is has the same root cause, however; the metallic SWCNTs have weaker vdW attraction than the semiconducting SWCNTs,[102] which is what ultimately enables separation.[103]

Although devices that rely on chemical doping are typically unstable - and our current efforts are focused on maximizing PCE and optimizing ideality - useful insight in this regard comes from recent devices that exhibit long-term photoconversion stability in air. All of these are fabricated from chemical-vapor-deposition SWCNTs that have undergone minimal post processing and hence likely contain residual metal catalyst. Such nanoparticle ‘impurities’ could play a role analogous to the chemical dopants used here, which suggests using nanoparticles, gels

or polymer complexes as dopant to improve chemical stability, an approach we are currently exploring.

5.2. Future Outlook

The future outlook for NSH devices depends strongly on the evolution of the SWCNT fabrication process, since current SWCNT synthesis methods are both expensive and time consuming. These devices have yet to reach the point of economic feasibility, due mostly to the expensive SWCNT fabrication process. These solar cells could become more economical with the implementation of industrial scale production, increasing their future potential.

A second hurdle to the future outlook of these NSH devices is the question of stability after chemical functionalization. To generate the exceptional performance of these solar cells, chemical functionalization of the SWCNT film is required. Unfortunately, this process is very much temporary and performance enhancements are observed to last less than 24 hours before detrimental declines in device performance appear. Some groups have tried to circumnavigate this problem through the addition of a thin-film capping layer designed to trap the dopants within the SWCNT network;[35-37,77] while other groups have had success in stabilizing devices to be high performing in air through the absence of chemical functionalization.[75]

In addition to these hurdles, modeling the band structure for a NSH device has proven difficult through the highly complex superposition of chirality-dependent band structures within the SWCNT film. This complexity results in a charge separation and transport mechanism that is poorly understood at present. It will only be through the discovery of high-output fabrication methods, an increased understanding of the underlying device band structure, and improved understanding of the mechanism behind high-efficiency non-functionalized devices that this technology might be fully optimized.

REFERENCES

1. Ohl, R.S., “Light Sensitive Electric Device.” US Patent 240,252 (27 March 1941).
2. Pearson GL. PV founders award luncheon. Conference Record, 18th IEEE Photovoltaic Specialists Conference, Las Vegas, IEEE, New York, (1985).
3. Bell Laboratories Record, May, **166**, 166, (1955).
4. Mandelkorn, J., McAfee, C., Kesperis, J., Schwartz, L., and Pharo, W., “Fabrication and Characteristics of Phosphorus-Diffused Silicon Solar Cells.” J Electrochemical Soc, **109**, 313–318 (1962).
5. “Terrestrial Photovoltaic Measurement Procedures. Report ERDA/NASA”, 1022–1077, (16 June 1977).
6. Green, M.A., Emery, K., Hishikawa, Y., and Warta, W., “Solar Cell Efficiency Tables (version 33)”. Progress in Photovoltaics, **17**, 85–94l, (2009).
7. Hishikawa, Y., “Revision of the Reference Solar Spectrum: the Influence on the PV Performance Measurements.”, Paper presented at Renewable Energy Conference, Busan, Korea, (13–17 October 2008).
8. Gueymard, C., "Parameterized Transmittance Model for Direct Beam and Circumsolar Spectral Irradiance." Solar Energy, **71**, 5, 325–346, (2001).
9. Gueymard, C., "SMARTS, A Simple Model of the Atmospheric Radiative Transfer of Sunshine: Algorithms and Performance Assessment." FSEC-PF, **270,** 95 (1995).
10. Green, M. A., “The Path to 25% Silicon Solar Cell Efficiency: History of Silicon Cell Evolution”, Prog. Photovolt. Res. Appl., **17**, 183–189, (2009).
11. Green, M. A., “Silicon Solar Cells: Evolution, High Efficiency Design and Efficiency Enhancements”, Semicond. Scl. Technol. **8**, 1-12, (1993).

12. Shockley, W. and Queisser, H. J. , "Detailed Balance Limit of Efficiency of P-N Junction Solar cells." J. Appl. Phys, **32**, 510-519, (1961).

13. Gabor, N. M., Zhong, Z., Bosnick, K., Park, J., and McEuen,P. L., "Extremely Efficient Multiple Electron-Hole Pair Generation in Carbon Nanotube Photodiodes", Science, **325**, 5965, 1367-1371, (11 September 2009).

14. Cao, Q. and Rogers, J. A., "Ultrathin Films of Single-Walled Carbon Nanotubes for Electronics and Sensors: A Review of Fundamental and Applied Aspects.", Adv. Mater., **21**, 29–53, (2008).

15. Hu, L., Hecht, D. S., and Grüner, G., "Carbon Nanotube Thin Films: Fabrication, Properties, and Applications." Chem. Rev., **110**, 5790– 844, (2010).

16. Kis, A. and Zettl,A., "Nanomechanics of Carbon Nanotubes." Phil. Trans. R. Soc. A, **366**, 1591–1611, (2008).

17. Zhang, D. B. and Dumitric, T., "Elasticity of Ideal Single-Walled Carbon Nanotubes via Symmetry-Adapted Tight-Binding Objective Modeling." Appl. Phys. Lett., **93**, 031919, (2008).

18. Iijima, S., "Helical Microtubules of Graphitic Carbon", Nature **354**, 56-58 (1991).

19. Saito, R.., Fujita, M., Dresselhaus, G., and Dresselhaus, M.S., "Electronic Structure of Chiral Graphene Tubules", Appl. Phys. Lett., **60**, 2204-2206, (1992).

20. Kataura, H., Kumazawa, Y., Maniwa, Y., Umezu, I., Suzuki, S., Ohtsuka, Y., and Achiba, Y., "Optical Properties of Single-Wall Carbon Nanotubes", Synth. Met., **103**, 2555-2558, (1999).

21. Calvert, P., "Nanotube Composites: A Recipe for Strength", Nature, **399**, 210-211, (1999)

22. Odom, T.W., Huang, J.L., Kim, P., and Lieber, C.M., "Atomic Structure and Electronic Properties of Single-Walled Carbon Nanotubes ", Nature, **391**, 62-64, (1998).

23. Murakami, Y., Einarsson, E., Edamura, T., and Maruyamaet, S., "Polarization Dependence of the Optical Absorption of Single-Walled Carbon Nanotubes", Phys. Rev. Lett., **94**, 087402, (2005).

24. Fujiwara, A., Matsuoka, Y., Suematsu, H., Ogawa, N., Miyano, K., Kataura, H., Maniwa, Y., Suzuki, S., and Achiba, Y., "Photoconductivity in Semiconducting Single-Walled Carbon Nanotubes", Jpn. J. Appl. Phys., **40**, 1229-231, (2001).

25. V. Sgobba,G. M. A. Rahman, D. M. Guldi, N. Jux, S. Campidelli, and M. Prato, "Supramolecular Assemblies of Different Carbon Nanotubes for Photoconversion Processes", Adv. Mater., **18**, 2264-2269, (2006).

26. Tezuka, N., Umeyama, T., Seki, S., Matano, Y., Nishi, M., Hirao, K., and Imahori, H., "Carbon Nanotube Wiring of Donor–Acceptor Nanograins by Self-Assembly and Efficient Charge Transport", J. Phys. Chem. C, **114**, 3235-3247, (2010).

27. Rahman, G. M. A., Guldi, D. M., R. Cagnoli, A. Mucci, L. Schenetti, L. Vaccari, and M. Prato, "Combining Single-Wall Carbon Nanotubes and Photoactive Polymers for Photoconversion." J. Am. Chem. Soc., **127**, 10051-10057, (2005).

28. H. Imahori and T. Umeyama, "Donor-Acceptor Nanoarchitecture on Semiconducting Electrodes for Solar Energy Conversion.", J. Phys. Chem. C, **113**, 9029-9039 (2009).

29. D'Souza, F. and Sandanayaka, A. S. D., Ito, O.," SWNT-Based Supramolecular Nanoarchitectures with Photosensitizing Donor and Acceptor Molecules", J. Phys. Chem. Lett., **1**, 2586-2593, (2010).

30. Wei, J., Jia, Y., Shu, Q., Gu, Z., Wang, K., Zhuang, D., Zhang, G., Wang, Z., Luo, J., Cao, A., and Wu, D., "Double-Walled Carbon Nanotube Solar Cells", Nano Lett., **7**, 2317-2321, (2007).

31. Hu, L., Hecht, D.S. and Gruner, G., "Percolation in Transparent and Conducting Carbon Nanotube Networks", Nano Lett., **4**, 2513-2517, (2004).

32. Behnam, A., Johnson, J. L., Choi, Y., Ertosun, M. G., Okyay, A. K., Kapur, P., Saraswat, K. C., and Ural, A., "Experimental Characterization of Single-Walled Carbon Nanotube Film-Si Schottky Contacts Using Metal-Semiconductor-Metal structures", Appl. Phys. Lett. **92**, 243116 (2008)

33. Li, Z., Kunets, V.P., Saini, V., Xu, Y., Dervishi, E., Salamo, G.J., Biris, A.R. and Biris, A.S., "$SOCl_2$ Enhanced Photovoltaic Conversion of Single Wall Carbon Nanotube/n-Silicon Heterojunctions", Appl. Phys. Lett., **93**, 243117, (2008).

34. Li, Z., Kunets, V.P., Saini, V., Xu, Y., Dervishi, E., Salamo, G.J., Biris, A.R. and Biris, A.S., "Light-Harvesting Using High Density p-Type Single Wall Carbon Nanotube/n-Type Silicon Heterojunctions", ACS Nano, **3**, 1407-1414, (2009).

35. Jia, Y., Cao, A., Bai, X., Li, Z., Zhang, L., Guo, N., Wei, J., Wang, K., Zhu, H., Wu, D. and Ajayan, P. M., "Achieving High Efficiency Silicon-Carbon Nanotube Heterojunction Solar Cells by Acid Doping", Nano Lett., **11**, 1901-1905, (2011).

36. Jia, Y., Li, P., Gui, X., Wei, J., Wang, K., Zhu, H., Wu, D., Zhang, L., Cao, A. and Xu, Y.,"Encaspulated Carbon Nanotube-Oxide-Silicon Solar Cells with Stable Efficiency", Appl. Phys. Lett., **98**, 133115, (2011).

37. Jung, Y., Li, X., Rajan, N.K., Taylor, A.D. and Reed, M.A., "Record High Efficiency Single-Walled Carbon Nanotube/Silicon P-N Junction Solar Cells", Nano Lett., **13**, 95-99, (2013).

38. Li, X., Jung, Y., Sakimoto, K., Goh, T.H., Reed, M.A. and Taylor, A.D., "Improved Efficiency of Smooth and Aligned Single Walled Carbon Nanotube/Silicon Hybrid Solar Cells", Energy Environ. Sci., **6**, 879-887, (2013).

39. Tune, D.D., Flavel, B.S., Krupke, R. and Shapter, J. G., "Carbon Nanotube-Silicon Solar Cells", Adv. Energy Mater., **2**, 1043-1045, (2012).

40. Castrucci. P., "Carbon Nanotube/Silicon Hybrid Heterojunctions for Photovoltaic Devices", Adv. Nano Res., **2**,1, 23-56, (2014).

41. Tune, D. D., and Shapter, J. G., "Effect of Nanotube Film Thickness on the Performance of Nanotube-Silicon Hybrid Solar Cells", Nanomaterials, **3**, 655-673, (2013).

42. Harris, J. M., Semler, M. R., Fagan, J. A., May, S,. and Hobbie, E. K. "The Nature of Record Efficiency Fluid-Processed Nanotube-Silicon Heterojunctions." J. Chem. Phys. DOI**:** 10.1021/acs.jpcc.5b02626, (2015).

43. Saito, R., Dresselhaus, G., and Dresselhaus, M. S., "Physical Properties of Carbon Nanotubes", World Scientific, Singapore, (1998)

44. Scott, C.D., Arepalli, S., Nikolaev, P., Smalley, R.E. "Growth Mechanisms for Single-Wall Carbon Nanotubes in a Laser-Ablation Process" J Appl. Phys. A, **72**,574-580, (2001).

45. Shi, Z., Lian, Y., Liao, F. H., Zhou, X., Gu, Z., Zhang, Y., Iijima S., Li, H., Yue, K.T., Zhang, S.L; "Large Scale Synthesis of Single-Wall Carbon Nanotubes by Arc-Discharge Method" J. Phys. Chem. Solids, **61**, 1031-1036, (2000).

46. Resasco, D.E., Alvarez, W.E., Pompeo, F., Balzano, L., Herrera, J.E., Kitiyanan, B. and Borgna, A., "A Scalable Process for Production of Single-Walled Carbon Nanotubes by Catalytic Disproportionation of CO on a Solid Catalyst" J. Nanopart. Res., **4,** 131-136, (2002).

47. Blackburn, J. L.; Barnes, T. M.; Beard, M. C.; Kim, Y.-H.; Tenent, R. C.; McDonald, T. J.; To, B.; Coutts, T. J.; Heben, M. J. "Transparent Conductive Single-Walled Carbon Nanotube Networks with Precisely Tunable Ratios of Semiconducting and Metallic Nanotubes." ACS Nano, **2**, 1266–1274, (2008).

48. Fagan, J. A., Becker, M. L., Chun, J., Nie, P., Bauer, B. J., Simpson, J. R., Walker, A. R. H., and Hobbie, E. K., "Centrifugal Length Separation of Carbon Nanotubes" Langmuir, **24**, 13880-13889, (2008).

49. Fagan, J. A., Zheng, M., Rastogi, V., Simpson, J. R., Khripin, C. Y., Batista, C. A. S., and Walker, A. R. H., "Analyzing Surfactant Structures on Length and Chirality Resolved (6,5) Single-Wall Carbon Nanotubes by Analytical Ultracentrifugation" ACS Nano, **7**, 3373-3387, (2013).

50. Harris, J. M., Iyer, S.G.R., Hobbie E.K., Bernhardt, A.K., Huh J.Y., Hudson S.D., and Fagan J.A., "Electronic Durability of Flexible Transparent Films from Type-Specific Single-Wall Carbon Nanotubes" ACS Nano, **6**,881-887, (2012).

51. Frank, D. J. and Lobb, C. J., "Highly Efficient Algorithm for Percolative Transport Studies in Two Dimensions. Phys. Rev. B, **37**, 302–307, (1988).

52. Laugier, J. M., Clerc, J. P., Giraud, G., and Luck, J. M., "AC Properties of 2D Percolation Networks: A Transfer Matrix Approach." J. Phys. A: Math. Gen., **19**, 3153–3164, (1986).

53. Lajk, P. and Turban, L., "Percolation and Conduction in Restricted Geometries.", J. Phys. A., **33**, 1683–1692, (2000).

54. Kurti, J., Zolyomi, V., Kertesz, M., Sun, G., "The Geometry and the Radial Breathing Mode of Carbon Nanotubes: Beyond the Ideal Behavior" New Journal of Physics, **5**, 125, 1-21, (2003)

55. Jishi, R. A., Venkataraman, L., Dresselhaus, M. S., and Dresselhaus, G., "Phonon Modes in Carbon Nanotubules" Chem. Phys. Lett., **209**, 77-82, (1993)

56. Jorio, A., Saito, R., Hafner, J. H., Lieber, C. M., Hunter, M., McClure, T., Dresselhaus, G. and Dresselhaus, M. S., "Structural (n,m) Determination of Isolated Single-Wall Carbon Nanotubes by Resonant Raman Scattering", Phys. Rev. Lett., **86**, 1118 , (2001).

57. Collins, P.G., Bradley, K., Ishigami, M. and Zettl, A., "Extreme Oxygen Sensitivity of Electronic Properties of Carbon Nanotubes", Science, **287**, 1801-1804, (2000).

58. Kim, K. K., Bae, J. J., Park, H. K., Kim, S. M., Geng, H., Park, K. A., Shin, H., Yoon, S., Benayad, A., Choi, J., and Lee, Y. H., "Fermi Level Engineering of Single-Walled Carbon Nanotubes by $AuCl_3$ Doping." , J. Am. Chem. Soc., **130**, 12757-12761, (2008).

59. Kim, S. M., Kim, K. K., Jo, Y. W., Park, M. H., Chae, S. J., Duong, D. L., Yang, C. W., Kong, J., and Lee, Y. H., "Role of Anions in the AuCl3-Doping of Carbon Nanotubes." ACS Nano, **5**, 1236-1242, (2011).

60. Duong, D. L., Lee, I. H., Kim, K. K., Kong, J., Lee, S. M., and Lee, Y. H., "Carbon Nanotube Doping Mechanism in a Salt Solution and Hygroscopic Effect: Density Functional Theory." ACS Nano, **4**, 5430-5436, (2010).

61. Tune, D. D., Blanch, A. J., Krupke, R., Flavel, B. S., and Shapter J. G., "Nanotube Film Metallicity and its Effect on the Performance of Carbon Nanotube-Silicon Solar Cells. Phys. Status Solidi A, **211**, 1479-1487, (2014)

62. Crochet, J. J., Duque, J. G., Werner, J. H., and Doorn, S. K., "Photoluminescence Imaging of Electronic Impurity-Induced Exciton Quenching in Single-Walled Carbon Nanotubes.", Nat. Nanotechnol., **7**, 126-132, (2012).

63. Kern, W., "The Evolution of Silicon Wafer Cleaning Technology". J Electrochem. Soc. **137**, 6, 1887–1892, (1990).

64. Thess, A., Lee, R., Nikolaev, P., Dai, H., Petit, P., Robert, J., Xu, C., Lee. Y. H., Kim, S. G., Rinzler, A. G., Colbert, D. T., Scuseria, G. E., Tomrinek, D., Fischer, J. E., and Smalley, R. E., "Crystalline Ropes of Metallic Carbon Nanotubes", Science, **273**, 483-487 (1996).

65. Cowley, J. M., Nikolaev, P., Thess, A., and Smalley, R. E., "Electron Nano-Diffraction Study of Carbon Single-Walled Nanotube Ropes", Chem. Phys. Lett. **265**, 379-384 (1997).

66. Arnold, M. S., Green, A. A., Hulvat, J. F., Stupp, S. I., and Hersam, M. C., "Sorting Carbon Nanotubes by Electronic Structure Using Density Differentiation", Nature Nano., **1**, 60-65, (2006).

67. Ghosh, S., Bachilo, S. M., Weisman, R. B., "Advanced Sorting of Single-Walled Carbon Nanotubes by Nonlinear Density-Gradient Ultracentrifugation", Nature Nano., **5**, 443-450 (2010).

68. Miller, J. B., Harris, J. M., and Hobbie, E. K., “Purifying Colloidal Nanoparticles through Ultracentrifugation with Implications for Interfaces and Materials” Langmuir, **30**, 7936-7946 (2014).

69. Fagan, J. A., Becker, M. L., Chun, J., Nie, P., Bauer, B. J., Simpson, J. R., Walker, A. R. H., and Hobbie, E. K., “Centrifugal Length Separation of Carbon Nanotubes.”, Langmuir, **24**, 13880-13889, (2008).

70. Fagan, J. A., Zheng, M., Rastogi, V., Simpson, J. R., Khripin, C. Y., Batista, C. A. S., and Walker, A. R. H., “Analyzing Surfactant Structures on Length and Chirality Resolved (6, 5) Single-Wall Carbon Nanotubes by Analytical Ultracentrifugation”, ACS Nano, **7**, 3373-3387, (2013).

71. Fagan, J. A., Khripin, C. Y., Silvera Batista, C. A., Simpson, J. R., Hároz, E. H., Hight-Walker, A. R., and Zheng, M., “Isolation of Specific Small-Diameter Single-Wall Carbon Nanotube Species via Aqueous Two-Phase Extraction”, Adv. Mater., **26**, 2800-2804, (2014).

72. Li, S. S., “Semiconductor Physical Electronics”, Springer, New York, (2006).

73. Harris, J. M., Huh, J. Y., Semler, M. R., Ihle, T., Stafford, C. M., Hudson, S. D., Fagan, J. A., and Hobbie, E. K., "Elasticity and Rigidity Percolation in Flexible Carbon Nanotube Films on PDMS Substrates" Soft Matter, **9**, 11568-11575 (2013).

74. Wang, F., Kozawa, D., Miyauchi, Y., Hiraoka, K., Mouri, S., Ohno, Y., and Matsuda, K., “Fabrication of Single-Walled Carbon Nanotube/Si Heterojunction Solar Cells with High Photovoltaic Performance.”, ACS Photonics, **1**, 360-364, (2014).

75. Cui, K., Anisimov, A. S., Chiba, T., Fujii, S., Katuara, H., Nasibulin, A. G., Chiashi, S., Kauppinen,E. I., and Maruyama, S., "Air-Stable High-Efficiency Solar Cells with Dry-Transferred Single-Walled Carbon Nanotube Films.", J. Mater. Chem. A, **2**, 11311-11318, (2014).

76. Li, R., Di, J., Yong, Z., Sun, B., and Li, Q., "Polymethylmethacrylate Coating on Aligned Carbon Nanotube-Silicon Solar Cells for Performance Improvement." J. Mater. Chem. A, **2**, 4140-4143, (2014).

77. Shi, E., Zhang, L., Li, Z., Li, P., Shang, Y., Jia, Y., Wei, J., Wang, K., Zhu, H., Wu, D., Zhang, S., and Cao, A., "TiO2-Coated Carbon Nanotube-Silicon Solar Cells with Efficiency of 15 %.", Sci. Rep., **2**, 884(2012).

78. Sinha, D. and Lee, J. U., "Ideal Graphene/Silicon Schottky Junction Diodes." Nano Lett., **14**, 4660-4664, (2014).

79. Miao, X., Tongay, S., Petterson, M. K., Berke, K., Rinzler, A. G., Appleton, B. R., and Hebard, A. F., "High Efficiency Graphene Solar Cells by Chemical Doping.", Nano Lett., **12**, 2745-2750, (2012).

80. Li, X., Zhu, H., Wang, K., Cao, A., Wei, J., Li, C., Jia, Y., Li, Z., Li, X., and Wu, D., "Graphene-on- Silicon Schottky Junction Solar Cells.", Adv. Mater., **22**, 2743-2748, (2010).

81. Shi, E., Li, H., Yang, L., Zhang, L., Li, Z., Li, P., Shang Y., Wu, S., Li, X., Wei, J., Wang, K., Zhu, H., Wu, D., Fang, Y., and Cao A. "Colloidal Antireflection Coating Improves Graphene–Silicon Solar Cells," Nano Lett., **13**, 1776-1781, (2013).

82. Xie, C., Zhang X,, Ruan K., Dhaliwal, S. S., Wang, Liu., Zhang Q., Zhang, X., and Jie, J., "High-Efficiency Air Stable Graphene/Si Micro-Hole Array Schottky Junction Solar Cells.", J. Mater. Chem. A, **1**, 15348-15354, (2013).

83. Won, R., "Photovoltaics: Graphene-Silicon Solar Cells.", Nature Photonics, **4**, 411, (2010).

84. Liu, X., Zhang, X. W., Yin, Z. G., Meng, J. H., Gao, H. L., Zhang, L. Q., Zhao, Y. J., and Wang, H. L. "Enhanced Efficiency of Graphene-Silicon Schottky Junction Solar cells by Doping with Au Nanoparticles." Appl. Phys. Lett., **105**, 183901, (2014).

85. Zhang, X., Xie, C., Jie, J., Zhang, X., Wua, Y., and Zhang, W., "High-Efficiency Graphene/Si Nanoarray Schottky Junction Solar Cells via Surface Modification and Graphene Doping." J. Mater. Chem. A, **1**, 6593-6601, (2013).

86. Yu, X., Yang, L., Lv, Q., Xu, M., Chen, H., and Yang, D., "The Enhanced Efficiency of Graphene-Silicon Solar Cells by Electric Field Doping." Nanoscale (2015)

87. Wadhwa, P., Liu, B., McCarthy, M. A., Wu, Z., and Rinzler, A. G., "Electronic Junction Control in a Nanotube-Semiconductor Schottky Junction Solar Cell." Nano Lett., **10**, 5001-5005, (2010).

88. Wadhwa, P., Seol, G., Petterson, M. K., Guo, J., and Rinzler, A. G., "Electrolyte-Induced Inversion Layer Schottky Junction Solar Cell." Nano Lett., **11**, 2419-2423, (2011).

89. Behnam, A., Radhakrishna, N. A., Wu, Z., and Ural, A., "Electronic Properties of Metal-Semiconductor and Metal-Oxide-Semiconductor Structures Composed of Carbon Nanotube Films on Silicon." Appl. Phys. Lett., **97**, 233105, (2010).

90. Li, X., Jung, Y., Huang, J. S., Goh, T., and Taylor, A. D., "Device Area Scale-Up and Improvement of SWCNT/Si Solar Cells using Silver Nanowires." Adv. Energy Mater., **4**, 1400186, (2014).

91. Jia, Y., Cao, A., Kang, F., Li, P., Gui, X., Zhang, L., Shi, E., Wei, J., Wang, K., Zhu, H., and Wu, D., "Strong and Reversible Modulation of Carbon Nanotube-Silicon Heterojunction Solar Cells by an Interfacial Oxide Layer." Phys. Chem. Chem. Phys., **14**, 8391-8396, (2012).

92. Pintossi, C., Salvinelli, G., Drera, G., Pagliara, S., Sangaletti, L., Del Gobbo, S., Morbidoni, M., Scarselli, M., De Crescenzi, M., and Castrucci, P., "Direct Evidence of Chemically Inhomogeneous, Nanostructured, Si-O Buried Interfaces and Their Effect on the Efficiency of Carbon Nanotubes/Si Photovoltaic Heterojunctions." J. Phys. Chem. C, **117**, 36, 18688-18696, (2013).

93. Le Borgne, V., Gautier, L. A., and El Khakani, M. A., "Figure of Merit Based Maximization of the Quantum Efficiency of (Single-Wall Carbon Nanotube/n-type Silicon) Hybrid Photovoltaic Devices." Appl. Phys. Lett., **103**, 073103,(2013).

94. Hobbie, E. K., Simien, D. O., Fagan, J. A., Huh, J. Y., Chung, J. Y., Hudson, S. D., Obrzut, J., Douglas, J. F., and Stafford, C. M., "Wrinkling and Strain Softening in Single-Wall Carbon Nanotube Membranes.", Phys. Rev. Lett., **104**, 125505, (2010).

95. Hudait, M. K., Venkateswarlu, P., and Krupanidhi, S. B., "Electrical Transport Characteristics of Au/n-GaAs Schottky Diodes on n-Ge at Low Temperatures.", Solid-State Electron., **45**, 133-141, (2001).

96. Tung, R. T., "Electron Transport at Metal-Semiconductor Interfaces: General Theory." Phys. Rev. B, **45**, 13509-13523, (1992).

97. Semler, M. R., Harris, J. M., and Hobbie, E. K., "Wrinkling and Folding of Nanotube-Polymer Bilayers." J Chem. Phys., **141**, 044901, (2014).

98. Sze, S. M. and Ng, K. K., "Physics of Semiconductor Devices", Wiley, New York, (2007).

99. Zhao, J., Han, J., and Lu, J. P., "Work Functions of Pristine and Alkali-Metal Intercalated Carbon Nanotubes and Bundles.", Phys. Rev. B, **65**, 193401, (2002).

100. Jung, Y., Vacic, A., Perea, D. E., Picraux, S. T., and Reed, M. A., "Minority Carrier Lifetimes and Surface Effects in VLS-Grown Axial P-N Junction Silicon Nanowires." Adv. Mater., **23**, 4306-4311, (2011).

101. Böer, K. W., "Introduction to Space Charge Effects in Semiconductors - Springer Series in Solid-State Sciences", Springer, Heidelberg, (2010).

102. Hobbie, E. K., Ihle, T., Harris, J. M., and Semler, M. R., "Empirical Evaluation of Attractive van der Waals Potentials for Type-Purified Single-Walled Carbon Nanotubes." Phys. Rev. B, **85**, 245439, (2012).

103. Jain, R. M., Tvrdy, K., Han, R., Ulissi, Z., and Strano, M. S., "Quantitative Theory of Adsorptive Separation for the Electronic Sorting of Single-Walled Carbon Nanotubes." ACS Nano, 8, 3367-3379, (2014).

APPENDIX A. NANOTUBE SEPARATION BY ELECTRONIC TYPE

Electronic type separation of the laser SWCNTs was performed using a method similar to Arnold et al.[1] and Yanagi et al.[2]. However, an additional step that separates the SWCNT population by the degree of water filling[3] was performed before type separation in a Beckman-Coulter VTI 65.2 vertical rotor for 1 h at 6800 rad/s and 20 °C with the following density layers: 1 mL of 18 % mass per volume iodixanol (5,5'-[(2-hydroxy-1-3 propanediyl)-bis(acetylamino)] bis [N,N'-bis(2,3dihydroxylpropyl-2,4,6-triiodo-1,3-benzenecarboxamide])), 1 % DOC; 3 mL of 9 % mass per volume iodixanol, 1 % DOC; 0.9 mL of 2 % DOC/SWCNTs. A consistent middle band containing the water-filled SWCNTs was collected and material from multiple runs was concentrated *via* forced filtration[4] to produce the parent population for type separation. Isolation of the water-filled nanotubes improves the yield of the electronic type separation, which was performed in a Beckman-Coulter SW-32 rotor for 19.25 h at 3350 rad/s and 20 °C. The solution layers for type separation were as follows: 1 mL of 40 % mass per volume iodixanol, 0.75 % sodium (dodecylsulfate) (SDS), 0.75 % sodium cholate (NaChol); 2 mL of purified SWCNTs in 32 % iodixanol, 1.125 % SDS, 0.5 % DOC; 20 mL of 30 % mass per volume iodixanol, 1.125 % SDS, 1.125 % NaChol. The water-filled SWCNTs used in the separation were allowed to equilibrate in the mixed surfactant environment for at least 4 days prior to separation. After separation, metallic and semiconducting fractions were collected and dialyzed repeatedly *via* forced filtration against a 30 kD membrane to exchange the SWCNTs into 1 % DOC and to increase the absolute SWCNT concentration.

A.1. References

1. Arnold, M. S., Green, A. A., Hulvat, J. F., Stupp, S. I., and Hersam, M. C., "Sorting carbon nanotubes by electronic structure using density differentiation", Nature Nanotech., **1**, 60-65, (2006).
2. Yanagi, K.., Miyata, Y., and Kataura, H., "Optical and Conductive Characteristics of Metallic Single-Wall Carbon Nanotubes with Three Basic Colors; Cyan, Magenta, and Yellow", Applied Physics Express, **1**, 034003, (2008).
3. Fagan, J. A., Huh, J.-Y., Simpson, J. R., Blackburn, J. L., Holt, J. M., Larsen, B. A., and Hight Walker, A. R., "Separation of Empty and Water-Filled Single-Wall Carbon Nanotubes", ACS Nano, **5**, 3943-3953, (2011).
4. Fagan, J. A., Becker, M. L., Chun, J., Nie, P., Bauer, B. J., Simpson, J. R., Hight Walker, A. R. and Hobbie, E. K., "Centrifugal Length Separation of Carbon Nanotubes", Langmuir, **24**, 13880-13889, (2008).

APPENDIX B. ELECTRONIC DURABILITY OF FLEXIBLE TRANSPARENT FILMS FROM SINGLE-WALL CARBON NANOTUBES

Research on the potential applications of single-wall carbon nanotubes (SWCNTs) has grown tremendously over the last two decades. Thin SWCNT films, in particular, show significant promise as transparent conductive coatings[1] with outstanding electronic, mechanical, and optical properties.[2-5] A particularly attractive feature of SWCNT films is that the physical properties can be tuned through the addition or subtraction of a relatively small number of nanotubes. This is because the percolation threshold for a collection of long slender rods scales inversely with aspect ratio,[6] and hence can become exceptionally small for very high-aspect-ratio objects like SWCNTs. The electronic and optical properties of an individual SWCNT are dictated by its band structure,[7] which is in turn determined by the chiral vector (*n*, *m*) that characterizes the symmetry of rolling a 2D graphene sheet into a hollow tube. Unfortunately, as-produced nanotubes tend to contain a broad distribution of lengths, ranging from tens of nanometers up to thousands of micrometers, as well as a broad mixture of the two distinct species of electronic type, typically 1/3 metallic and 2/3 semiconducting.[8] This polydispersity can have a profound influence on the physical properties of thin nanotube films. The critical role of nanotube aspect ratio, for example, in dictating the percolation behavior of thin SWCNT membranes has recently been demonstrated.[6,9,10]

Only very recently have improvements in SWCNT sorting and purification methods[11-15] enabled the production of highly uniform SWCNT ensembles with specific length and/or electronic type distributions. Thin films made from such materials hold tremendous potential for flexible electronics applications, including the replacement of indium tin oxide (ITO) in liquid crystal displays and photovoltaic devices.[16] Metallic SWCNT membranes are among the most

promising candidate materials in this regard, but the mechanical properties of these films are often only qualitatively described as 'flexible', with a relative lack of any quantitative metrics. The wrinkling instability that emerges in compressed thin films on compliant substrates has emerged as a powerful tool for characterizing the mechanical properties of stiff membranes, and a variation on this theme has recently been used to study the bending mechanics[17] of individual nanotubes.[18] We recently used this approach to study the deformation mechanics of films assembled from length purified SWCNTs on soft polydimethylsiloxane (PDMS) substrates.[9,10] By applying an empirical generalization of a continuum mechanical model for thin-film wrinkling[19] to a wide range of compressed nanotube films, changes in membrane elasticity and sheet resistance were linked to strain-induced changes in microstructure and percolation threshold. These data suggest a remarkable degree of strain softening that couples intuitively to the electronic transport properties of the films.[9,10] A number of important issues remain unresolved, however, regarding the microscopic origins of these effects, such as the fundamental roles of van der Waals interactions and electronic type in dictating the mechanical response of the films.

In this contribution, we consider the influence of compressive and cyclic strain on the electronic transport characteristics of type-purified nanotube membranes. Percolated networks of metallic and semiconducting SWCNTs are assembled as thin films on elastic polymer substrates, and the sheet resistance is measured as a function of applied strain through impedance spectroscopy. The topography, microstructure and optical transparency of the membranes are independently characterized using optical microscopy, electron microscopy and optical absorption spectroscopy. We find significant differences in the electronic manifestations of thin-film wrinkling depending on the electronic type of the nanotubes, and we examine the

underlying mechanisms. Our results are relevant to a number of ongoing efforts in transparent conducting films and flexible electronic devices.

B.1. Experimental Methods

B.1.1. Sample Preparation

Polymer substrates of Polydimethylsiloxane (PDMS) were prepared at a 10:1 monomer:crosslinker ratio. The two components were mixed, poured into a mold, and placed in a vacuum oven for 1 h to remove air bubbles. Without breaking vacuum, the mold was then baked at 80 ^{o}C for two hours. Substrates with dimensions 75 mm x 25 mm x 1.5 mm were cut from the mold and cleaned with ethanol. The two ends of a substrate were then clamped in a strain stage and a controlled stretch was applied up to a specific strain. Two SWCNT pieces of approximately 2 mm x 10 mm were cut from the filter paper and placed SWCNT-face down onto the pre-strained substrate, one oriented with the long edge normal to the direction of strain and the other oriented parallel. The sample was then subjected to a gentle acetone wash over the course of an hour to remove the filter paper. This was followed by a 20 min ethanol rinse to remove any residual surfactant, and the test specimen was then placed in a vacuum for several hours to expedite drying. Once dry, the strain on the substrate was carefully released at a controlled and consistent rate, compressing the two films. The sample was then positioned on a mask and placed in a deposition chamber where 10 nm chromium followed by 100 nm gold were sputtered onto the sample without breaking vacuum (Figure B4f). Pieces of the SWCNT films were also deposited in a similar manner on quartz to measure spectra, scattering and thickness.

B.1.2. Characterization

UV-Vis-NIR spectroscopy was performed on a commercial spectrometer and optical transparency analysis was performed on an optical microscope equipped with a spectrometer. Multiple spectra were captured at various locations across the surface of each film. An atomic force microscope (AFM) configured in tapping mode was used to collect several images at various points along the edges of each film, and the thickness was determined by analyzing the quartz-SWCNT step height normal to the edge. Impedance spectroscopy, configured for a 2-probe capacitive frequency (CF) test and calibrated against a 1.01 mF capacitor, was used to measure the complex impedance spectra for each sample. The CF measurement uses a 250 mV amplitude over the frequency interval 1-1000 kHz. A reflection optical microscope was used to collect images of all tested gaps, and these images were used to compute geometrical factors to convert impedance to sheet resistance. A 4-point probe was then used to measure the zero-frequency sheet resistance of each sample, calibrated against an ITO standard. This 4-point measurement was used for the final calibration of each impedance trace from the low frequency plateau in the real part of the response. For cyclic strain experiments, optical measurements of the in-plane geometry as a function of strain were used to compute strain-dependent geometric factors. Measurements of the conductivity of the gold electrodes under cyclic strain showed negligible effects associated with strain-induced changes in electrode structure, contact and topography. Static small-angle light scattering measurements were performed with a 30 mW He-Ne laser directed through unstrained films deposited on thin quartz. The scattered light was imaged on a screen equipped with a beam stop using a thermoelectrically cooled CCD, and measured background scattering from the quartz substrate was subtracted from the total intensity. The signal was then circularly averaged and reduced by the thickness of the film. Increased

scattering in the metallic film (Figure B1d) is a consequence of the shape of the real part of the dielectric response and the near-resonant (M_{11}) laser line.[39] Unless otherwise indicated, error bars are the size of the data markers and represent the maximum instance of two standard deviations in uncertainty.

To image the membranes with transmission electron microscopy (TEM), SWCNT films on quartz or PDMS were first coated with evaporated Pt/C at a shadowing angle of approximately 26 ° (the height of an object is thus half of the length of its shadow). A thin evaporated coating of carbon was then applied at normal incidence. To detach the decorated nanotube membranes from the supporting substrates, a drop of aqueous polyacrylic acid (PAA) solution was placed on the film, allowed to dry overnight at 55 °C, and then removed the following day. Slow removal of the PAA typically resulted in a clean detachment of the membrane from the substrate. The detached sample was then placed PAA side down onto a water bath, dissolving the PAA and floating the SWCNT membrane on the water surface. After gentle washing, the film was retrieved on a copper 600 mesh grid. TEM was performed using a Philips EM400T operated at 120 kV in bright-field mode with an objective aperture to enhance contrast. Images were recorded with a Cantega 2k CCD camera. In this mode, the darkness of a point in the image is correlated to the total mass (integrated thickness) at that location.

B.2. Results and Discussion

Our films are assembled from purified, type-sorted colloidal solutions of laser-ablation and electric arc discharge SWCNTs. The samples contain a broad distribution of lengths, as detailed in the supporting information. The solutions (Figure B1a) are deposited through vacuum filtration onto porous cellulose-ester filter paper supports and then transferred to elastic polymer substrates by back dissolving the filter paper with acetone. The electronic purity of the

membranes is evident in the UV-Vis-NIR absorption spectra of films deposited on quartz (Figure B1b), where the blue and brown-green curves represent metallic and semiconducting SWCNT films, respectively. There is a common graphitic absorption feature near 300 nm corresponding to the plasma frequency of the π electrons. The metallic films show just two optical resonances, the M_{22} just beyond the π-plasmon and the M_{11} near 600-700 nm. In contrast, the semiconducting films show three distinct resonances, S_{11}, S_{22}, and S_{33}. During the vacuum filtration process and subsequent rinsing to remove residual surfactant, individual SWCNTs assemble into bundles of 10-to-10^3 nanotubes (Figure B1c). Small-angle light scattering (SALS) from films deposited on quartz show that the quasi-2D bundle networks both have a mass fractal structure (Figure B1d), with $I(q) \propto q^{-D}$ and a fractal dimension $D \approx 1.7$. The identical value of D suggests that the morphology of the unperturbed networks is independent of electronic type.

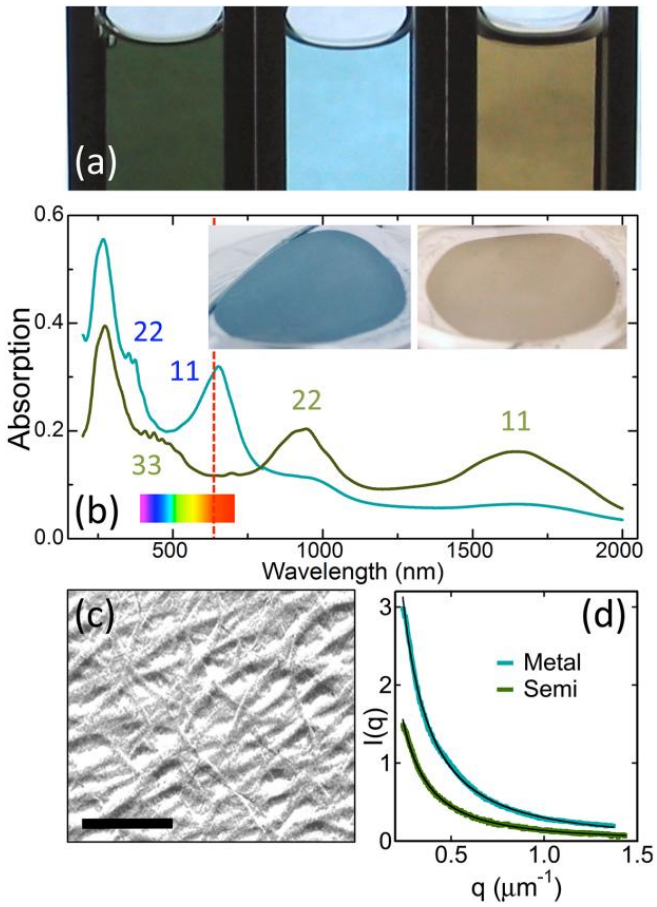

Figure B1: (a) Mixed-type colloidal SWCNT suspension (green) and the subsequent metallic (blue) and semiconducting (brown) fractions. (b) Optical absorption spectra of metallic (blue) and semiconducting (brown) films deposited on quartz with indicated resonant features. The visible spectrum and the laser line used to collect the scattering data in (d) are indicated. The insets show typical type-sorted membranes prepared on filter paper. (c) An unstrained semiconducting SWCNT film imaged with TEM (250 nm scale). (d) Small-angle light scattering profiles of type-sorted films on quartz with power-law fits as described in the text.

The optical and electronic properties of the flexible films are characterized here as a function of film thickness. Three metallic films (h = 20, 28, and 41 nm) and one semiconducting film (h = 35 nm) were created with type-sorted aqueous colloidal solutions of electric arc SWCNTs commercially available from NanoIntegris. The remaining films were assembled from laser ablation SWCNTs type-sorted through an in-house ultracentrifugation procedure as described elsewhere[20] and in the supporting information. Figure B2a shows the transmission

spectra of the metallic films over the wavelength interval 530-730 nm. Laser-ablation SWCNT films (denoted with shades of cyan) exhibit an M_{11} interband feature at approximately 650 nm, while the NanoIntegris films (displayed in blue) show a slight shift in M_{11} to approximately 705 nm due to the slightly larger average diameter of the electric arc nanotubes. Transmission spectra of the semiconducting films are relatively featureless over the relevant wavelength interval. The transmittance in Figure B2a is plotted as a function of film thickness, *h*, and fit to an exponential decay,[21,22]

$$T(h) = e^{-Ah} \tag{4}$$

The extinction coefficients are A = 0.0096 ± 0.001 nm^{-1} for the resonant M_{11} metallic data (Figure B2c) and A = 0.0055 ± 0.0007 nm^{-1} for the semiconducting data (650 nm, Figure B2d).

Gold electrodes were deposited across the surface of each film (Figure B4f) and impedance spectroscopy was used to measure the complex sheet resistance as a function of strain on flexible PDMS substrates. The zero-strain sheet resistance is broken down into real and imaginary parts as a function of frequency for metallic and semiconducting films in Figure B3. The response is typical of percolated conducting networks,[6] with a real part (solid) that is independent of frequency and an imaginary part (dashed) that increases linearly with frequency. The zero-strain sheet conductivity as a function of film thickness is fit to the expression[23]

$$\sigma(h) = \left(\frac{h}{h_c} - 1\right)^{\propto} \tag{5}$$

where σ_0 is the critical amplitude, h_c is the film thickness at the percolation threshold, and α is the critical exponent. The metallic data (Figure B3b) yield σ_0 = 3.3 x10^{-4} □ Ω^{-1} and h_c = 12 ± 2 nm with a critical exponent of 0.92 ± 0.1, while the fit of the semiconducting data (Figure B3e) yields σ_0 = 7.7 x10^{-5} □ Ω^{-1} and h_c = 6 ± 2 nm with a critical exponent of 1.15 ± 0.1. Results from both film types are in agreement with accepted values of the critical exponent ($\alpha \approx 1$) for

percolated 2D conducting networks.[24-28] Film thicknesses range from 9 nm to 72 nm, much less than the wavelength of light, and the transmittance as a function of sheet resistance, R_s, is fit to the expression[21,22]

$$T(R_s) = \left(1 + \frac{1}{2R_s}\sqrt{\frac{\mu_0}{\varepsilon_0}}\frac{\sigma_{op}}{\sigma_{dc}}\right)^{-2} \quad (6)$$

where ε_0 and μ_0 are the permittivity and permeability of free space, respectively, σ_{op} is the optical conductivity, and σ_{dc} is the direct current conductivity. The ratio σ_{op}/σ_{dc} quantifies the combined optical and electronic quality of the films. Our measurements yield a ratio of 1.52 ± 0.3 for metallic films (Figure B3c) and 1.24 ± 0.3 for semiconducting films (Figure B3e). An off-resonant (500 nm) transparency measure for the metallic films gives a slightly better ratio (0.8 ± 0.3). All impedance spectroscopy measurements reported here were performed on compliant PDMS (E = 1.8 MPa and v = 0.48, where E and v are the Young modulus and Poisson ratio, respectively). A 2-fold reduction in sheet conductivity is observed for films deposited on PDMS as opposed to quartz, which we attribute to SWCNT network damage that occurs as a result of the swelling/deswelling processes in the PDMS.[9] When this factor is applied to the data in Figure B3, we find reasonable agreement with comparable measurements reported by Green *et al.*[22] For the relevant range of film thicknesses, reflection optical micrographs on transparent substrates appear pink for the metallic films and green for the semiconducting films due to constructive interference effects (insets, Figure B3b and B3e).

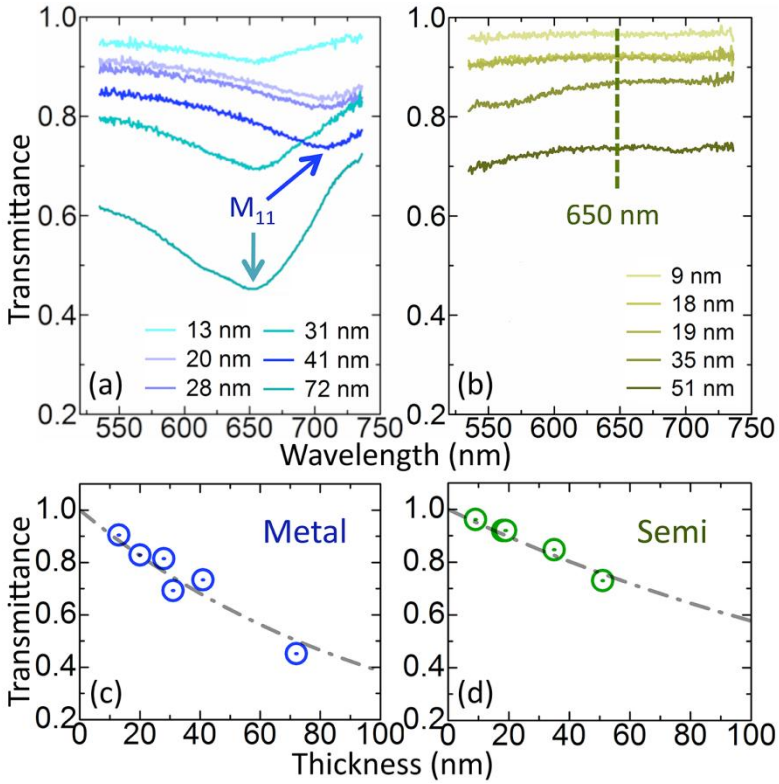

Figure B2: Optical transmittance spectra for (a) the metallic SWCNT films and (b) the semiconducting SWCNT films. (c) Transmittance as a function of film thickness, *h*, for the metallic SWCNTs at the M_{11} resonance and (d) the semiconducting SWCNTs at 650 nm. The curves are fits to an exponential decay.

Our main interest here is the influence of strain on flexible electronic performance, which is uninvestigated for type-purified SWCNT films. Optical reflection micrographs in Figure B4a show an unstrained SWCNT film (left) and the same film under compression (right). Figure B4b shows this same film imaged with transmission electron microscopy, where the dotted line delineates the edge of the membrane. A higher magnification TEM image of the same film is shown in Figure B4c. Variations in local film thickness are correlated with density variations across wrinkled regions of the compressed film. The underlying mechanics of a similar process are described in detail in two earlier contributions.[9,10] Smaller bundles coarsen into larger bundles aligned normal to the direction of the applied strain, which gives the film a surface profile of dark regions surrounded by lighter webs of interconnected bundles. The wrinkling

pattern in Figure B4a closely resembles the behavior we previously observed for length-purified mixed-type films[9,10] and is strikingly similar to the pattern predicted for the elasto-plastic deformation of compressed stiff films on soft substrates.[29]

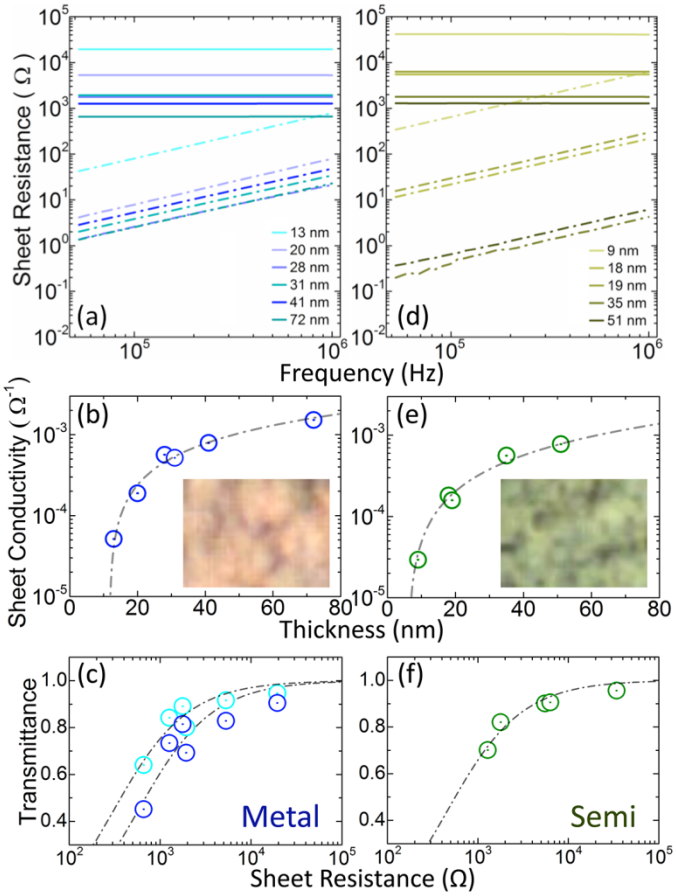

Figure B3: (a) Complex sheet resistance as a function of frequency, (b) sheet conductivity as a function of thickness, and (c) transmittance as a function of sheet resistance for the metallic films. (d)-(f) Analogous plots for the semiconducting films. The real and imaginary parts are shown as solid and dashed curves, respectively, in (a) and (d). Fits to Equation 5 in (b) and (e) are shown as dashed curves. The fits in (c) and (f) are based on the standard model of conducting films described in the text, where cyan markers in (c) represent off-resonant extinction. Reflection optical micrographs of the two film types are shown in (b) and (e).

An interesting question is how these structural changes affect sheet conductivity. To address this, a large number of films were deposited on pre-strained PDMS substrates and subjected to compression through the release of the strain. The density profile of a compressed film measured in TEM (Figure B4b-c) suggests that the SWCNTs align normal to the direction

of pre-strain.[9,10] Two pieces of the same film were thus deposited on each PDMS substrate; one oriented parallel to the compression axis (*x*) and the other oriented perpendicular (*y*). Gold electrodes were then deposited on the surface of the film, as shown in Figure B4f. The anisotropic sheet resistance was measured for films prepared at 0, 2.5, 5, 10, 15 and 20 % compressive strain in the *x*-*y* (solid/dashed) plane for both metallic (Figure B4d) and semiconducting (Figure B4e) films. Statistically, for an ensemble of over 100 SWCNT films prepared on over 50 different PDMS substrates, the conductivity of the metallic films is more robust in response to compression; 12 % of strained metallic films show > 2x anisotropic loss of conductivity, compared with 55 % of strained semiconducting films. Both types show the strongest anisotropy at thicknesses just inside the percolation region, where the networks will be less developed and weaker.

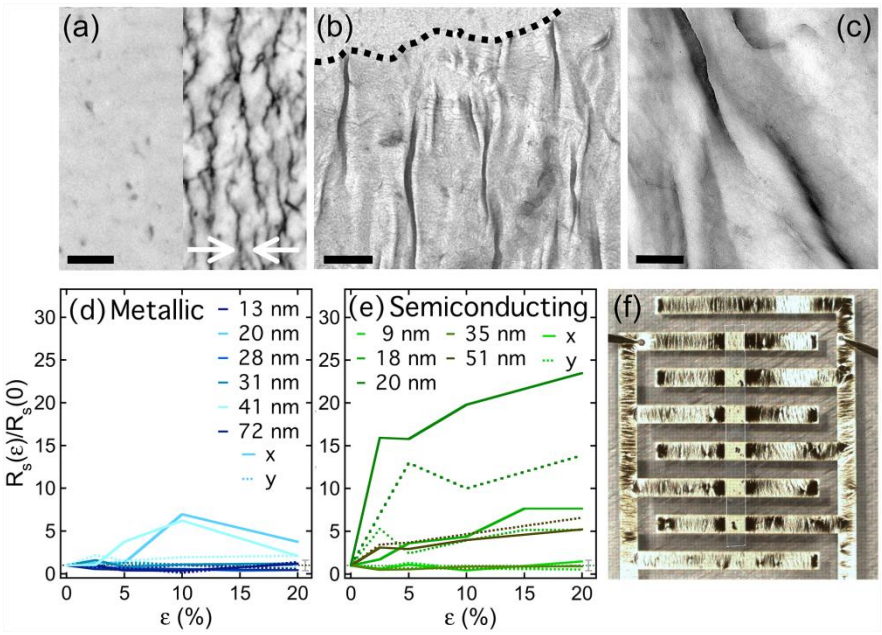

Figure B4: (a) Reflection optical micrograph of an unstrained 35 nm thick semiconducting film on quartz (left) and the same film on PDMS subjected to a 10 % compressive strain (10 μm scale). (b) TEM image of the same film at 10 % strain (2 μm scale). The dotted curve delineates the edge of the film. (c) The same film viewed with TEM at higher magnification (300 nm scale). (d) Strain response of the sheet resistance for metallic films. (e) Strain response of the sheet resistance for semiconducting films. (f) Typical film configuration showing the electrode pattern.

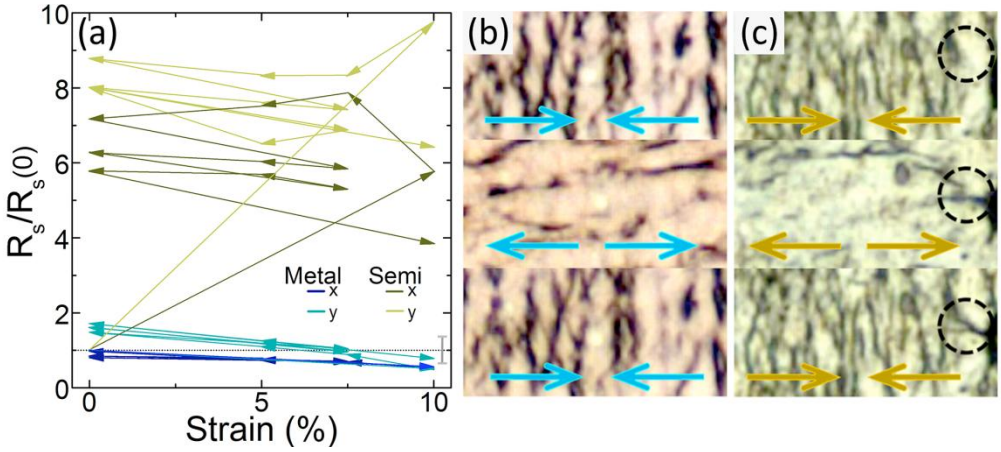

Figure B5: (a) Cyclic strain history of sheet resistance for the metallic and semiconducting films, where the data are normalized by the zero-strain values in Figure B3. (b) Reflection optical micrographs of the wrinkling topography under cyclic strain for a 30 nm thick metallic film, and (c) analogous images for a 50 nm thick semiconducting film. The strain sequence in the images is 10, 0, and 10 %, from top to bottom, where the semiconducting films show topographical change as indicated.

These observations raise the question of durability under cyclic strain, which we investigated for a 30 nm metallic film and a 50 nm semiconducting film (Figure B5). Both samples were prepared at 10 % compressive strain and then subjected to the strain sequence 7.5, 5, 0, 7.5, 5, 0, 7.5, 5, 0, 10 % by repeatedly stretching and relaxing the samples in a strain gauge (the 0 % strain point in Figure B5 corresponds to the independent measurement in Figure B3). The resulting changes in conductivity are illustrated in Figure B5a and support the conclusion that cyclic strain has a larger impact on the semiconducting films. From top to bottom, the optical images in Figure B5 are taken at 10, 0, and 10 % strain, corresponding to cycle points 2, 8, and 12. Comparing the top and bottom image in Figure B5b, the wrinkling pattern is nearly unchanged. The semiconducting film in Figure B5c exhibits a similar "memory", but new topography that emerges later in the cycle suggests continued structural change in the film. Insight into the underlying mechanics follows from a simple scaling analysis. In a linear elastic film, and to some approximation in a yielding SWCNT film, the characteristic wrinkling length scale is[9,10] $\lambda \propto hE_f^{1/3}$, where E_f is the Young modulus of the film. Knowing the thickness ratio,

and computing the average wrinkling length scale from optical micrographs, at 10 % strain the modulus of the semiconducting film is a factor of 0.2 smaller than that of the metallic film, even though the semiconducting film is a factor of 5 deeper into the (unstrained) percolation regime. The loss of conductivity in the semiconducting film (Figure B5a) would thus appear to be accompanied by a significant loss in mechanical rigidity.

B.3. Conclusions

SWCNT-polymer composites are of potential interest for a broad range of emerging applications.[30-33] Through impedance spectroscopy performed on flexible SWCNT membranes deposited on elastic polymer substrates, we have characterized the coupling between mechanical flexibility and electronic performance in thin metallic and semiconducting SWCNT films. Optical transmittance as a function of sheet resistance is consistent with high-quality films, which are well characterized by the concept of percolation in quasi-2D thin fibrous networks. The zero-strain percolation threshold of the semiconducting films is approximately half that of the metallic films, while the semiconducting films are more fragile, suggesting a possible difference in the nature of van der Waals contact forces in the respective networks. Such forces play a critical role in the mechanical response of single-wall carbon nanotube networks.[34-36] Although the length distribution of the semiconducting SWCNTs is slightly broader than that of the metallic SWCNTs (Supporting Information), a broader width would be expected to increase the percolation threshold,[6] and the peak in the length distribution is relatively insensitive to electronic type. The results we present here thus suggest that the metallic films make better flexible transparent conductive coatings; they have higher conductivity/transmission and are more durable.

Both films remember the initial wrinkling configuration in subsequent cycles. Once a compressive strain is applied, and the film responds by folding, the same pattern persists through all future relaxation/compression cycles (Figure B5). In the case of the semiconducting SWCNTs, this pattern becomes augmented by additional topography that is indicative of further plastic change in the films. Since the microstructure of the films is known to evolve as the film deforms,[9,10] the reproducibility of the pattern that emerges in the first strain experiment is a combined consequence of the initial quenched thickness fluctuations in the film and any subsequent strain-induced changes in microstructure. Although there are plastic changes in the metallic films, our data suggest that these occur primarily in the first compression. Additionally, since conductivity in the film only requires intimate electrical contact across the network and not rigidity, physical contact of plastically altered micro-structural regions will be sufficient to maintain electrical percolation, as long as the interfacial conductivity is high. The interfacial conductance of type-specific SWCNT contacts has been measured[37] and metallic-metallic contacts do indeed show better conductivity. Evidence for this can also be seen in Figure B4d, where there is a compressive restoration of the conductivity above 10 % strain for the metallic films. Based on all of these observations, we suggest that metallic SWCNT films are more durable as flexible transparent conductors because (i) the metallic films themselves are more mechanically robust and (ii) the impedance between contacted metallic SWCNT bundles is smaller.

We recently identified the source of this apparent difference in electronic durability as residual surfactant that persists more strongly in the semiconducting films.[39] The surfactant used to process and sort the nanotubes has a stronger attraction to the semiconducting SWCNTs and is thus more difficult to remove. By doubling the duration of the cleaning process, we have been

able to achieve comparable response in terms of sheet resistance and conductivity.^xx This difference stems from a difference in Hamaker constant between the metallic and semiconducting films, which is ultimately what enables their separation. We can see this difference in a detailed study of the mechanical behavior of the films, as detailed in the next section.

B.4. References

1. Blackburn, J. L., Barnes, T. M., Beard, M. C., Kim, Y.-H., Tenent, R. C., McDonald, T. J., Coutts, T. J., and Heben, M. J., "Transparent Conductive Single-Walled Carbon Nanotube Networks with Precisely Tunable Ratios of Semiconducting and Metallic Nanotubes", ACS Nano, ***2***, 1266-1274, (2008).
2. Cao, Q., Rogers and J. A., "Ultrathin Films of Single-Walled Carbon Nanotubes for Electronics and Sensors: A Review of Fundamental and Applied Aspects", Adv. Mater., **21**, 29-53, (2008).
3. Hu, L., Hecht, D. S., and Grüner, G., "Carbon Nanotube Thin Films: Fabrication, Properties, and Applications," Chem. Rev., **110**, 5790-5844, (2010).
4. Kis, A. and Zettl, A., "Nanomechanics of Carbon Nanotubes", Phil. Trans. R. Soc. A, **366**, 1591-1611, (2008).
5. Zhang, D. B. and Dumitrică, T., "Elasticity of Ideal Single-Walled Carbon Nanotubes *via* Symmetry-Adapted Tight-Binding Objective Modeling", Appl. Phys. Lett., **93**, 031919, (2008)
6. Simien, D., Fagan, J. A., Luo, W., Douglas, J. F., Migler, K., and Obrzut, J., "Influence of Nanotube Length on the Optical and Conductivity Properties of Thin Single-Wall carbon Nanotube Networks", ACS Nano, **2**,1879-1884, (2008).

7. Saito, R., Dresselhaus, G., and Dresselhaus, M. S., "Physical Properties of Carbon Nanotubes"; Imperial College Press: London, (1999).

8. Jorio, A. P., Ribeiro, H. B., Fantini, C., Souza, M., Vieira, J. P. M., Furtado, C. A., Jiang, J., Saito, R., Balzano, L., Resasco, D. E., et al., "Quantifying Carbon-Nanotube Species with Resonance Raman Scattering", Phys. Rev. B, ***72,*** 075207, (2008).

9. Harris, J. M., Iyer, G. R. S., Simien, D. O., Fagan, J. A., Huh, J. Y., Chung, J. Y., Hudson, S. D., Obrzut, J., Douglas, J. F., Stafford, C. M., et al., "Structural Stability of Transparent Conducting Films Assembled from Length Purified Single-Wall Carbon Nanotubes", J. Phys. Chem C, **115**, 3973-3981, (2011).

10. Hobbie, E. K., Simien, D. O., Fagan, J. A., Huh, J. Y., Chung, J. Y., Hudson, S. D., Obrzut, J., Douglas, J. F., and Stafford, C. M., "Wrinkling and Strain Softening in Single-Wall Carbon Nanotube Networks," Phys. Rev. Lett., **104**, 125505, (2010).

11. Yanagi, K., Miyata, Y., and Kataura, H., "Optical and Conductive Characteristics of Metallic Single-Wall Carbon Nanotubes with Three Basic Colors; Cyan, Magenta, and Yellow", Appl. Phys. Express, **1**, 034003, (2008).

12. Fagan, J. A., Becker, M. L., Chun, J., and Hobbie, E. K., "Length Fractionation of Carbon Nanotubes Using Centrifugation", Adv. Mater., **20**, 1609-1613, (2008).

13. Arnold, M. S., Suntivich, J., Stupp, S. I., and Hersam, M. C., "Hydrodynamic Characterization of Surfactant Encapsulated Carbon Nanotubes Using an Analytical Ultracentrifuge", ACS Nano, **2**, 2291-2300, (2008).

14. Tu, X., Manohar, S., Jagota, A., and Zheng, M., "DNA Sequence Motifs for Structure-Specific Recognition and Separation of Carbon Nanotubes," Nature, **460**, 250-253, (2009**)**.

15. Fagan, J. A., Becker, M. L., Chun, J., Nie, P., Bauer, B. J., Simpson, J. R., Hight-Walker, A., and Hobbie, E. K., "Centrifugal length separation of carbon nanotubes", Langmuir, **24**, 13880-13889, (2008).

16. Hu, L., Hecht, D. S., and Grüner, G., "Infrared Transparent Carbon Nanotube Thin Films", Appl. Phys. Lett., **94**, 081103, (2009).

17. Nikiforov, I., Zhang, D.-B., James, R. D., and Dumitrică, T., "Wavelike Rippling in Multi-walled Carbon Nanotubes under Pure Bending", Appl. Phys. Lett., **96**, 123107, (2010).

18. Khang, D.Y., Xiao, J., Kocabas, C., MacLaren, S., Banks, T., Jiang, H., Huang, Y. Y., and Rogers, J. A., "Molecular Scale Buckling Mechanics in Individual Aligned Single-Wall Carbon Nanotubes on Elastomeric Substrates", Nano Lett., **8**, 124-130,(2008).

19. Jiang, H. Q., Khang, D., Song, J., Sun, Y., Huang, Y., and Rogers, J. A., "Finite Deformation Mechanics in Buckled Thin Films on Compliant Supports", Proc. Natl. Acad. Sci., **104**,15607-15612, (2007).

20. Hobbie, E. K., Fagan, J. A., Obrzut, J., and Hudson, S. D., "Microscale Polymer-Nanotube Composites", ACS Appl. Mater. Interfaces, **1**, 1561-1566, (2009).

21. Zhou, Y. X., Hu, L. B., and Gruner, G., "A Method of Printing Carbon Nanotube Thin Films", Appl. Phys. Lett., **88**, 123109, (2006).

22. Green, A. A. and Hersam, M. C., "Colored Semitransparent Conductive Coatings Consisting of Monodisperse Metallic Single-Walled Carbon Nanotubes", Nano Letters, **8**, 1417-1422, (2008).

23. Hu, L., Hecht, D. S., and Gruner, G., "Percolation in Transparent and Conducting Carbon Nanotube Networks", Nano Letters, **4**, 2513-2517, (2004).

24. Clerc, J. P., Giraud, G., Laugier, J. M., and Luck, J. M., "The Electrical Conductivity of Binary Disordered Systems, Percolation Clusters, Fractals, and Related Models", Adv. Phys., **39**, 191-309, (1990).

25. Frank, D. J., and Lobb, C. J., "Highly Efficient Algorithm for Percolative Transport Studies in Two Dimensions", Phys. Rev. B, **37**, 302-307, (1988).

26. Laugier, J. M., Clerc, J. P., Giraud, G., and Luck, J. M., "AC Properties of 2D Percolation Networks: A Transfer Matrix Approach", J. Phys. A: Math. Gen., **19**, 3153-3164, (1986).

27. Lajko´, P., and Turban, L., "Percolation and Conduction in Restricted Geometries", J. Phys. A: Math. Gen., **33**, 1683-1692, (2000).

28. Kholodenko, A. L. and Freed, K. F., "Diffusion in Random Media as a Problem of Interacting Bose and Fermi Fields", J. Phys. A: Math. Gen., **17**, L55-L59, (1984).

29. Yin, J., and Chen, X., "Buckling Patterns of Thin Films on Compliant Substrates: the Effect of Plasticity", J. Phys. D: Appl. Phys., **44**, 045401, (2011).

30. Kim, D., Kim, Y., Choi, K., Grunlan, J. C.,and Yu, C., "Improved Thermoelectric Behavior of Nanotube-Filled Polymer Composites with Poly(3,4-ethylenedioxythiophene) Poly(styrenesulfonate)", ACS Nano, **4**, 513-523 (2010).

31. Hermant, M. C., van der Schoot, P., Klumperman, B., and Koning, C. E., "Probing the Cooperative Nature of the Conductive Components in Polystyrene/Poly(3,4 ethylenedioxythiophene): Poly(styrene sulfonate)-Single-Walled Carbon Nanotube Composites", ACS Nano, **4**, 2242-2248, (2010)

32. De, S., Lyons, P. E., Sorrel, S., Doherty, E. M., King, P. J., Blau, W. J., Nirmalraj, P. N., Boland, J. J., Scardaci, V., Joimel, J. et al., "Transparent, Flexible, and Highly Conductive Thin Films Based on Polymer-Nanotube Composites", ACS Nano, **3**, 714-720, (2009).

33. Mauter, M. S., Elimelech, M., and Osuji, C. O., "Nanocomposites of Vertically Aligned Single-Walled Carbon Nanotubes by Magnetic Alignment and Polymerization of a Lyotropic Precursor", ACS Nano, **4**, 6651-6658, (2010).

34. Volkov, A. N. and Zhigilei, L. V., "Structural Stability of Carbon Nanotube Films: The Role of Bending Buckling", ACS Nano, ***4***, 6187-6195, (2010).

35. Hahm, M. G., Wang, H., Jung, H., Hong, S., Lee, S.-G., Kim, S.R., Upmanyu, M., and Jung, Y. J., "Bundling Dynamics Regulates the Active Mechanics and Transport in Carbon Nanotube Networks", Nanoscale, **4**, 3584-3590, (2012).

36. Lipomi, D. J., Vosgueritchian, M., Tee, B. C.K., Hellstrom, S. L., Lee, J. A., Fox, C. H., and Bao, Z., "Skin-Like Pressure and Strain Sensors Based on Transparent Elastic Films of Carbon Nanotubes," Nature Nanotechnology, **6**, 788–792, (2011).

37. Fuhrer, M. S., Nygard, J., Shih, L., Forero, M., Yoon, Y.G., Mazzoni, M. S., Choi, H. J., Ihm, J., Louie, S. G., Zettl, A. et al., "Crossed Nanotube Junctions", Science, **288** 494-497, (2000)

38. Fagan, J. A., Simpson, J. R., Landi, B. J., Richter, L. J., Mandelbaum, I., Bajpai, V., Ho, D. L., Raffaelle, R., Hight Walker, A. R., Bauer, B. J. et al., "Dielectric Response of Aligned Semiconducting Single-Wall Nanotubes", Phys. Rev. Lett., **98**, 147402, (2007).

39. Miller, J. B., Harris, J. M., and Hobbie, E. K., “Purifying Colloidal Nanoparticles through Ultracentrifugation with Implications for Interfaces and Materials” Langmuir, **30**, 7936-7946 (2014).

APPENDIX C. ELASTICITY AND RIGIDITY PERCOLATION IN NANOTUBE FILMS ON POLYMER SUBSTRATES

From the perspective of soft matter, one of the most intriguing applications for purified SWCNTs lies in the realm of flexible electronics,[1] but only a handful of recent studies have focused specifically on the flexural mechanics of pristine nanotube films on compliant polymer substrates.[2-4] These studies suggest that the subtle interplay between nanotube length, electronic type, film elasticity and charge transport can have important implications for the performance and durability of such coatings and the devices that rely on them.[2-4] Flexural studies of length-purified SWCNT films on polydimethylsiloxane (PDMS), for example, suggest a marked strain softening of the nanotube network in response to compressive stress,[2,3] while conductivity studies of type-purified SWCNT films on PDMS suggest that there is a significant coupling between sheet resistance and strain that can depend strongly on electronictype.[4] Despite the potentially important implications, the deformation mechanics of thin flexible sheets of type-purified SWCNTs on polymer supports have never been investigated in detail. In general, the mechanics of wrinkling applied to thin stiff sheets on soft elastic substrates is an active area of soft matter research, with important implications for metrology, self assembly, and polymer science.[5-10] A central element of such work is the observation that a thin film adhered to a much softer substrate will exhibit a harmonic wrinkling instability along the direction of a compressive stress, where the wavelength of the sinusoidal distortion has a simple and utilitarian relationship to the mechanical properties of the film.[5-8] In its simplest form, this instability represents a critical phenomena whereby the film remains flat until a critical strain is exceeded.[6,7] By simply measuring the wavelength of the distortion, a precise knowledge of the thickness of the film and the plane-strain modulus of the substrate gives a direct measure of the plane strain elastic

modulus of the film.[6,7] For films that are disordered or inhomogeneous, recent work demonstrates that the pure harmonic deformation described above gives way to localization or 'folding', with a characteristic spacing of folds that can be twice or even four times the wavelength of harmonic wrinkling.[11] In the case of small-strain plastic or pseudoplastic films, the inability of the sheet to sustain long-range correlations in stress favors wavelength doubling, which has profound implications for the implementation of wrinkling as a metrology for the mechanics of disordered nanotube films.[11] In this contribution, we utilize these recent advances to measure the deformation mechanics of thin films of type purified SWCNTs on PDMS substrates. While the low-strain plateau moduli are consistent with the exceptional (TPa) mechanical properties of the individual nanotubes, the films are remarkably fragile, with yield strains that decrease with increasing thickness. Our data suggest measurable differences in the mechanics of semiconducting vs. metallic nanotube films, and we relate these results to previous measurements of electronic durability and the scale of van der Waals attraction. Finally, a comparison of the percolation metrics obtained here with those obtained from conductivity measurements on identical films suggests a significant distinction between rigidity and connectivity percolation in these systems, and we discuss the implications of this for both rigid-rod networks and flexible nanotube electronics.

The mass per unit area of nanotubes (c) and the mean film thickness (h) are both measured quantities, and by simple geometry, the slope of h *vs.* c should be $(\rho\varphi)^{-1}$, where φ is the effective nanotube volume fraction and ρ is the effective nanotube density (the mass of the graphitic shell divided by the volume of the cylinder). Plots of h *vs.* c show negative curvature, implying that φ increases with thickness. Raman and AFM suggest a mean diameter of 1 nm for the metallic SWCNTs and (0.8 to 0.9) nm for the semiconducting SWCNTs,[12] and we thus take

ρ_m = 1.3 g cm^3 and ρ_s = 1.5 g cm^3 for the two distinct electronic types. This is consistent with plots of *h vs. c*, which have slightly smaller slope for the semiconducting SWCNTs at small *c*. Interpolated volume faction is plotted as a function of thickness in Figure C1a. Throughout the paper, error bars represent two standard deviations in experimental uncertainty and are the size of the data markers unless otherwise indicated. Figure C1b shows a TEM image of the isotropic network structure of an unstrained film, and Figure C1c shows an SEM image of the film edge for a compressed SWCNT coating on PDMS, where the latter is consistent with no delamination of the nanotubes from the substrate. This is also consistent with previous estimates of the depth of attraction (several k_BT) between the same type purified SWCNTs and the PDMS substrates.[12] As described in detail in a previous publication,[4] the sheet resistance of identical SWCNT films deposited on quiescent PDMS was measured by depositing gold/chromium electrodes and using impedance spectroscopy to measure the complex impedance of the films. The real part of the response was then converted to sheet resistance using measured geometrical factors and calibrated against an indium tin oxide (ITO) standard.[4] Conductivity data for each electronic type as a function of film thickness, h, was then fitted to a standard percolation model to extract the conductivity percolation threshold (h_c) and the corresponding critical exponent (β), with h_c = 12 ± 2 nm and β = 0.92 ± 0.1 for the metallic SWCNTs, and h_c = (6 ± 2) nm and β = 1.15 ± 0.1 for the semiconducting SWCNTs.[4]

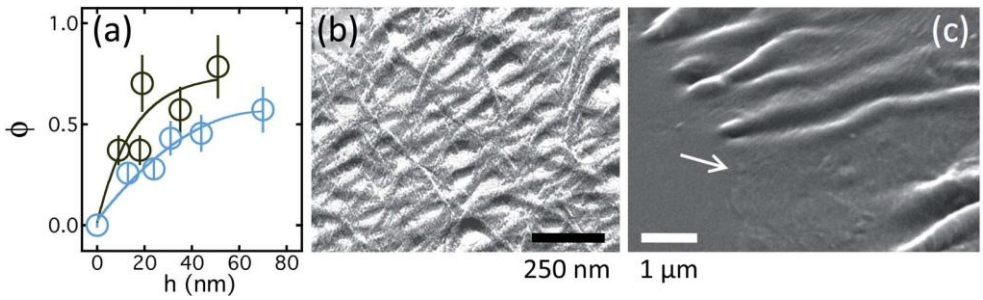

Figure C1: (a) Average volume fraction as a function of mean film thickness for the metallic (blue/light) and semiconducting (brown/dark) films. (b) TEM image of an unstrained 20 nm thick semiconducting film prepared on quartz (250 nm scale) and (c) SEM image of a 40 nm thick semiconducting film on PDMS at 10%strain, where the arrow indicates the film edge (1 µm scale).

C.1. Preparation of Polydimethylsiloxane Substrates

Substrates of PDMS (Dow Corning Sylgard 182) were prepared at a 10:1 by mass monomer : crosslinker ratio. The two components were mixed, transferred to a mold, and put under vacuum for 1 h to remove air bubbles before baking at 80 °C for 2 h. Substrates with dimensions of 75 mm 25 mm 1.5 mm were cut from the mold and cleaned with ethanol. The two ends of a substrate were then clamped in a strain stage and a controlled stretch was applied to a specific prestrain. A 3 mm 3 mm SWCNT piece was cut from filter paper and placed SWCNT-face down on the pre-strained substrate. The sample was then subjected to a gentle acetone wash over the course of an hour to remove the filter paper, followed by a 30 min ethanol rinse to remove any residual surfactant. The test specimen was then placed under vacuum for several hours to expedite drying. Once dry, the strain on the substrate was carefully released at a controlled and consistent rate, compressing the nanotube films and initiating wrinkling. To facilitate small-strain measurements, some of the PDMS substrates were preswollen with acetone prior to depositing the SWCNT films, and the surface topography and shape were then measured as the acetone evaporated. In all cases, the topography was measured with reflection optical microscopy and atomic force microscopy (AFM), and the average spacing of folds and wrinkles for an ensemble of such images was determined by analyzing the images using a numerical

routine written in Python. The modulus of the PDMS substrates, Es = 1.8 MPa, was measured using an Instron 5545 Tensile Tester. For small-strain (3 < 2%) data based on the deswelling of PDMS from acetone, Es was scaled by the volumetric change to account for very slight changes with density.[13]

C.2. Wrinkling, Folding, and Localization

The difference between wrinkling in disordered nanotube films and the usual harmonic wrinkling observed for homogeneous polymer films is immediately evident in optical micrographs of the compressed SWCNT networks.[11] An example of this is shown in Figure C2, which compares the optical reflection profile of two otherwise similar films (h = 30 nm at 5% strain) of different electronic type. Localization is evident as cusp-like folds with a disordered (as opposed to periodic) arrangement. The disordered spacing of folds or ridges is evident in Figure C2c, which shows the computed correlation function $c(x) \propto < u(x)u(0) >$, where *u(x)* is the film deformation from the optical images in Figure C2a. A comparison of the two profiles reveals a measurable difference in the spacing of folds (λ) for the two electronic types, where λ replaces the harmonic wrinkling wavelength[5] λ_0 through

$$\langle\lambda\rangle = 4\pi\langle h\rangle\left(\frac{\bar{E}_f}{3\bar{E}_s}\right)^{1/3} \quad (7)$$

wher $\bar{E}_f = E_f/\left(1-\nu_f{}^2\right)$ and $\bar{E}_s = E_s/(1-\nu_s{}^2)$. E_f is the Young modulus of the film, and ν_f and ν_s are the Poisson ratio of the film and substrate, respectively. Here, we use ν_s = 0.48 for the PDMS and ν_f = 0.33 for the SWCNTs.[2] The differences between equation 7 and the familiar expression[5] for λ_0 appropriate to wrinkling in a homogeneous film are the additional factor of 2 on the RHS and the need to use an average over an ensemble of measurements on identical films.[11]

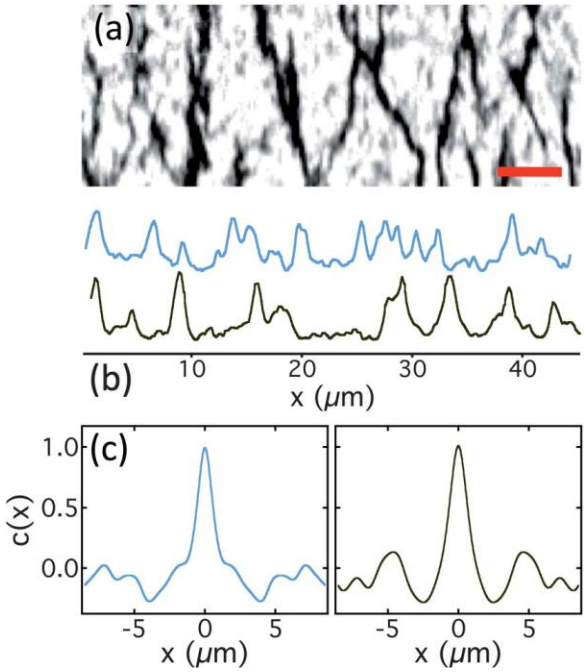

Figure C2: (a) Reflection optical micrograph of a 30 nm thick semiconducting film under 5% compressive strain (scale = 10 mm). (b) Reflection optical contrast profiles of 30 nm thick metallic (top, blue/light) and 30 nm thick semiconducting (bottom, brown/dark) films at 2.5% strain as projected along the strain (x) direction. (c) Correlation function *c(x)* for the profiles shown in (b).

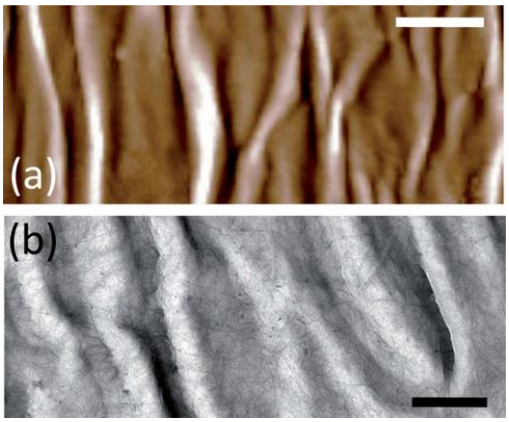

Figure C3: (a) AFM image of a 35 nm semiconducting film at 10% strain (3 mm scale) and (b) a TEM image of the same film (500 nm scale).

The physical origin of folding and bifurcation in disordered SWCNT films is straightforward to understand.[11] Starting conceptually from a homogeneous compressed film under harmonic deformation, the random addition of more than one defect (in the form of a

thickness fluctuation or a quenched variation in modulus) will frustrate the periodicity of the harmonic pattern such that the only option for the film is to localize the deformation around the defects. The leading-order expression for the stress–stress correlation function, in turn, has an overall width of $2\lambda_0$, and the mean spacing of folds is thus $2\lambda_0$ since the folds cannot overlap within the width of their stress correlation.[11] This is the origin of the additional factor of 2 on the RHS of equation 7. These effects are examined in detail in reference 11, which also gives the motivation for equation 7 in the general case of a small-strain plastic film. The structure of folds can be viewed at smaller length scales using AFM and TEM (Figure C3), where it can be seen that the folds often exhibit a crease. Because of the disordered nature of the films, however, it is difficult to deduce a mean length scale from a single high-resolution image. Additionally, the smaller length scale λ_0 always coexists with the larger length scale, although with a much smaller amplitude.[11] Figure C4a and b show the mean spacing of folds, $<\lambda>$, deduced from a large number of optical images as a function of strain for a variety of metallic and semiconducting films. It is important to note that the mean length scales represented in Figure C4 coincide with the mean spacing of the larger-amplitude, fold-like or ridge structures seen at higher magnification with AFM and TEM (Figure C3). However, the need for a large ensemble and the relative ease of optical imaging favor a coarser view that tabulates the spacing of a large number of ridges in a single image.

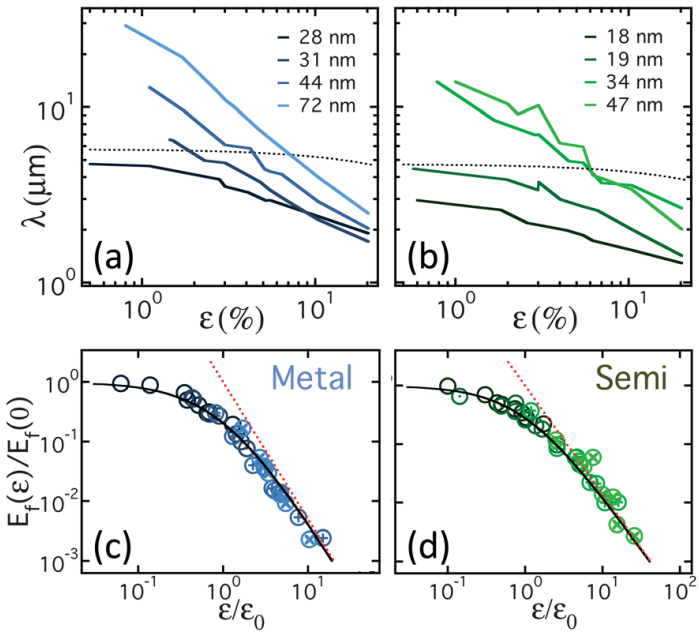

Figure C4: The length scale $<\lambda>$ vs. ε for (a) the metallic and (b) the semiconducting films. The curves denote different h and the dashed curve is the nonlinear response of a homogeneous elastic film.[14] (c) Scaling plot for the metallic films and (d) an analogous plot for the semiconducting films, where the dashed line is the asymptotic power-law. Of the 36 data points for the metals, 3 are excluded from the plot (2 at the highest and 1 at the smallest strain) because they deviate from equation 8 and were not included in the fit. Of the 36 data points for the semis, 2 at the highest strain were excluded for the same reason.

Figure C4a and b also show the theoretically predicted strain-dependence (dashed curve) for a linear elastic film on a nonlinear elastic foundation.[14] For the data presented here, strain softening is evident as a much steeper decrease in $<\lambda>$ with strain than predicted by nonlinear elastic theory. To deduce the zero-strain modulus, $E_f(0)$, and a yield strain, ε_0, $<\lambda>$ was converted to modulus according to equation 7 in a manner that accounts for substrate nonlinearity,[2,14] and the data for each film thickness and electronic type were fit with the phenomenological strain-softening constitutive equation[2,3,11]

$$E_f(\varepsilon) = \frac{E_f(0)}{\left(1+\frac{\varepsilon}{\varepsilon_0}\right)^{\alpha}} \tag{8}$$

with α = 1.85 for the semiconducting SWCNTs and α = 2.3 for the metallic SWCNTs. Figure C4c and d show the collapse of the data when the vertical and horizontal axes of $E_f(\varepsilon)$ vs. ε are scaled by the fitting parameters $E_f(0)$ and ε_0. The modulus and yield strain are shown as a function of film thickness in Figure C5a, and we discuss these results in detail in the following section. It is important to note that our definition of yield strain, which interpolates a low-ε plateau with power-law softening at large ε, is unique, since $E_f(\varepsilon)$ is only strictly equal to $E_f(0)$ for $\varepsilon << \varepsilon_0$.

C.3. Elasticity, Plasticity, and Rigidity Percolation

A physical value for the small-strain modulus of a SWCNT film can be estimated from the theoretical work of Cox on 2D fiber networks in the absence of a matrix, which suggests $Ef(0) \approx E_{tube}\varphi/3$, where f is the effective volume fraction of nanotubes.[15] With $E_{tube} \approx 1.2$ TPa, the range of volume fractions evident in Figure C1 suggests a plateau modulus of 80 to 400 GPa. The data in Figure C5a are in qualitative agreement with this, but a more rigorous analysis requires the concept of percolation. The solid curves in Figure C5a are fits based on the expression

$$E_f(0) \cong E_0\left(\frac{h}{h_c} - 1\right)^{\beta} \qquad (9)$$

where h_c is the percolation threshold.[4] The data suggest $h_c = 27 \pm 4$ nm, $\beta = 1.0 \pm 0.05$ and $E_0 = 350 \pm 30$ GPa for the metallic SWCNTs, and $h_c = 17.5 \pm 4$ nm, $\beta = 1.0 \pm 0.05$ and $E_0 = 500 \pm 30$ GPa for the semiconducting SWCNTs. Equation 8 only strictly applies close to h_c, and the fits thus include a quadratic correction to scaling.[16] Physically, this reflects a saturation of the modulus well inside the percolation regime.[2,3] It is interesting to note that the exponents suggested by these fits are comparable to or slightly larger than those obtained previously for

conductivity measurements on identical films, but the percolation thresholds are 2 to 3 times larger.[4] In general, there is no reason to expect the critical exponents for rigidity and connectivity percolation to be the same, and the data only suggest this when h_c is allowed to vary as a free parameter. Constraining h_c to match previously determined conductivity percolation thresholds,[4] as was done in prior publications focused on length-sorted films of mixed electronic type,[2,3] requires a description of elasticity percolation very similar to that used previously; a large critical exponent (≈ 4 to 7) giving way to a plateau at large thickness.[2,3] When viewed in this manner, the measurements presented here are consistent with results obtained for length monodisperse SWCNTs of mixed electronic type.[2,3]

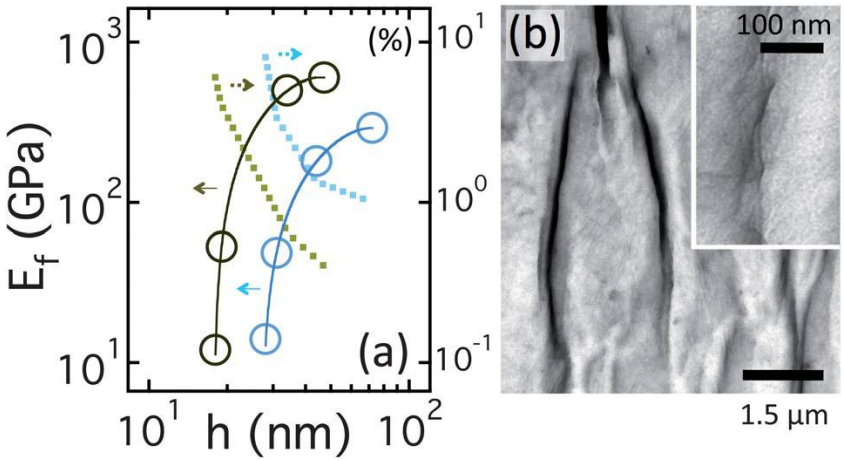

Figure C5: (a) Zero-strain modulus (open) vs. film thickness for each electronic type (blue/light – metallic, brown/dark – semiconducting) with percolation fits (solid curves) as described in the text. The dashed curve is the yield strain (right scale). (b) TEM images of folds, bundles and clusters normal to the direction of applied strain for a 35 nm thick semiconducting film at 10% strain.

Another similarity to length-purified mixed-type SWCNTs is the trend exhibited by the yield strain with increasing thickness.[2,3] For thicker films, ε_0 approaches values of 0.5%, consistent with a physical picture in which compression perturbs the SWCNTs into van der Waals bundles aligned perpendicular to the strain. This is clearly evident in the TEM images shown in Figure C5b, where such bundles appear as dark fold-like structures that contain regions of above

average nanotube density. The small yield strains and the decrease in ε_0 with increasing h can be viewed as a consequence of the magnitude of the SWCNT volume fraction, which is high enough that the unperturbed bundles are already in close proximity, and minimal strain is required to push neighboring bundles into aligned van der Waals minima.

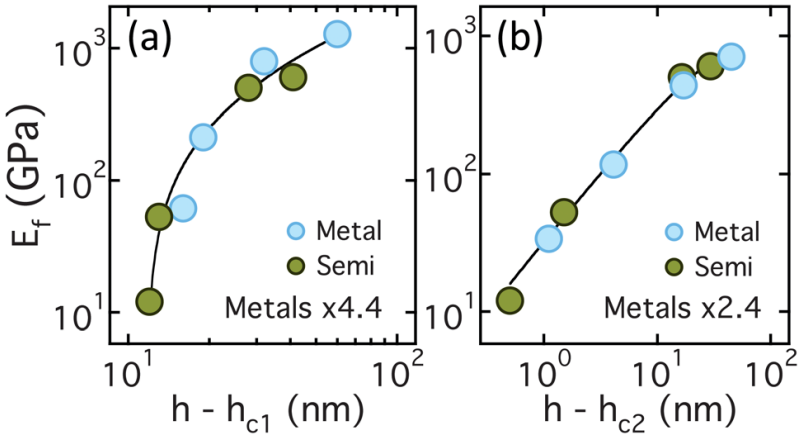

Figure C6: (a) Scaled modulus in terms of the conductivity percolation threshold determined previously,[4] where a factor of 4.4 is required to bring the metallic data up to the semiconducting data. (b) Scaled modulus in terms of the rigidity percolation thresholds used in Figure C5, where a factor of 2.4 is required to bring the metallic data up to the semiconducting data. The vertical label for (b) is the same as (a).

What is unique about the data presented here is the availability of empirical van der Waals (vdW) potentials for the nanotubes in question.[12] Such potentials are based on Lifshitz theory,[17] which converts the imaginary part of the single-tube dielectric response function (measured over a broad spectral range) into the attractive part of an intertube potential, where such attractive forces are a critical component of the full interparticle potential.[18] For the type-purified SWCNTs of interest, the primary Hamaker coefficients are $A_{0S} \approx 195$ zJ for the semi–semi interaction and $A_{0M} \approx 160$ zJ for the metal–metal interaction.[12] These translate into attractive intertube potentials so strong as to render the SWCNTs irreversibly bonded on contact, and the factor of 2 difference in the conductivity percolation threshold can thus be traced to a factor of 2 difference in aspect ratio.[4,11,19,20]

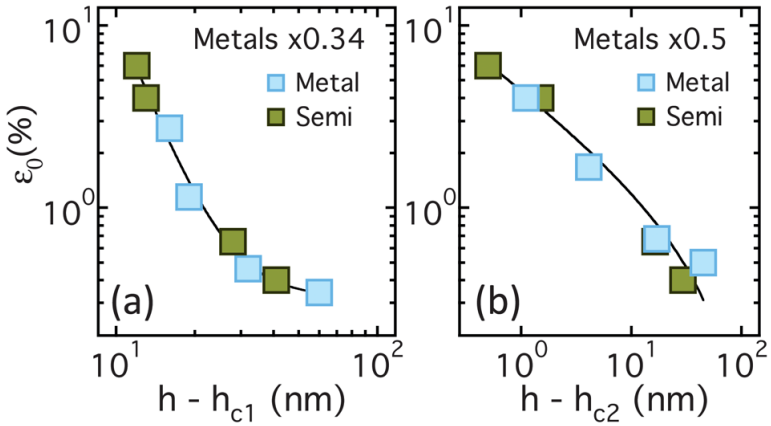

Figure C7: (a) Scaled yield strain in terms of the conductivity percolation threshold determined previously,[4] where a factor of 0.34 is required to bring the metallic data down to the semiconducting data. (b) Scaled yield strain in terms of the rigidity percolation thresholds used in Figure C5, where a factor of 0.5 is required to bring the metallic data down to the semiconducting data. The vertical label for (b) is the same as (a).

Network elasticity in the absence of friction will be dominated by vdW forces, which are parameterized by the contact energy per unit length, *v*, from which we get the energy for perpendicular contact, $w_\perp = 2va$ where a is the nanotube radius. The other relevant quantity is the bending rigidity, κ, and these two quantities define the length $\xi = \sqrt{\kappa/v}$. The Young modulus has units of energy per unit volume;

$$E_0 \cong \frac{v\xi}{\xi^3} \cong \frac{v^2}{\kappa} \tag{10}$$

Defining $v \approx A_0/a$, the ratio of adhesion energy for two perpendicular fibers is $(w_s/w_m) = A_{0s}/A_{0m} \approx 1.25$. With $a_s/\,a_m = 0.85$, we thus obtain

$$\frac{E_{0S}}{E_{0M}} = \left(\frac{a_m A_{0s}}{a_s A_{0m}}\right)^2 \approx 2.2 \tag{11}$$

for the ratio of network moduli. To model the difference in yield strain, we utilize a scaling argument for fractal nanoparticle gels, which models the film as a network of connected clusters. In this view, the yield strain is

$$\varepsilon_0 \propto E_0^{-(1+x)/(d+x)} \tag{12}$$

where $d = 2$ is the spatial dimension and $x \approx 1$ is the bond dimension.[21] This gives

$$\frac{\varepsilon_{0S}}{\varepsilon_{0M}} \approx \left(\frac{E_{0S}}{E_{0M}}\right)^{-2/3} \approx 0.6 \tag{13}$$

These simple scaling arguments can be readily compared with the data shown in Figure C5.

Figure C6a shows scaled modulus data as a function of h - h_{c1}, where h_{c1} is the conductivity percolation threshold determined previously from the sheet resistance.[4] A factor of 4.4 is required to scale the metallic data onto the semiconducting data. Figure C6b shows a similar plot in terms of the rigidity percolation threshold, h_{c2}, determined from the fits in Fig. 6a, where a factor of 2.4 is required to scale the metallic data onto the semiconducting. A similar plot of the yield strain is shown in Figure C7, where the corresponding scale factors are 0.34 and 0.5. Based on the Hamaker constants cited above, the scaling analysis of the previous paragraph suggests that the multiplicative factors required to scale the metallic data onto the semiconducting data should be 2.2 for the modulus (equation 11) and 0.6 for the yield strain (equation 13). The rigidity percolation thresholds determined here thus give scaling factors that are in better agreement with the independently determined Hamaker constants, which supports a clear distinction between rigidity and connectivity percolation for type-purified SWCNT films.

C.4. Conclusions

The difference between rigidity and connectivity percolation has been appreciated forsome time, and this distinction has been the subject of considerable theoretical and computational scrutiny.[22-35] There is compelling evidence that the threshold for rigidity (vector) percolation is indeed higher than that for connectivity (scalar) percolation, although the

difference has been predicted to be rather modest.[36] A recent review of the broader topic of random-fiber network mechanics is given by Picu,[37] who examines this question in detail. The results we offer here suggest that the two thresholds differ by more than a factor of 2, however, at least when film thickness is used as the percolation variable to describe disordered nanotube films. We note that this distinction provides a rather simple explanation for the observation of a regime of non-wrinkling strained films between the connectivity percolation line and the onset of buckling in the state diagram of length-purified mixed-type SWCNTs as measured in the plane of aspect ratio and surface density.[2,3] Further work is needed, however, since the scaling model we offer here is admittedly simplified, and there may be more than one equivalent description of rigidity percolation in these systems. Detailed numerical simulations that specifically target quasi-2D SWCNT networks would be quite valuable in this regard. In a broader view, the changes with electronic type suggested by our data have important practical implications. The observation of stiffer, more fragile films for the semiconducting SWCNTs (Figure C5) is consistent with previous studies of electronic durability in the same films; the distinction between rigidity and conductivity percolation would explain the superior durability of metallic SWCNTs, which have stronger interfacial charge transport.[4] This distinction also offers a way to improve the performance of the semiconducting films, most trivially by taking extra measures to ensure the removal of all residual surfactant, but also through acid doping, which has been shown to markedly improve the charge transport characteristics of SWCNT networks and junctions.[38-40] The loss of rigidity under severe mechanical deformation will not matter for flexible electronics applications if the connectivity of the network remains robust. Doping might also offer an effective way to mitigate other types of more extreme damage, such as that from ion irradiation.[41] Finally, there is clearly an untapped opportunity to further improve our

understanding of these systems through atomistically informed coarse-grained simulations,[42,43] and the insight gained from such models could potentially be applied to other shapes and materials as well.[44] Results obtained from such simulations would likely help clarify the true distinction between rigidity and connectivity percolation in SWCNT films and coatings, as well as offer insight into the nature of plastic deformation and how it might be mitigated.

C.5. References

1. Park, S., Vosguerichian, M. and Bao, Z., "A Review of Fabrication and Applications of Carbon Nanotube Film-Based Flexible Electronics", Nanoscale, **5**, 1727–1752, (2013).
2. Hobbie, E. K., Simien, D. O., Fagan, J. A., Huh, J. Y., Chung, J. Y., Hudson, S. D., Obrzut J., Douglas, J. F. and Stafford, C. M., "Wrinkling and Strain Softening in Single-Wall Carbon Nanotube Membranes" Phys. Rev. Lett., **104**, 125505, (2010).
3. Harris, J. M., Iyer, G. R. S., Simien, D. O., Fagan, J. A., Huh, J. Y., Chung, J. Y., S. D. Hudson, J. Obrzut, J. F., Douglas, C. M. Stafford et al., "Structural Stability of Transparent Conducting Films Assembled from Length Purified Single-Wall Carbon Nanotubes" J. Phys. Chem. C, **115**, 3973–3981, (2011).
4. Harris, J. M., Iyer, G. R. S., Bernhardt, A. K., Huh, J.Y., Hudson, S. D., Fagan, J. A., and Hobbie, E. K., "Electronic Durability of Flexible Transparent Films from Type-Specific Single-Wall Carbon Nanotubes", ACS Nano, **6**, 881–887 (2012).
5. Chung, J. Y., Nolte, A. J., and Stafford, C. M., "Surface Wrinkling: A Versatile Platform for Measuring Thin-Film Properties", Adv. Mater., **23**, 349–368, (2011).
6. Howarter, J. A. and Stafford, C. M., "Instabilities as a Measurement Tool for Soft Materials", Soft Matter, **6**, 5661–5666, (2010).

7. Chena, Y.C. and Crosby, A. J., “Wrinkling of Inhomogeneously Strained Thin Polymer Films”, Soft Matter, **9**, 43–47, (2013).

8. Ramanathan M., Lokitz, B. S., Messman, J. M., Stafford, C. M., and Kilbey, S. M., “Spontaneous Wrinkling in Azlactone-Based Functional Polymer Thin Films in 2D and 3D Geometries for Guided Nanopatterning”, J. Mater. Chem. C, **1**, 2097–2101, (2013).

9. Ohzono, T. and Monobe H., “Microwrinkles: Shape-Tunability and Applications”, Colloid Interface Sci., **368**, 1–8, (2012).

10. Zhao,Y., Loyolo, B. R., and Loh, K. J., “Characterizing the Viscoelastic Properties of Layer-by-Layer Carbon Nanotube–Polyelectrolyte Thin Films”, Smart Mater. Struct., **20**, 075020, (2011).

11. Semler, M. R., Harris, J. M., Croll, A. B. and Hobbie, E. K., “Localization and Length-Scale Doubling in Disordered films on Soft Substrates”, Phys. Rev. E: Stat., Nonlinear, Soft Matter Phys., **88**, 032409, (2013).

12. Hobbie, E. K., Ihle, T., Harris, J. M., and Semler, M. R., "Elasticity and Rigidity Percolation in Flexible Carbon Nanotube Films on PDMS Substrates" Phys. Rev. B: Condens. Matter Mater. Phys., **85**, 245439, (2012).

13. Lee, J. N., Park, C., and Whitesides, G. M., “Solvent Compatibility of Poly (dimethylsiloxane)-Based Microfluidic Devices” Anal. Chem., **75**, 6544–6554, (2003).

14. Sun, J.Y., Xia, S., Moon, M.Y., Oh, K. H., and Kim, K.S., “Folding wrinkles of a Thin Stiff Layer on a Soft Substrate” , Proc. R. Soc. London, Ser. A, **468**, 932–940, (2012).

15. Cox, H. L., “The Elasticity and Strength of Paper and Other Fibrous Materials” Br. J. Appl. Phys., **3**, 72–79, (1952).

16. The full expression is $E_f(0) = E_0(h/h_c - 1)^{\beta} + E_2(h/h_c - 1)^2$ with E_0 = 350 ± 50 GPa and E_2 = -100 ± 30 GPa for the metals, and E_0 = 750 ± 50 GPa and E_2 = -250 ± 30 GPa for the semiconducting SWCNTS. The second term phenomenologically accounts for the saturation of $E_f(0)$ well inside the percolation regime.

17. Rajter, R. F., French, R. H., Ching, W. Y., Podgornikde, R. and Parsegian, V. A., "Chirality-Dependent Properties of Carbon Nanotubes: Electronic Structure, Optical Dispersion Properties, Hamaker Coefficients and van der Waals–London Dispersion Interactions", RSC Adv., **3**, 823–842, (2013).

18. Wu, L., Gao, B., Tian, Y., Munoz-Carpena R., and Ziegler, K. J., "DLVO Interactions of Carbon Nanotubes with Isotropic Planar Surfaces", Langmuir, **29**, 3976–3988, (2013).

19. Kyrylyuk A. V. and van der Schoot, P., "Continuum Percolation of Carbon Nanotubes in Polymeric and Colloidal Media", Proc. Natl. Acad. Sci. U. S. A., **105**, 8221–8226., (2008).

20. Otten, R. H. J. and van der Schoot, P., "Connectivity Percolation of Polydisperse Anisotropic Nanofillers", J. Chem. Phys., **134**, 094902, (2011).

21. Shih, W.H., Shih, W. Y., Kim, S. I., Liu, J. and Aksay, I. A., "Scaling Behavior of The Elastic Properties of Colloidal Gels", Phys. Rev. A: At., Mol., Opt. Phys., **42**, 4772–4780, (1990).

22. Feng, S. and Sen, P., "Percolation on Elastic Networks: New Exponent and Threshold", Phys. Rev. Lett., **52**, 216–220, (1984).

23. Day, A. R., Tremblay, R. R., and Tremblay, A.M. S., "Rigid backbone: A New Geometry for Percolation", Phys. Rev. Lett., **56**, 2501–2504, (1986).

24. Roux, S. and Hanson, A., “Transfer-Matrix Study of the Elastic Properties of Central-Force Percolation”, Europhys. Lett., **6**, 301–305, (1988).

25. Hansen, A. and Roux S., “Universality Class of Central-Force Percolation” Phys. Rev. B: Condens. Matter Mater. Phys., **40**, 749–752, (1989).

26. Arbabi, S. and Sahimi M., “Mechanics of Disordered Solids. I. Percolation on Elastic Networks with Central Forces”, Phys. Rev. B: Condens. Matter Mater. Phys., **47**, 695–702, (1993).

27. Obukhlov S. P., “First Order Rigidity Transition in Random Rod Networks”, Phys. Rev. Lett., **74**, 4472–4475, (1995).

28. Jacobs, D. J. and Thorpe, M. F., “Generic Rigidity Percolation: The Pebble Game”, Phys. Rev. Lett., **75**, 4051–4054, (1995).

29. Moukarzel, C. and Duxbury, P. M., “Stressed Backbone and Elasticity of Random Central-Force Systems”, Phys. Rev. Lett., **75**, 4055–4058, (1995).

30. Jacobs, D. J. and Thorpe, M. F., “Generic Rigidity Percolation in Two Dimensions” Phys. Rev. E: Stat., Nonlinear, Soft Matter Phys., **53**, 3682–3693, (1996).

31. Moukarzel, C., Duxbury, P. M., and Leath, P. L., “Infinite-Cluster Geometry in Central-Force Networks”, Phys. Rev. Lett., **78**, 1480–1483, (1997).

32. Moukarzel, C., Duxbury, P. M., and Leath, P. L., “First-order Rigidity on Cayley Trees”, Phys. Rev. E: Stat., Nonlinear, Soft Matter Phys., **55**, 5800–5811, (1997).

33. Duxbury, P. M., Jacobs, D. J., Thorpe, M. F., and Moukarzel, C., “Floppy Modes and the Free Energy: Rigidity and Connectivity Percolation on Bethe Lattices”, Phys. Rev. E: Stat. Phys., Plasmas, Fluids, Relat. Interdiscip.Top., **59**, 2084–2092, (1999).

34. Latva-Kokko, M., Makinen, J., and Timonen, J., "Rigidity Transition in Two-Dimensional Random Fiber Networks" Phys. Rev. E: Stat., Nonlinear, Soft Matter Phys., **63**, 046113, (2001).

35. Moukarzel, C. and Duxbury, P. M., "Rigidity Transition in Two-Dimensional Random Fiber Networks", Phys. Rev. E: Stat. Phys., Plasmas, Fluids, Relat. Interdiscip. Top., **59**, 2614– 2622, (1999).

36. Latva-Kokko, M. and Timonen, J., "Rigidity of Random Networks of Stiff Fibers in the Low-Density Limit", Phys. Rev. E: Stat., Nonlinear, Soft Matter Phys., **64**, 066117, (2001).

37. Picu, R. C., "Mechanics of Random Fiber Networks—a Review", Soft Matter, **7**, 6768–6785, (2011).

38. Mirri, F., Ma, A. W. K., Hsu, T. T., Behabtu, N., Eichmann, S. L., Young, C. C., Tsentalovich, D. E., and Pasquali, M., "High-Performance Carbon Nanotube Transparent Conductive Films by Scalable Dip Coating", ACS Nano, **6**, 9737–9744, (2012).

39. Ma, A. W. K., Nam, J., Behabtu, N., Mirri, F., Young, C. C., Dan, B., Tsentalovich, D., Majumder, M., Song, L., Cohen, Y. et al., "Scalable Formation of Carbon Nanotube Films Containing Highly Aligned Whiskerlike Crystallites", Ind. Eng. Chem. Res., **52**, 8705–8713, (2013).

40. Znidarsic, A., Kaskela, A., Laiho, P., Gaberscek M., Ohno, Y., Nasibulin, A. G., Kauppinen, E., and Hassanien, A., "Spatially Resolved Transport Properties of Pristine and Doped Single-Walled Carbon Nanotube Networks" J. Phys. Chem. C, **117**, 13324–13330, (2013).

41. Rossi, J. E., Cress, C. D., Helenic, A. R., Schauerman, C. M., DiLeo, R. A., Cox, N. D., Messenger, S. R., Weaver, B. D., Hubbard, S. M., and Landi, B., "Ion Irradiation of Electronic-Type-Separated Single Wall Carbon Nanotubes: A Model for Radiation Effects in Nanostructured Carbon", J. Appl. Phys., **112**, 034314, (2012).

42. Hahm, M. G., Wang, H. L., Jung, H. Y., Hong, S., Lee, S. G., Kim, S. R., Upmanyu M. and Jung, Y. J., "Bundling Dynamics Regulates the Active Mechanics and Transport in Carbon Nanotube Networks and Their Nanocomposites", Nanoscale, **4**, 3584–3590, (2012).

43. Ostanin I., Ballarini, R., Potyondy, D., and Dumitricˇa, T., "A Distinct Element Method for Large Scale Simulations of Carbon Nanotube Assemblies", J. Mech. Phys. Solids, **61**, 762–782, (2013).

44. Pichard, H., Duclos, A., Groby, J. P., Tournat, V. and Gusev, V. E., "Two-Dimensional Discrete Granular Phononic Crystal for Shear Wave Control", Phys. Rev. B: Condens. Matter Mater. Phys., **86**, 134307, (2012).

APPENDIX D. IMPACT OF NANOTUBE DEPOSITION ON NANOTUBE-SILICON HETEROJUNCTION SOLAR CELL PERFORMANCE

A variety of techniques to help adhere the SWCNT film to the Si surface exist in the literature. The most common of these is to float a SWCNT film on the surface of water.[1,2] Strong hydrophobicity in the SWCNT film will pull it tight across the water's surface. A pre-patterned wafer is then used to scoop the film from the water. The SWCNTs come into contact with the Si surface as the water evaporates from the system, forming the heterojunction. Some groups claim that following this process with an ethanol rinse helps adhesion;[3] while others advise compression and thermal annealing..[4,5]

Several devices with identical 50 nm electronically-mixed SWCNT films were subjected to the various deposition techniques. A control-device implemented the ethanol process described in chapter 3; while another used the standard water collection technique. A set of devices with both deposition techniques were then compressed with Teflon and thermally annealed (100 °C, 60 min) in a vacuum oven. A final set of devices were created using Si substrates treated with HF immediately before and after SWCNT deposition. Table 1 lists the photovoltaic performance of these devices. Their IV profiles are shown in Figure D1.

Table D2: Photovoltaic performance across deposition processes.

	Ethanol(eth)	**H2O**	**annealed Teflon(eth)**	**annealed Teflon(H2O)**	**HF(eth)**	**HF(H2O)**
Voc (V)	0.5879	0.5829	0.3299	0.3093	0.5693	0.5655
Jsc (mA/cm2)	29.034	30.186	27.701	26.21	24.968	24.831
Fill Factor (%)	62.99	58.11	42.46	61.39	69.36	69.82
Pmax (mW)	1.121	1.066	0.3985	0.5247	0.904	0.8736
Efficiency (%)	10.75	10.22	3.88	4.98	9.86	9.81
Rshunt est (Ω)	589	173	731	1700	785	524

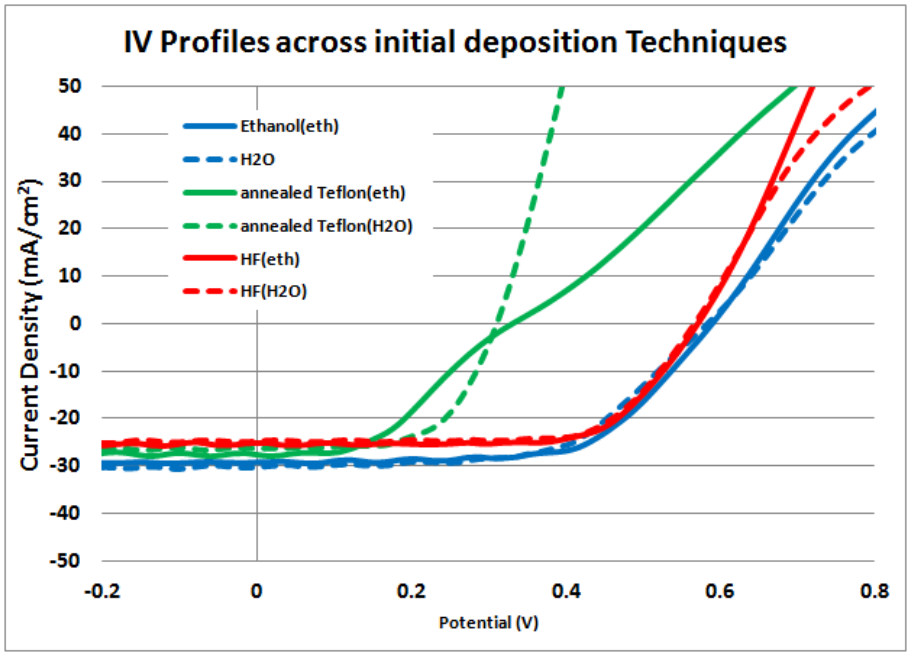

Figure D1: IV profiles under light exposure for a set of 6 NSH solar cells demonstrates the dependence of device performance on the initial SWCNT deposition technique.

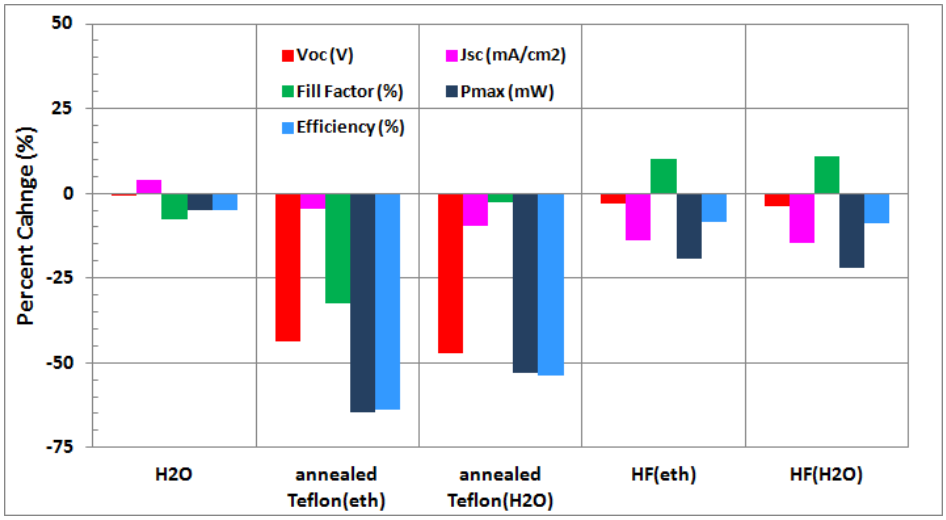

Figure D2: The percent-change in key photovoltaic variables with respect to the standard ethanol deposition process described in Chapter 3 of the text.

These tests indicate that ethanol-based deposition techniques provide the greatest benefit to device performance, while annealed Teflon-compressing appears to be detrimental to device performance on all measures within the sample set considere. Cleaning the Si substrate with HF

prior to deposition appears to have the greatest effect on SWCNT-Si connectivity as seen through improved fill factor, however all other variables remain hindered rather than improved by the additional HF cleaning step. The percent-change in key photovoltaic variables are shown in Figure D2. We find that the liquid-mediated ethanol deposition process not only results in the best performing devices, it does so in a way that is faster, cleaner, and more accurate than the other methods tested.

D.1. References

1. Jung, Y., Li, X., Rajan, N.K., Taylor, A.D. and Reed, M.A., "Record High Efficiency Single-Walled Carbon Nanotube/Silicon P-N Junction Solar Cells", Nano Lett., (2013), 95-99, (2013).
2. Li, X., Jung, Y., Sakimoto, K., Goh, T.H., Reed, M.A. and Taylor, A.D., "Improved Efficiency of Smooth and Aligned Single Walled Carbon Nanotube/Silicon Hybrid Solar Cells", Energy Environ. Sci., **6**, 879-887, (2013).
3. Li, Z., Kunets, V.P., Saini, V., Xu, Y., Dervishi, E., Salamo, G.J., Biris, A.R. and Biris, A.S., "Light-Harvesting Using High Density p-Type Single Wall Carbon Nanotube/n-Type Silicon Heterojunctions", ACS Nano, **3**, 1407-1414, (2009).
4. Tune, D.D., Flavel, B.S., Krupke, R. and Shapter, J. G., "Carbon Nanotube-Silicon Solar Cells", Adv. Energy Mater., **2**, 1043-1045, (2012).
5. Tune, D. D., Blanch, A. J., Krupke, R., Flavel, B. S., and Shapter J. G., "Nanotube Film Metallicity and its Effect on the Performance of Carbon Nanotube-Silicon Solar Cells. Phys. Status Solidi A, **211**, 1479-1487, (2014)

APPENDIX E. IMPACT OF NANOTUBE SHEET RESISTANCE ON - SILICON HETEROJUNCTION SOLAR CELL PERFORMANCE

The voltage at maximum power, V_m, is related to the photo (source) current, I_S, and the dark (saturation) current, I_0, by[1]

$$\left(1+\frac{V_m}{V_T}\right)\exp\left(\frac{V_m}{V_T}\right)=1+\frac{I_S}{I_0} \tag{14}$$

where $V_T = k_B T/q$ is the thermal voltage. The junction dark current is

$$I_0 = AJ_0 \propto \exp\left(-\frac{\Phi}{k_B T}\right), \tag{15}$$

where Φ is the barrier height. The photo-conversion efficiency (PCE) is

$$\eta = \frac{V_m J_0 (V_m/V_T)\exp(V_m/V_T)}{P_{in}} \tag{16}$$

where P_{in} = 100 mW/cm^2 for AM1.5 illumination.[1] When the ratio V_m/V_T is of order 10 to 20, an approximate solution to equation 14 is

$$V_m/V_T \propto \ln\left(\frac{I_S}{I_0}\right). \tag{17}$$

Similarly, another reasonable approximation is

$$\left(\frac{V_m}{V_T}\right)\exp\left(\frac{V_m}{V_T}\right)\approx 1+\frac{I_S}{I_0}, \tag{18}$$

which when combined with equation 17 yields

$$\eta \propto V_T(J_0+J_S)\ln\left(\frac{J_S}{J_0}\right)\approx V_T J_S \ln\left(\frac{J_S}{J_0}\right). \tag{19}$$

The influence of a parasitic series resistance (primarily the SWCNT sheet resistance) reduces the power as $P' \approx (VI)_m - {I_m}^2 R_s \approx P_m(1 - I_s R_s/V_m)$, from which we get

$$\eta \propto J_S \ln\left(\frac{J_S}{J_0}\right)\left(1-\frac{J_S A R_S}{V_T \ln(J_S / J_0)}\right). \quad (20)$$

Because the photocurrent is proportional to the transmission, $T(\lambda)$, of the SWCNT film,[1-3] the PCE coarsely scales as $\eta \propto T(\lambda)[1-\alpha T(\lambda)R_S+...]$ or $\eta R_S \propto x(1-\alpha x+...)$ with $x = T(\lambda)R_S$. This is the fit of the efficiency in Figure 24c of the text.

E.1. References

1. Li, S. S. ,"Semiconductor Physical Electronics", Springer, New York, (2006).
2. Simeonov, S.S., Kafedjiiska, E. I., Guerassimov, A. L., "Quantum Efficiency of the Photocurrent in Schottky Barrier Structures.", Solar Cells, ***20***, 99-118, (1987).
3. Sze, S. M., "Physics of Semiconductor Devices", Wiley, New York, (1969).

APPENDIX F. JUNCTION COMPOSITION VIA X-RAY PHOTOELECTRON SPECTROSCOPY

Focusing on the nature of the heterojunctions, X-Ray photoelectron speectroscopy measurements were performed on a Thermo Scientific K-Alpha, which scans a range of binding energies and converts counts per energy interval into material composition. Data were processed to identify elemental carbon, chlorine, chromium, gold, silicon and oxygen. After each scan, the sample collection point was subjected to an argon etch to cut further into the device. These scans were used to construct a depth-profile for an NSH solar cell. (Figure F1)

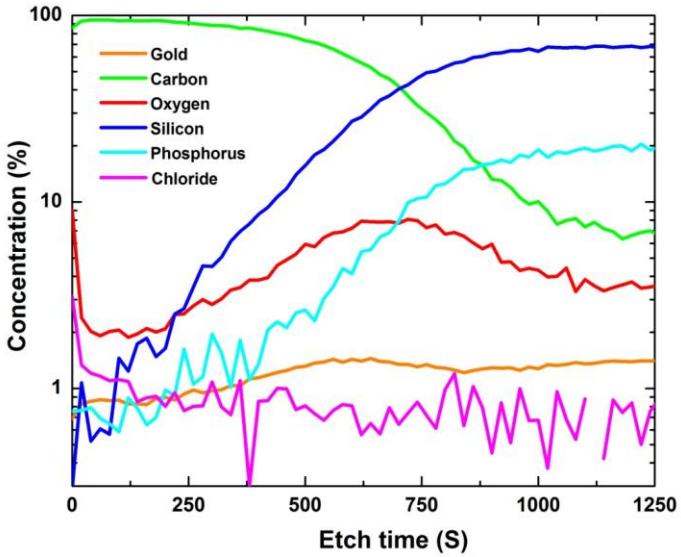

Figure F1: The elemental composition at the surface of an NSH solar cell where etch time is directly related to surface-depth via Argon-etch.

An etch time of 0 seconds corresponds to the initial surface scan of the device, indicating peaks of chloride, oxygen, and carbon, which is indicative of residual $SOCL_2$ dopant on the surface of the SWCNT layer. As the Argon-etch approaches the Si surface at approximately 700 seconds, another oxygen peak is observed which corresponds to a native oxide layer at the junction interface, accompanied by a noticeable increase in silicon and phosphorus (Si n-dopant).

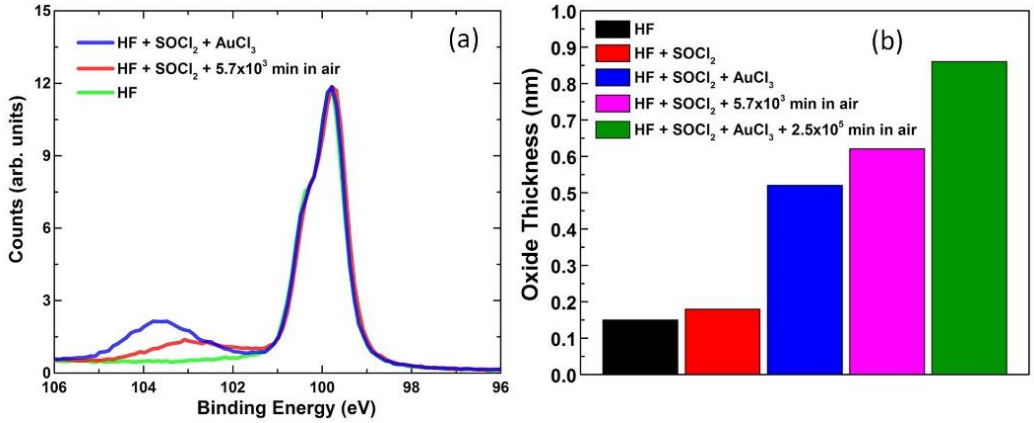

Figure F2: (a) XPS spectra showing the evolution of the silicon oxide peak. (b) Oxide layer thickness deduced from XPS under different processing conditions.

Oxide thickness at the interface plays an important role for the charge separation mechanisms within the device, where the absence of an oxide layer points to PN junctions and oxide layers on the orders of several nanometers give rise to a metal-insulator-semiconductor (MIS) architecture. A detailed examination of silicon binding energies shows 3 peaks in the energy range of 95 -105 eV. (Figure F2a) where the intensity ratio between the SiO_2 peak at 104 eV and elemental Si at 100 eV can be used to determine the thickness of the oxide layer at the junction interface. Figure F2b shows the effective oxide thickness at the interface as a result of the various chemical processes needed to create high efficiency NSH solar cells.